Imaging physical phenomena with local probes: From electrons to photons

Dawn A. Bonnell

Nano/Bio Interface Center and Department of Materials Science and Engineering, The University of Pennsylvania, Philadelphia, Pennsylvania 19104, USA

D. N. Basov

Department of Physics, The University of California at San Diego, La Jolla, California 92093, USA

Matthias Bode

Experimental Physics University of Wuerzburg, Wuerzburg, Germany

Ulrike Diebold

Institute of Applied Physics, Vienna University of Technology, Vienna, Austria

Sergei V. Kalinin

Center for Nanophase Materials Sciences, Oak Ridge National Laboratory, Oak Ridge, Tennessee 37831, USA

Vidya Madhavan

Department of Physics, Boston College, Chestnut Hill, Massachusetts 02467, USA

Lukas Novotny

The Institute of Optics, The University of Rochester, Rochester, New York 14627, USA

Miquel Salmeron

Materials Sciences Division, Lawrence Berkeley National Laboratory, Berkeley, California 94720, USA

Udo D. Schwarz

Mechanical Engineering and Materials Science, Yale University, New Haven, Connecticut 06520, USA

Paul S. Weiss

California NanoSystems Institute and Department of Chemistry and Biochemistry and Department of Materials Science and Engineering, University of California, Los Angeles, Los Angeles, California 90095, USA

(published 26 September 2012)

The invention of scanning tunneling and atomic force probes revolutionized our understanding of surfaces by providing real-space information about the geometric and electronic structure of surfaces at atomic spatial resolution. However, the junction of a nanometer-sized probe tip and a surface contains much more information than is intrinsic to conventional tunneling and atomic force measurements. This review summarizes recent advances that push the limits of the probing function at nanometer-scale spatial resolution in the context of important scientific problems. Issues such as molecular interface contact, superconductivity, electron spin, plasmon field focusing, surface diffusion, bond vibration, and phase transformations are highlighted as examples in which local probes elucidate complex function. The major classes of local probes are considered, including those of electromagnetic properties, electron correlations, surface structure and chemistry, optical interactions, and electromechanical coupling.

DOI: 10.1103/RevModPhys.84.1343 PACS numbers: 07.79.Fc, 68.35.B−, 68.37.Ps, 07.79.Lh

CONTENTS

I. INTRODUCTION

The quest toward understanding the behavior of condensed matter has relied on measuring structure, bonding, and properties at increasingly local levels. The invention of scanning tunneling microscopy (STM) by Binnig and Rohrer (1982) revolutionized our understanding of surfaces by providing real-space information about the geometric and electronic structure of surfaces at atomic spatial resolution. It has been over 25 years since the invention of STM and atomic force microscopy (AFM) during which these techniques have been employed to advance our understanding of physics and chemistry at surfaces and interfaces. The impact of these techniques inspired efforts to extend the strategy of local probes to electrical, optical, magnetic, dielectric, and chemical phenomena at ultrahigh spatial resolution. Understanding complex phenomena at the nanometer scale not only advances frontiers of fundamental physics and chemistry, but is a prerequisite to next-generation applications in electronics, sensing, catalysis, energy harvesting, and more. Recent advances are demonstrating unprecedented and unexpected new capabilities in probes of complex phenomena. Here we review the current status and the next frontiers of scanning local probes.

A "phase" space of physical phenomena in terms of structure, properties, and time (= 1/frequency) illustrates how new probes can advance our understanding of physical processes; see Fig. 1. Structure is usually considered in terms of length scales from millimeters to atomic dimensions, shown along the *y* axis. The time scales of physical processes span femtoseconds to hours (terahertz to 0.001 Hz), shown along the *x* axis. The vertical axis represents properties and/or function, encompassing a wide range of phenomena with many levels of complexity. Most characterization techniques are optimized on the length scale–property (function) plane or the time scale–property plane. For example, classical optical microscopy covers spatial scales from millimeters to microns, but is limited to structural characterization and time regimes of milliseconds or longer. In contrast, optical spectroscopies routinely access dynamic processes in the femtosecond time regime, but do not achieve spatial resolution. Early scanning probes expanded beyond some of these constraints but operate predominantly in the length scale–function plane of Fig. 1. In the simplest limit, measuring current at a tip-surface junction probes scalar properties such

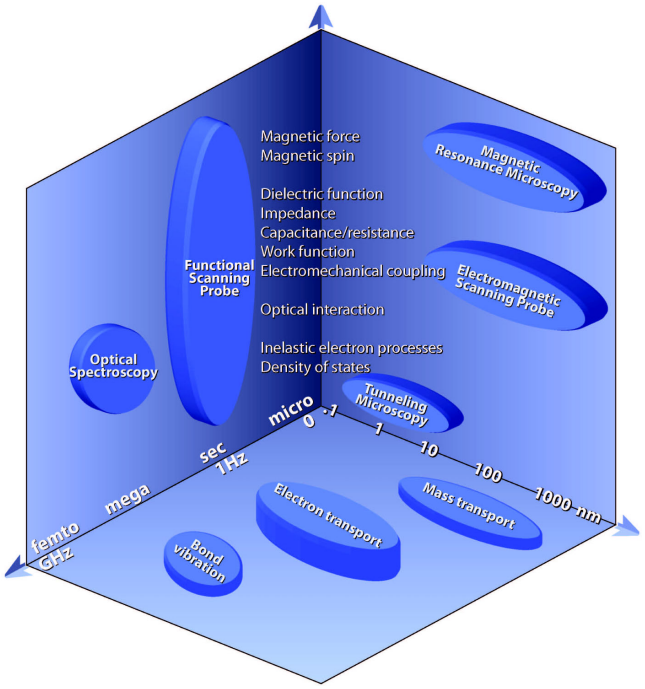

FIG. 1 (color online). A schematic representation of the capabilities of various probes in terms of length scales, time scales, and complexity of the property and response functions.

as conductance, or in the case of tunneling, single-valued density of states. Adding voltage variation enables access to electronic structure, which is a consequence of the details of atomic bonding. This can be viewed as extending into the frequency space. An example of probing increased complexity is found in the combination of optical interactions in the near field of a probe tip, with time accessed via multiple harmonics. Here the real and imaginary contributions to a dielectric function can be probed by extending from the length scale–property plane up the vertical axis and into the time regime. The advances reviewed here examine the structure–property, structure–time, and property–time regimes in this space (see Fig. 1). The field of the new scanning probes strives to quantify aspects of all three axes, moving into three dimensions in this space, and is making remarkable progress.

By way of introduction, the underlying premise in scanning probe microscopy is that a small, sharp probe tip is brought close to a surface and the interactions between the two contain information about the surface. In the simplest case of STM, the tip is a metal wire and the surface is conducting such that an electrical circuit enables a tunneling current between them to be detected, as illustrated in Fig. 2(a). Another class of scanning probes, AFM, involves attaching the tip to a cantilever such that the mechanical properties of the cantilever can be used to detect the tip-surface interaction (see Fig. 2(b)) (Binnig, Quate, and Gerber, 1986). Figure 2(c) conceptualizes a tip-surface junction. In all cases, the tip-surface interaction function is inherently complex, containing simultaneous contributions from electrostatic, magnetic, mechanical, and atomic bonding forces, which operate over a range of tip-surface separations. Consequently, the tip-surface junction can be a rich source of information on complex properties. The challenge is to extract properties and complex property functions from this milieu of information.

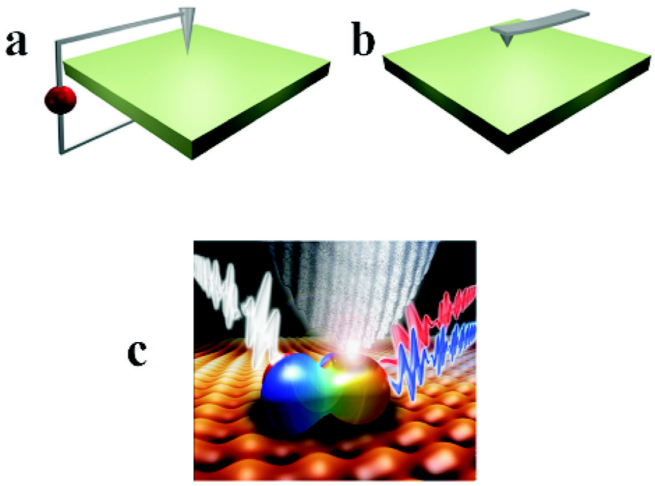

FIG. 2 (color online). General principles of (a) scanning tunneling microscopy and (b) atomic force microscopy. In STM, a metal probe tip is brought into proximity to a conductive sample, which forms a circuit that is used to control the separation and interactions. In AFM, the tip is typically mounted on a cantilever and forces between the tip and surface are monitored using the mechanical properties of the cantilever. The junction of a tip and a planar surface contains information about electronic electromagnetic, optical, thermal, and chemical properties. These properties can be accessed by stimulating the junction with various perturbations and quantifying the response (c). [(c) is courtesy of Stephen Jesse].

In traditional scanning probe microscopy (SPM) applications, instrumental conditions are set such that one or another contribution dominates the interaction, greatly simplifying the analysis. The reader is referred to several texts for introductory concepts on tunneling microscopy, atomic force microscopy, and electrostatic and magnetic force microscopy (Weisendanger, 1994, 1998; Bonnell, 2000; Bai, 2000; Chen, 2008). Strategies to extract complex properties include modulating signals between the sample and tip, utilizing multiple frequencies, independently varying gradients across samples, and combining, for example, optical and electrical probes. Figure 2(c) conceptually suggests how multiple signals can be introduced and/or detected from a tip-surface junction. It is this concept that is implemented in many variants to realize extraction of complex properties and local interactions. This review will focus on those advances that extend probes into the three-dimensional (3D) space of Fig. 1 by pushing the limits of probing function at nanometer-scale spatial resolution. In the process, the impact of understanding several important scientific issues will be illustrated, including molecular interface contact, superconductivity, electron spin, plasmon field focusing, surface diffusion, bond vibrations, and phase transformations.

Section II focuses on properties that can be determined by imposing a time-varying electrical field between the tip and sample. The resulting properties are continuum in nature (resistance, capacitance, dielectric function), but in some cases, atomic resolution is nonetheless achieved. The examples used here also illustrate a strategy to isolate complex properties, an approach to accessing real and imaginary components of a property, and an explanation of the unexpectedly high spatial resolution. In Sec. III, the atomic spatial resolution of STM is exploited to make novel spectroscopic measurements. Advances in instrument stability and energy resolution enable electronic structure characterization that can be used to examine electron interactions in solids and to manipulate atoms and molecules. While STM has been a staple of the surface chemistry toolbox for two decades, developments now enable analyses of more complex surface reactions. Approaches to examining reactions at the high pressures more relevant to realistic reactions are illustrated. Section IV explores how correlated electron interactions in solids can be probed to gain insight on fundamental aspects of superconductivity and magnetism. Atomic forces are now used routinely in a large family of tools, but the control needed to achieve atomic-scale 3D force profiles above a surface is extreme. Section V shows how this control can be used to identify atoms from atomic forces. One powerful strategy for accessing complex properties is to utilize light-matter interactions. New strategies for near-field optics, optical antennas, and near-field spectroscopy are reviewed in Sec. VI. The probing of electromechanical interactions illustrates a new level of complexity in that the tip is interacting with a tensor property of the material. A summary of the impact of these advances is followed by projections of future developments in the field.

The emphasis of this review is on the application of local probes to physical phenomena rather than on instrumentation,

although instrumentation factors are often critical to success. In all cases, the reader is referred to additional resources. Since space limitations preclude inclusion of all techniques and even all variations of approaches, we refer readers to a number of monographs on specialized topics throughout the text and in the Summary.

II. SPATIALLY RESOLVED ELECTROMAGNETIC PROPERTIES: FROM CONDUCTANCE TO DIELECTRIC FUNCTION

After over 25 years of routine application of STM at atomic resolution, it is not surprising to find that properties accessed through variants of STM achieve atomic resolution as well. Elegant examples are discussed in Secs. III and IV. Perhaps more surprising is the spatial resolution achieved recently in probing continuum properties such as resistance, capacitance, dielectric function, electromechanical coupling, polarizability, etc. (Bonnell, 2008; Brukman and Bonnell, 2008; Moore *et al.*, 2010) This level of resolution can be a consequence of the behavior of the sample, such as localized phase transformations, or of dimensionality constraints. Alternatively, resolution is a consequence of instrumentation advances, for example, exploiting multiple modulations and high-order harmonics in tip-surface response functions.

Most force-based scanning probes of electronic and dielectric properties involve a conducting tip and application of an electrical signal to the tip-surface junction (Bonnell and Shao, 2003). In some cases, this is done with the probe tip in contact with the surface yielding, for example, scanning resistance, capacitance, and piezoforce microscopies. In other cases the tip is above the surface leading to potentiometry, Kelvin probe microscopy, etc. Considering these probes in terms of combinations of contact condition, applied fields, and detection mechanisms allows a variety of both simple and complex functions to be isolated.

A. Isolating local properties

A basic approach to isolating properties is illustrated in a comparison of surface potential–Kelvin probe and capacitance probes. When a tip is above the surface and a static and a periodic field are applied, the resulting force at the tip is a nonlinear function that can be detected via the motion of the cantilever. The cantilever will oscillate in response to the periodic force. The force $F = \frac{1}{2}V^2\delta C/\delta z$, where V is the applied voltage, C is the capacitance between the tip and bottom electrode (usually below the sample), and z is the distance between the sample and tip. With a sinusoidal voltage applied, V_{ac}, the force has a dc component and components at higher resonant frequencies. The first- and second-order components of the total function can be used to isolate properties. The first-order harmonic of the force due to a periodic electrical field is $F = (\delta C/\delta z)\times[\frac{1}{2}(V_{dc\ tip}V_{dc\ surface})^2 V_{ac}\sin(\omega t)]$, where V is the dc voltage on the tip and surface, respectively. Superimposing a dc bias at the junction and adjusting the magnitude until it is equal to the surface potential results in zero force at the frequency of the first-order harmonic. This detection scheme can be used to map the surface potential (which is related to the work function under ideal conditions) under the tip and is the basis of scanning surface potential microscopy or Kelvin probe microscopy, which is routinely used in surface characterization.

The force at the second-order harmonic of applied bias is related only to the capacitance as $F = \frac{1}{4}(\delta C/\delta z)\times[V_{ac}^2\cos(2\omega t)]$. The contribution to the capacitance can be isolated by detection at the second-order harmonic. In the ideal case of a flat surface, this yields the dielectric constant at the frequency of the oscillation. For example, Brukman and Bonnell (2008) applied this to thin oxide films used in microelectronics and demonstrated sensitivity in the dielectric constant of 0.1 and spatial resolution limited by separation and on the order of tens of nanometers.

This comparison of well-known techniques illustrates how applying a single-frequency electrical signal to a tip not in contact with the surface, detecting the mechanical oscillation of the cantilever, and measuring at two harmonics of the frequency isolates potential (work function) and capacitance (dielectric constant). An obvious extension is to vary the frequency of the applied bias systematically to extract a dielectric function. Extending this strategy to different variations of contact, applied field, and detection schemes leads to probes of an immense range of local properties. Table I illustrates the range of phenomena that can be probed in this manner. Here we focus on those that push the limits of resolution or complexity, enabling access to physical phenomena at new levels.

B. Conductance, resistance, and capacitance at nanometer-scale spatial resolution

Scanning spreading resistance microscopy (SSRM) (Eyben *et al.*, 2004), scanning conductance microscopy, and scanning capacitance microscopy (SCM) are techniques that probe local properties, utilizing a tip that is in contact with a surface (Martin, Abraham, and Wickramasinghe, 1988; Williams, Hough, and Rishton, 1989; Park *et al.*, 2006). In these techniques a dc or an ac electrical signal is applied to the tip and the current detected as the tip scans. Knowing the voltage, the current can be related to resistance or conductance in the dc case and capacitance in the ac case. These approaches are useful in mapping dopant concentration variations in semiconductors. Recently, lateral resolution approaching 1 nm was achieved with SCM (Eyben *et al.*, 2004) in imaging localized electronic states near a SiO_2 surface in ultrahigh vacuum (UHV). Noncontact microwave-frequency ac STM was used to map individual buried dopant atoms in certain cases (Weiss and McCarty, 2003). Spatial resolution in the <5 nm range was demonstrated for SSRM in air on InGaAs quantum well structures (Douheret, Bonsels, and Anand, 2005), and 1–3 nm reproducibility was demonstrated on p- and n-MOS (metal oxide semiconductor) structures (Martin, Abraham, and Wickramasinghe, 1988; Eyben, Janssens, and Vandervorst, 2005).

Spatial resolution of <1 nm in scanning conductance microscopy is illustrated on a HfO_2 thin film on Si in Fig. 3. The reported resolution in all of these cases is better than that expected given the size of the probe tip and a question arises as to the origin of this high spatial resolution. For the data in Fig. 3(a) the contact radius is estimated to be 4–5 nm. The

TABLE I. Properties and modulated operation modes of scanning probes.

Technique	Mode[a]	Property
Atomic force microscopy	c, nc/ic, mech/osc phase/amp/FM mode	van der Waals forces, chemical forces, electrostatic interactions, topography
Electrostatic force microscopy	nc, mech, phase/amp/FM	Electrostatic force
Magnetic force microscopy	nc, mech, phase/amp/FM	Magnetic force
Scanning surface potential (Kelvin force microscopy)	nc, elec, 1st harmonic	Potential, work function Adsorbate enthalpy/entropy
Scanning capacitance microscopy	c, F, cap sensor	Capacitance, relative dopant density
Scanning capacitance force microscopy	c, elec, 3rd harmonic	dC/dV, dopant profile
Scanning spreading resistance microscopy	c, F, dc current	Resistivity, relative dopant density
Scanning gate microscopy	nc, elec, amp	Current flow, local band energy, contact potential variation
Scanning impedance microscopy	nc, elec, phase/amp	Interface potential, capacitance, time constant, local band energy, current flow (in combination w/SSPM)
Scanning tunneling microscopy	nc, dI/dV	Topography, local density of states, maps with gate voltage, bias, and magnetic field, dispersion, phonons and spin excitations, spatial spin contrast, local hysteresis
Microwave-frequency ac STM	nc, 1st or 3rd harmonic, mdf	Polarizability, dopant profile, dielectric response
Scanning near-field optical microscopy	c, nc/ic	Frequency-dependent dielectric function, surface polaritons, Rayleigh scattering, IR absorption, fluorescence
Nano-impedance spectroscopy	c, F, freq spectrum	Interface potential, capacitance, time constant, dopant profiling
Piezoforce microscopy	c, elec, phase/amp c, elec, 2nd harmonic	d_{33} Switching dynamics, relaxation time, and domain nucleation
Scanning nonlinear microscopy	c, F, 1st or 3rd harmonic	dC/dV, dielectric constant
Near-field microwave microscopy	c, F, phase	Microwave losses, d_{33}
Tip-enhanced Raman scattering	Local field enhancement	Raman scattering

[a]Mode: amp = detection of amplitude at preset frequency; c = contact; nc = noncontact; ic = intermittent contact; mech = cantilever is driven by a mechanical oscillation; elec = cantilever is driven or responds to an oscillating electrical signal; F = constant force feedback; FM = feedback on constant shift of the resonant frequency; osc = oscillate magnetized tip by external magnetic field to avoid a ''forest'' of peaks due to the liquid cell; and phase = detection or feedback on phase; mdf = microwave difference frequency.

reduction of the tip-surface interaction size from the contact diameter by a factor of 8–10 indicates the existence of a field-focusing mechanism. Bonnell and co-workers (Brukman and Bonnell, 2008; Nikiforov *et al.*, 2008a) consider two potential focusing effects: localized phase transformation and an elastic strain-induced conductivity increase. Bonnell and co-workers note that the stress distribution underneath the tip-sample junction is not uniform, with a region with half of the contact zone experiencing 50% greater stress than the nominal compressive load (Douheret, Bonsels, and Anand, 2005). The calculated enhanced loads for various experimental conditions were related to the pressures at which the two mechanisms could operate; see Fig. 3(b). An ~10 GPa load results in a decrease of 0.15 eV or about 10% of the Si band gap. At higher pressures, Si undergoes a phase transition from semiconducting diamondlike face-centered cubic (fcc) to conductive tetragonal β-Sn. Figure 3 demonstrates that the presence of a field-focusing mechanism, in this case mechanical strain, enables spatial resolution that far exceeds that expected from tip dimensions.

The examples above take the detection of continuum electrical and mechanical properties to unprecedented spatial scales. These probes can also, at times, access fundamental properties. Note again that capacitance can be directly accessed from the second-order harmonic of the ac signal. In some nanostructures (e.g., wires, tubes, dots), low dimensionality provides constraints that enable access to quantum behavior. In addition to a dielectric constant, the capacitance can include contributions from quantum capacitance, Coulomb blockades, abrupt variations and singularities in densities of states, etc. Dresselhaus and colleagues (Gekhtman *et al.*, 1999) probed quasi-one-dimensional confined states in bismuth quantum wires. By standing bismuth nanowires on end, they reproduced the particle-in-a-box configuration and used a dc-biased tip in noncontact AFM (nc-AFM) to map charge density within the well. In addition, cantilever frequency shift versus tip bias spectroscopy showed that the Bi wire thermodynamic density of states increasingly deviates from continuum predictions as the radius decreases, consistent with phonon-assisted shifts at the Fermi level.

C. Scanning impedance: The next level of complexity

Introducing frequency variation to local electrical measurements provides a path to access increased information about the sample. Impedance is the ratio between the applied voltage variation and current response $Z(w) = V(w)/I(w) = lZl\exp(i\theta)$. Accessing the frequency-resolved impedance

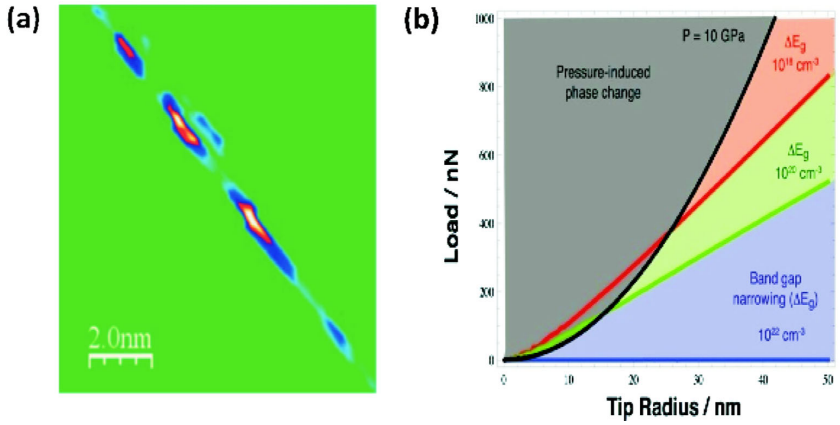

FIG. 3 (color online). (a) A scanning conductance image of defects in a HfO_2 thin film on a Si substrate, demonstrating subnanometer spatial resolution of enhanced current (~ 5 pA) at defects and (b) a mechanism map relating experimental tip-contact conditions to strain-induced conduction variations in Si. From Nikiforov *et al.*, 2008.

amplitude Z and phase ϕ provides information about the resistance, capacitance, and relaxation times associated with transport processes. For example, electron trap state lifetimes at interfaces or ion diffusion in solids can be quantified. Scanning impedance microscopy (SIM) can be done in noncontact mode, where the voltage modulation is across the sample of interest (Kalinin and Bonnell, 2002). Alternatively, it can be done in contact or near-contact mode, which is analogous to macroscopic impedance spectroscopy and is referred to as nano-impedance microscopy (NIM) or nano-impedance spectroscopy (Shao *et al.*, 2003). Figures 4(a) and 4(b) illustrate NIM configurations with a bottom electrode and with a surface electrode. The real and imaginary components of the impedance can be monitored as a function of voltage modulation frequency applied to the tip. The resulting semicircles in the spectra are associated with variations in transport processes, for example, at electrode interfaces, within a perfect crystal, at internal boundaries, etc. As with macroscopic impedance spectroscopy, the spectra are interpreted with equivalent circuit models, examples of which are shown in Figs. 4(c) and 4(d). Shao *et al.* (2003) measured the tip dc voltage dependence on spectra in polycrystalline ZnO varistors for both configurations and were the first to image the phase and amplitude. Figure 4(d) illustrates a case where grain boundary and electrode interface impedances are determined. O'Hayre, Lee, and Prinz (2004) and O'Hayre *et al.* (2004) measured the effect of contact force, and consequently tip area, on the impedance spectra; see Fig. 4(e). They developed a relationship between force and contact area that can be used to quantify local impedance.

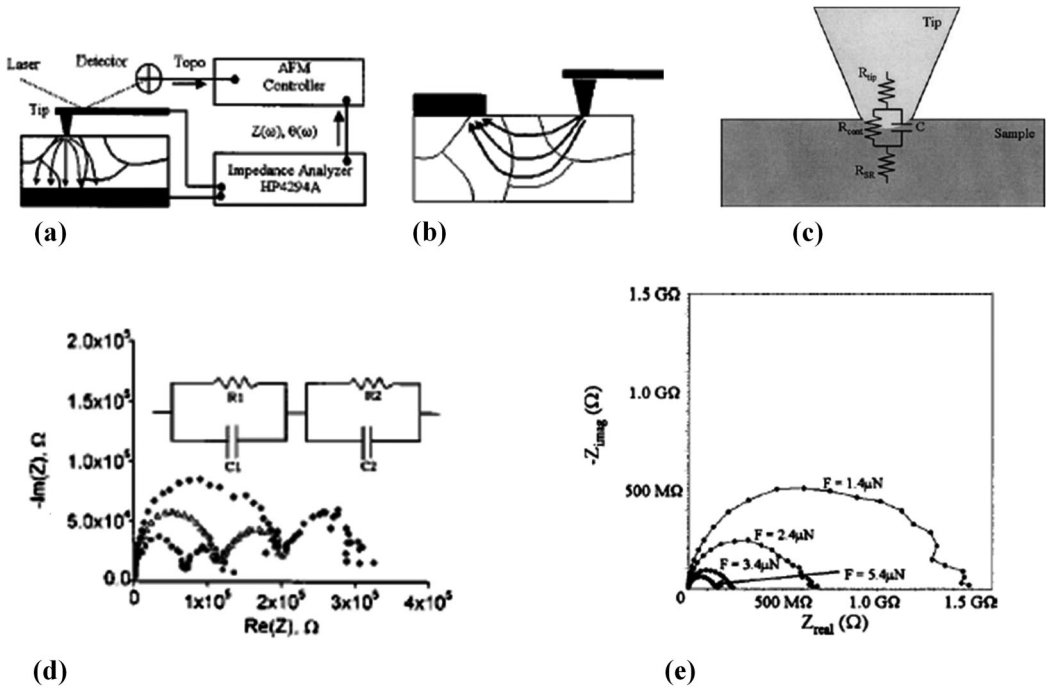

FIG. 4. Nano-impedance spectroscopy. Schematic diagrams of NIM configurations. The tip acts as an electrode in a (a) vertical or (b) lateral configuration. (c) A simple equivalent circuit for the tip-surface junction. Two examples of local impedance spectra, (d) one with multiple interfaces in the current path and (e) one with a single interface. (a)–(c) From Shao *et al.* (2003); (d), (e) from O'Hayre *et al.*, 2004.

Figure 5 shows three examples of imaging local impedance that illustrate different aspects of capability. Figure 5(a) examines defects in a single-walled carbon nanotube device (Freitag *et al.*, 2002). In SIM, a modulated current flows through the tube, the magnitude of which is recorded at the electrodes as a biased tip scans the surface. The field of the tip locally influences the band energies of the tube. The band energies at a defect differ from those of a perfect structure; the specific differences are associated with the character of the individual defect. When the electric field of the tip pushes the valence band below the Fermi level in this case, the defect becomes a locally insulating electron scattering center. The tip voltage dependence of the SIM contrast can be used to determine the valence band energies of each defect, with 3 meV energy resolution. McEuen and co-workers (Woodside and McEuen, 2002) used alternating sample biases to induce and to detect single-electron charging of such defects, which act as quantum dots within the nanotubes.

One of the early constraints of SIM and NIM is that stray capacitance contributes significantly (10–100 pF) to the signal and limits sensitivity. Pingree and Hersam (2005) and Pingree *et al.* (2009) developed a variable resistance and capacitance circuit that, when inserted into the NIM control system, reduces stray capacitance by five orders of magnitude. Figure 5(b) compares the magnitude (top) and phase (bottom) of a MOS test structure with (left) and without (right) the correction circuit. This dramatic improvement in sensitivity enables the technique to be used on a much wider range of systems.

Using a similar approach, referred to as nanoscale scanning capacitance microscopy, Fumagalli *et al.* (2009) mapped the dielectric properties of single layers of purple membrane fragments. Figure 5(c) shows the topographic structure (top) and the capacitance (bottom), which is measured with noise level in the range of 100 zF. The dielectric constant $\varepsilon(x, y)$ was determined from

$$\varepsilon(x, y) = \frac{h(x, y)}{h(x, y) - z_0 + \frac{R(1-\sin\theta)}{\exp\left(\frac{\Delta C(x,y,z_0)}{2\pi\varepsilon_0 R}\right)\left(1+\frac{R(1-\sin\theta)}{z_0}\right)-1}},$$

where Z_0 is the scan height, and R and V are geometric parameters of the tip. Once the tip parameters are known, the capacitance image can be transformed into a dielectric property map.

D. Surface potential at atomic and molecular resolution

As noted, scanning surface potentiometry (SSPM) and Kelvin force microscopy (KFM) access properties related to surface work function and recent results demonstrate single-molecular-layer and atomic spatial resolution. As an example, a critical issue in organic electronics is the state of the interface between the electrode and the organic films. The determination of the electronic structure at these interfaces is usually accomplished with photoemission and similar spatially averaging measurements. In other words, the molecular orientation is not directly determined. Nikiforov *et al.* (2008) used surface potential and a Kelvin probe to determine the

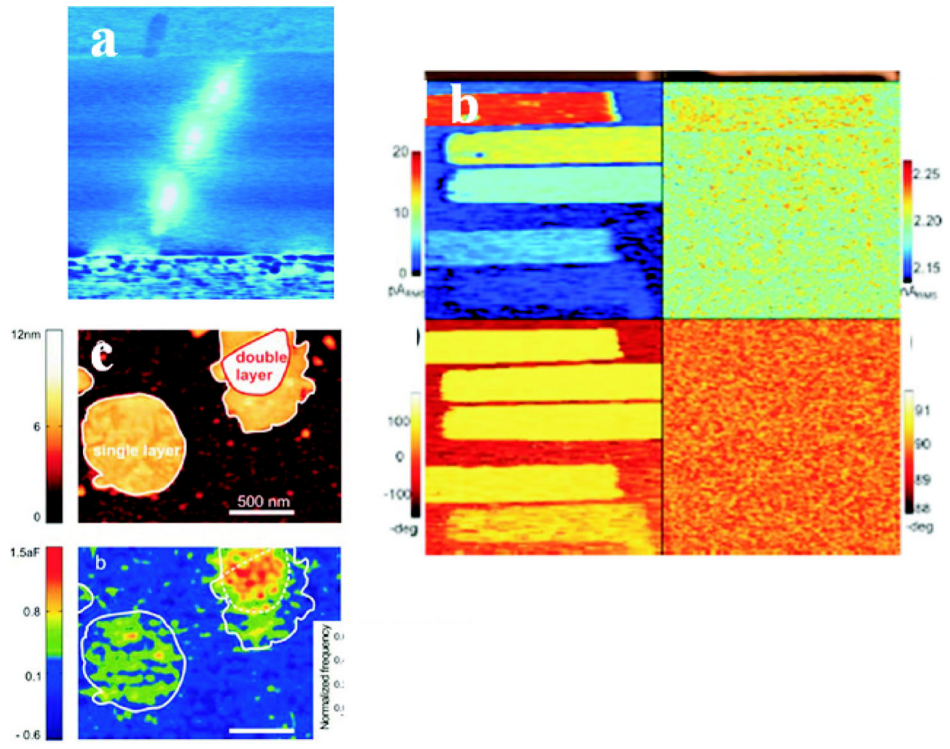

FIG. 5 (color online). Complex properties from modulated tip bias techniques. (a) Scanning impedance image of a single nanotube with defects in which contrast is related to the valence band energy of each individual defect. From Freitag *et al.*, 2002. (b) Comparison of bridge-enhanced nano-impedance microscopy amplitude and phase images (left) with uncorrected NIM (right) demonstrating five orders of magnitude increase in sensitivity. From Pingree and Hersam, 2005. (c) Topographic image (top) and single-frequency capacitance (bottom) of single and double purple membrane layers. From Fumagalli *et al.*, 2009.

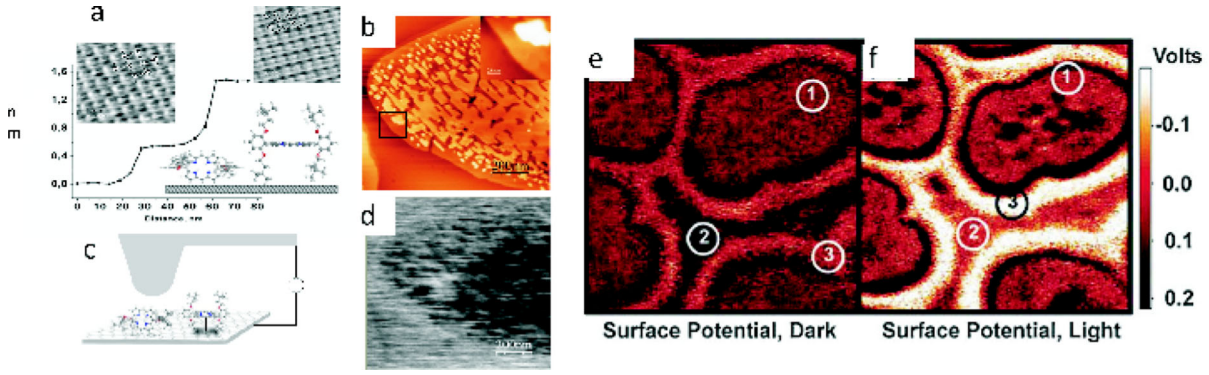

FIG. 6 (color online). Scanning surface potential and Kelvin force microscopy. (a)–(c) Potential measurement of single molecular layers; (d), (e) Potential variation with charge generation. (a) nc-AFM images of the structure of assembled monolayers of a Zn porphyrin on graphite. (b) Comparison of the topographic structure and (c) the surface potential. (d) Comparison of surface potential in the absence and (e) presence of optical illumination of a polymer blend. (a)–(d) From Nikiforov *et al.*, 2009. (e), (f) From Chiesa *et al.*, 2005.

effect of molecular orientation on work function at an electrode by probing a single molecular layer with known structure. A monolayer of a porphyrin complex deposited on highly oriented pyrolytic graphite in UHV assembles into islands with (see Fig. 6) two molecular orientations. The structures of the two types of monolayers were determined with nc-AFM [see Fig. 6(a)], and variations in surface potential were correlated with the structures of the monolayers. The potential difference between the substrate and the molecule oriented with the porphyrin ring perpendicular to the surface was negligible but that of the molecule oriented with the ring parallel to the surface was 0.6 eV; see Fig. 6(d). The π orbitals of the porphyrin and underlying substrate facilitate charge delocalization and a dipole is established that influences the local potential. That electrode-molecule contact properties are strongly dependent on orientation has tremendous implications in device design (Nikiforov *et al.*, 2008). It is also an example of the ability to measure the potential of a single molecular layer.

Figures 6(e) and 6(f) illustrate how surface potential can be used to map charge generation (Chiesa *et al.*, 2005). An AFM is configured on top of an inverted optical microscope and a photoactive sample is fabricated on a transparent substrate. Chiesa *et al.* (2005) used this configuration to characterize heterojunction photovoltaics, in this case a blend of donor and acceptor polymers that phase separate. Upon optical excitation, electron-hole pairs are created and dissociate at internal donor-acceptor interfaces. The spatial variation of charge carriers is evident in the surface potential signal and the differences between the illuminated and nonilluminated conditions provide insight into the transport processes.

Eguchi *et al.* (2004) imaged the surface potential of Ge(105)-(1 × 2) at atomic resolution. By comparing STM, nc-AFM, and theoretical calculations, an atomic model for the surface structure was developed that involves interactions among dangling bonds. The atomic-resolution surface potential map provides strong evidence of charge transfer between dangling bonds. More recently, Besenbacher and co-workers (Enevoldsen *et al.*, 2008) detected surface potential variations on TiO_2(110) with atomic resolution. The nc-AFM images in Fig. 7(a) illustrate the well-understood bridging row surface structure; in-plane Ti is at a lower position than the rows of oxygen that are on top of half of the Ti. Local potential variations on the order of 20 meV [see Fig. 7(b)] are associated with the Ti and O, with the oxygen rows exhibiting a more negative potential. The differences with respect to scan direction are a consequence of asymmetry in the trip structure [see Figs. 7(c)–7(g)]. The schematic sequence of tip interactions at various positions relates the measured surface potential to the surface atomic structure and chemical identity of atoms at the surface.

E. Toward measuring dielectric function at high spatial resolution

Linear and nonlinear dielectric properties are a measure of polarization on several length scales in a crystalline solid. At the smallest scale, atomic polarization occurs as electron charge density is distorted by an electric field. At larger scales, electric dipoles due to relative positions of anions and cations in the crystal unit cell couple in a manner that influences the alignment. The dielectric function that encompasses these interactions is inherent in capacitance and in light scattering. An approach to probing dielectric constant with a noncontact technique was mentioned above; however, the required sample-tip separation may ultimately limit spatial resolution. Several recent advances point to new avenues toward probing this complex function. Three are summarized here: backscattering of light from a tip, a local resonator, and microwave probes.

The dielectric function is an inherent component of scattering of light from a surface. Accessing scattering at a tip-surface junction takes advantage of the near-field focusing effects discussed in Sec. VI. Using similar instrumentation pioneered by Hillenbrand and Keilmann (2000), an analysis was done to determine whether the dielectric function of a single molecular layer could be isolated from optical scattering and, if so, at what sensitivity (Nikiforov *et al.*, 2009). Harmonics up to fourth order of light scattered from a tip-surface junction were detected to probe properties on idealized samples of monolayers of organic molecules on atomically smooth graphite substrates; see Fig. 8. The response functions and, therefore, the properties of the graphite surface and the porphyrin-graphite complex were compared. Extending earlier models, Nikiforov *et al.* calculated the intensity of

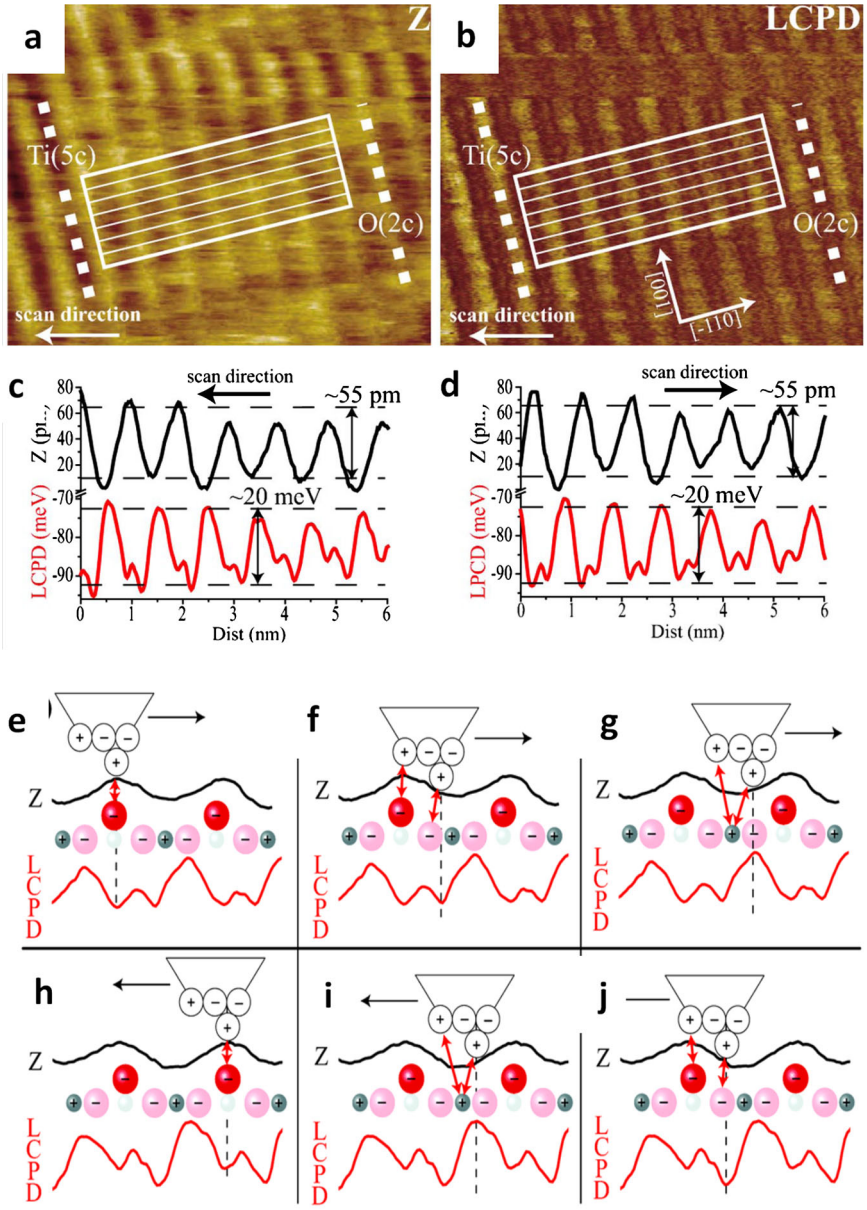

FIG. 7 (color online). (a) Noncontact AFM topography image, area 10×8 nm^2, $\Delta f \cong 121$ Hz, $A_{p-p} \cong 28$ nm, $f_0 = 70$ kHz, $f_{\text{mod}} \cong 452$ kHz, and $U_{\text{ac}} = 0.3$ V. (b) Simultaneously recorded potential. (c) Average twin cross sections of topography and potential, as indicated by the boxes in (a) and (b). (d) Schematic snapshot sequences of the AFM tip tracing in (a)–(c): left to right, and (d)–(f): right to left directions. Cutouts of the experimentally recorded cross-section graphs are superimposed onto the models in (d)–(f) and (a)–(c), respectively. Double arrows indicate the key electrostatic tip-surface interactions. From Enevoldsen *et al.*, 2008.

scattered light, accounting for the nonlinear enhancement of the electric field when the tip-surface distance is extremely small and included time variation in the tip-sample distance, and applied this to a sample consisting of a substrate and a thin film. They determined that the third-order harmonic of the scattered light was the most sensitive and could be used to determine local differences in the dielectric constant of 0.5. These results represent the first spatially localized quantification of both the real and imaginary contributions to the dielectric function of a single molecular layer, demonstrating single-monolayer detection with ~10 nm lateral resolution.

Cho and Hirose (2007) developed an alternative probe of dielectric properties that utilizes a resonator circuit at a tip-surface junction, referred to as scanning nonlinear microscopy. This configuration differs somewhat from that of conventional STM or AFM as shown in Fig. 9. A tip is in the center of a metallic ring that measures local capacitance; an *LC* resonator is inserted into a feedback loop with an oscillator tuned to the same frequency. Variations in capacitance under the tip modulate the oscillating frequency. The frequency is demodulated to produce a voltage proportional to the variation in capacitance. The resonator probe achieves four orders of magnitude increase in sensitivity compared to typical scanning capacitance microscopy. Figure 9 shows a schematic of this approach. To access nonlinear dielectric properties, they consider an expansion of the electrical displacement D as a function of the electric field E:

$$D_3 = P_3 + \varepsilon(2)E_3 + \tfrac{1}{2}\varepsilon(3){E_3}^2 + \tfrac{1}{6}\varepsilon(4){E_3}^3 + \cdots,$$

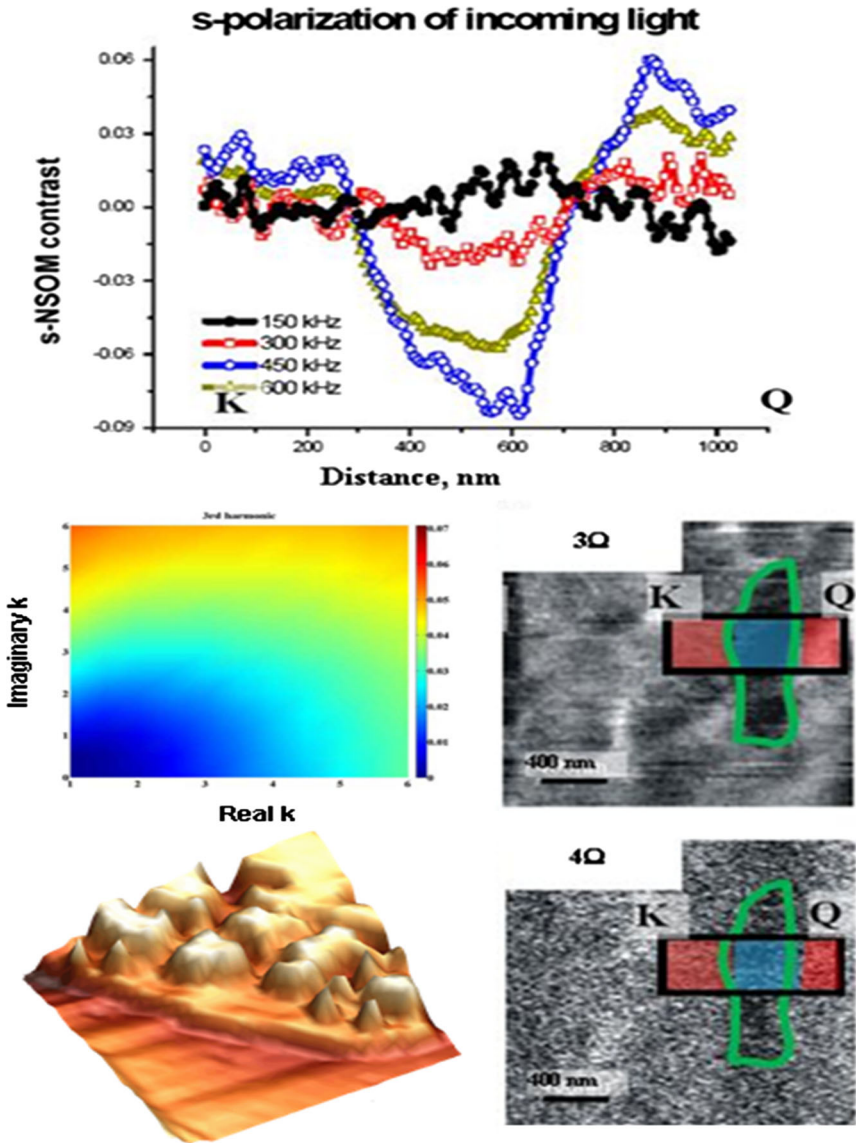

FIG. 8 (color online). High-order harmonic detection in *s*-NSOM to determine the dielectric function is illustrated with scattering of *s*-polarized light at four frequencies from a graphite-porphyrin sample. Profiles (top) across a molecular monolayer island are compared. The calculation of image contrast dependence on the dielectric function at the third-order harmonic (middle) can be used to relate scattering variations (right images) to properties. From Nikiforov *et al.*, 2009.

where $\varepsilon(2)$, $\varepsilon(3)$, and $\varepsilon(4)$ are the linear and higher-order dielectric constants. The even-rank tensors are insensitive to the polarization state; however, the odd-rank tensor is very sensitive to spontaneous polarization. Therefore, detecting the third term in the equation can distinguish, for example, positively and negatively poled ferroelectric domains. The ratio of capacitance change to static capacitance is

$$\frac{dCs}{dCs0} = \frac{\varepsilon(3)}{\varepsilon(2)} Ep\cos(\omega t) + \frac{1\varepsilon(4)}{4\varepsilon(2)} Ep^2\cos(2\omega t) + \cdots$$

and illustrates that these terms might be isolated by detecting the fundamental and second-order harmonic of the applied electric field. The phase at the fundamental frequency is related to the orientation of the polarization vector, and could, for example, map the orientations of ferroelectric domains. Figure 10 illustrates simultaneous atomic resolution of structure (a) and polarization (b) on a Si surface. The authors note that noncontact imaging must be done in UHV since the dielectric constant of ambient water precludes sample characterization under ambient conditions.

Tseleva *et al.* (2007) recently incorporated frequency variation in the GHz regime and determined dielectric properties of oxide thin films at various frequencies. To date, spatial resolution at these higher frequencies has been on the micrometer scale using this technique.

F. Locally resolved photoconduction

The nanoscale effects of photoexcitation have been targeted for investigation for 25 years (Walle *et al.*, 1987; Grafström, 2002). A key complication in this area has been that thermal expansion of the sample and the probe tip can be mistakenly interpreted as enhanced conduction. Hamers,

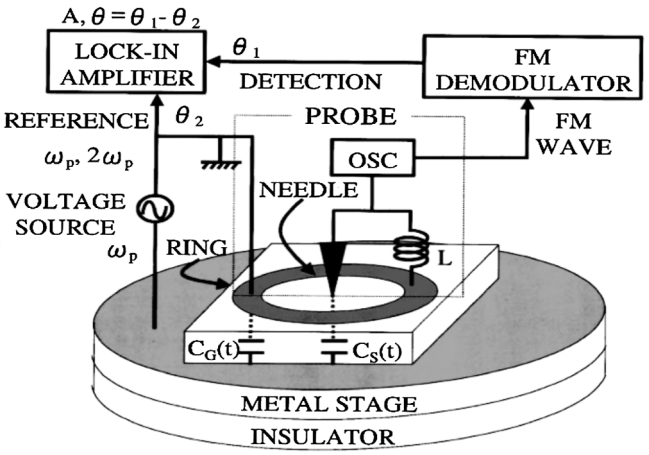

FIG. 9. A diagram of a scanning nonlinear dielectric microscope illustrating the inclusion of a resonator at the tip-surface junction. From Tanaka *et al.*, 2008.

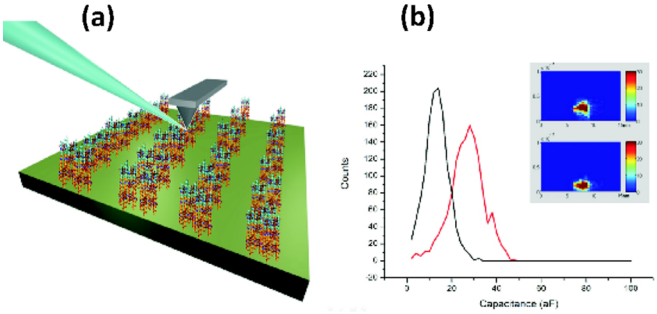

FIG. 11 (color online). (a) A schematic diagram of patterned peptides on a graphite substrate with light incident on the tip-surface junction. (b) The effect of optical illumination on the capacitance of the monolayer porphyrin containing peptides is illustrated as 2D and 3D histograms. The top 3D histogram in the inset shows the properties with illumination, the bottom without illumination. In the 2D histogram the curve on the right is with illumination, and the curve on the left is without exposure. $\lambda = 425$ nm. From Kathan-Galipeau *et al.*, 2011.

Kuk, and others explored local surface photovoltage effects in semiconductors (Kuk *et al.*, 1991; McEllistrem *et al.*, 1993; Grafström, 2002). The controversies in how measurements are best made, what effects are due to the electric field applied by the probe tip, and other issues highlight some of the difficulties in simple interpretations of such approaches.

To avoid illuminating the tip-sample junction directly, the Kretschmann-Raether configuration for evansescent coupling via total internal reflection was developed for STM by Scherer and co-workers (Feldstein *et al.*, 1996). It can be challenging to prepare high-quality substrates for such experiments. The photoconductance of isolated molecules and photoreaction of pairs of molecules held in a high-quality self-assembled monolayer matrix has been measured using this approach (Kim *et al.*, 2011). Using defects in alkanethiol monolayers on Au{111}, 9-phenylethynylanthracene disulfide was inserted such that pairs of the thiolate were held proximate and in place. The molecules were observed before and during photoexcitation, as well as before and after dimerization by a [4 + 4] cycloaddition. While changes in conductance of the photoabsorbing conjugated molecules were observed upon illumination, no changes were observed in the conductance of the nonabsorbing matrix molecules. This configuration could be used for measuring and optimizing the absorption spectra and photoconversion of molecules for organic and other solar cells.

Extending beyond STM-related techniques, Kathan-Galipeau *et al.* (2011) combined scanning impedance microscopy with optical excitation to quantify polarization in single molecular layers of porphyrin peptides. Challenges in obtaining quantitative results include peptide design that leads to controlled interface structure, the stray capacitance mentioned above, and the requirement not to damage the biomolecules during analysis. Using capacitance compensation strategies similar to those of Pingree and Hersam (2005) and torsional force stabilization of the AFM tip to control contact pressure, they examined microcontact patterned peptides designed to self-assemble on graphite substrates. The impedance approach allows both electron transport and dielectric function to be probed simultaneously. Figure 11 illustrates the experimental configuration and shows histograms of the capacitance in the absence and presence of optical excitation with a wavelength corresponding to absorption in the porphryin. The capacitance increase is due to the change in polarization volume in the excited state. The quantitative comparison between the ground-state and excited-state polarization volumes provides a measure of coupling between the porphyrin complexes within the molecule. This example illustrates again how a combination of multiple stimuli and detection paradigms can yield fundamental and complex property functions at the molecular scale.

Similar to the ability to probe trap state lifetimes in SIM, the combination of scanning KFM (SSPM) or electrostatic force microscopy (EFM) with optical excitation can provide insight into charging rates. This is of great utility in the study of photovoltaics, which are usually heterogeneous in composition, structure, and function. This approach was first

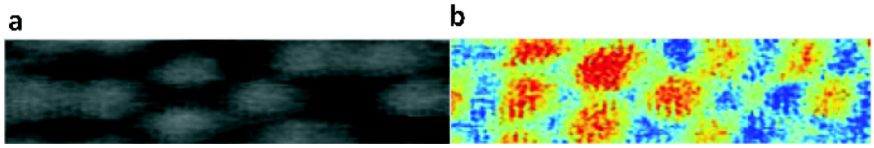

FIG. 10 (color online). In nc-AFM, atomic resolution is achieved both in (a) the topography image, which is the $\varepsilon(4)$ feedback signal and in (b) the nonlinear dielectric constant image $\varepsilon(3)$. The familiar Si(111)-(7 × 7) surface is used to demonstrate the resolution. There is a direct correlation between the Si adatom locations and the contrast in the $\varepsilon(3)$ signal. This implies that the atomic polarization of the Si bonds is probed here. From Tanaka *et al.*, 2008.

demonstrated by Coffey and Ginger as illustrated in Fig. 12. The configuration is similar to that in Fig. 6, i.e., the sample is illuminated from below and probed from above; see Fig. 12(a). In this case, the EFM signal is monitored after the light is switched off and the signal decay is quantified. Figure 12 shows results for a polymer blend that is a model system for photocells. When illuminated, charge builds up in the sample under the tip, it is detected as a change in force. Once it reaches saturation, the light is turned off and the exponential decay is recorded and fitted [see Fig. 12(b)], and plotted for each pixel [see Fig. 12(e)]. The charging rate can be compared to the external quantum efficiency [see Fig. 12(c)] and topography [see Fig. 12(d)]. Interestingly, the charging and efficiency were found to be slowest at the boundaries.

G. Opportunities for functional probes

The results discussed above exemplify how local electromagnetic properties can be probed in an AFM configuration

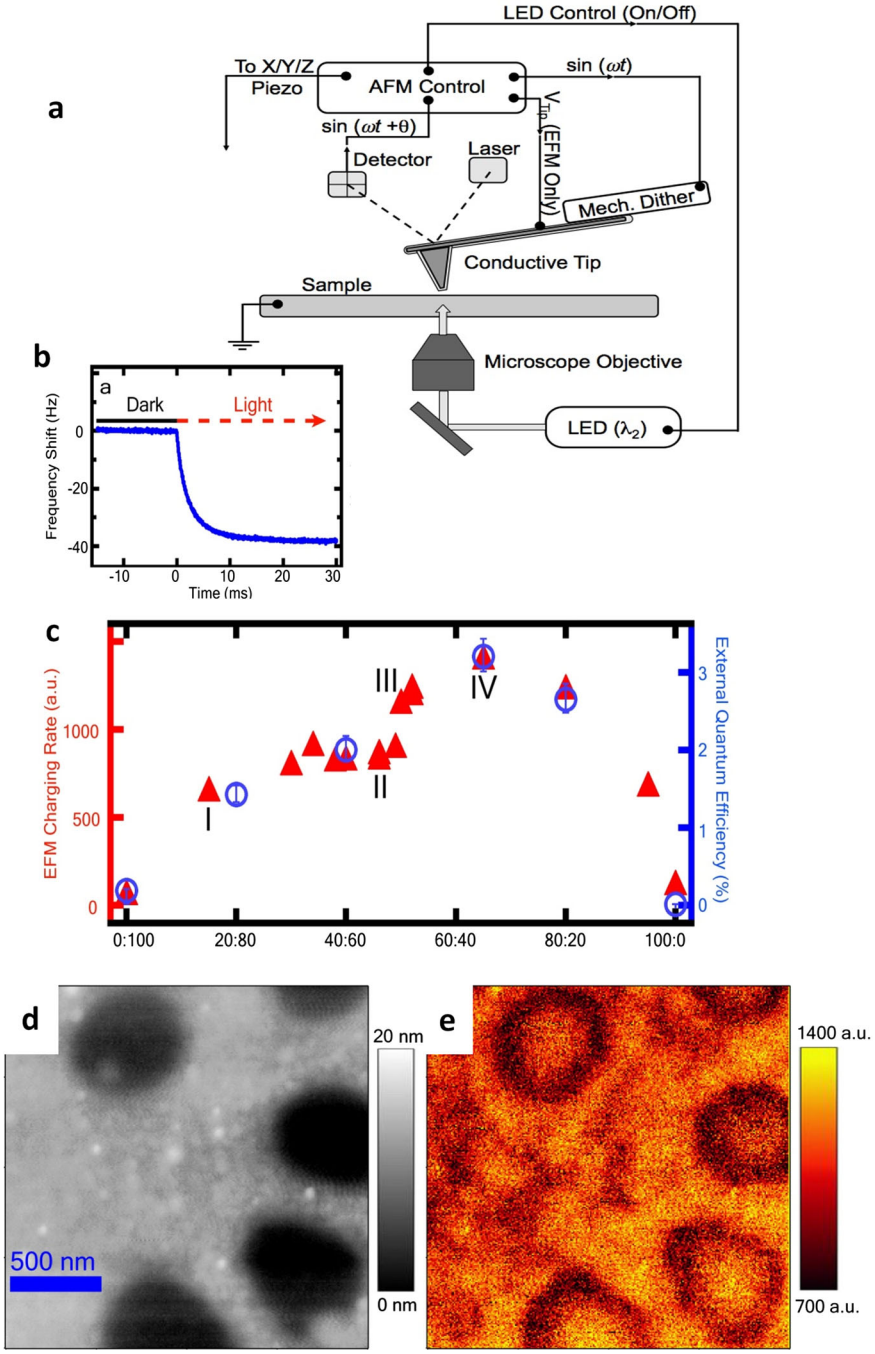

FIG. 12 (color online). Charge dynamics in a polymer blend solar cell. (a) The sample is illuminated from the bottom through a transparent substrate. (b) The EFM signal is monitored after the light is switched off, and (e) the exponential decay constant is plotted for each pixel. (c) This is compared with the quantum efficiency. (d, e) Images of topography and the charging rate, respectively. From Coffey and Ginger, 2006.

modified to exploit the complexity of interactions at a tip-surface junction. They illustrate a trend of increasing spatial resolution and increasing capability to quantify local properties. Other variants of these approaches have been developed. Notably, scanning gate microscopy has been useful in characterizing nanostructured devices. This technique implements EFM or SIM with a back gate under the structure, analogous to a transistor configuration; see, for example, Bachtold *et al.* (2000), Bockrath *et al.* (2001), Freitag *et al.* (2002), Hsu *et al.* (2003), Aoki *et al.* (2005), and Yang, Zhong, and Lieber (2005). Photoconductive SPM, similar to the optical techniques described above, is increasingly used to characterize photovoltaic devices. Notably, modifications of STM have been developed to operate at microwave frequencies and can achieve atomic resolution (Stranick and Weiss, 1994; Bumm *et al.*, 1996; Moore *et al.*, 2010). The vast array of properties that can now be addressed are illustrated in Table I.

III. ATOMICALLY RESOLVED SURFACE CHEMISTRY

Real-space atomic-resolution imaging of reactions on metal, semiconductor, and oxide surfaces has transformed surface science with implications in areas ranging from device processing to catalysis. The first decades of fundamental studies and development provide the basis on which to address more complex interactions and environments. Here the challenges and advantages of operation of SPM in controlled gas environments are considered; this opens new opportunities in surface chemistry, catalysis, and environmental sciences. Scanning probe microscopies can also be instrumental in overcoming the ''materials'' and ''structures'' gaps in nanoscience. Use of SPM to determine dynamics is considered next. Finally, application of theory to understanding local chemical variations and the interpretation of images is discussed.

A. Bridging the pressure, temperature, and materials gaps with scanning probe microscopy

Several reviews have made a compelling case for the role of SPM in advancing our understanding of reactions at surfaces; see Besenbacher (1996), Street, Xu, and Goodman (1997), Otero, Rosei, and Besenbacher (2006), and Vang *et al.* (2008). An often-debated question in surface chemistry and catalysis is the equilibrium structure of the surface in the presence of gases at pressures relevant to everyday chemistry and the environment. These pressures range from millitorrs to atmospheres. The relevant temperatures for many chemical and environmental phenomena range from roughly a few tens of degrees below to a few hundred degrees above 0 °C. For example, the triple point of water is close to 0 °C, at which point its vapor pressure is 4 torr. Electron-based microscopies and spectroscopies are powerful techniques that provided the bulk of existing fundamental information on and insight into surface processes. However, they normally operate in UHV, far from typical environmental and catalytic conditions. This calls into question the relevance of the information obtained under vacuum, a question embodied in the so-called ''pressure and temperature gap.''

Scanning probe microscopy techniques are not limited to operation under vacuum and have been used extensively in more relevant environments. From its inception in 1992, with the first paper reporting the operation of a scanning STM inside a chemical reaction cell (see Fig. 13) or high-pressure STM (HPSTM) to today, numerous papers and instrumental improvements have demonstrated the relevance and vitality of the field and the unique information on the structures of surfaces and their chemical properties in the presence of reactive gases. Figure 13 illustrates the various surface structures that result from exposure of Pt(110) to atmospheric pressures of H_2, O_2, and CO (McIntyre, Salmeron, and Somorjai, 1993). Under H_2, a classic missing-row reconstruction develops, while O_2 stabilizes the (111) surfaces and results in faceting. CO facilitates step bunching.

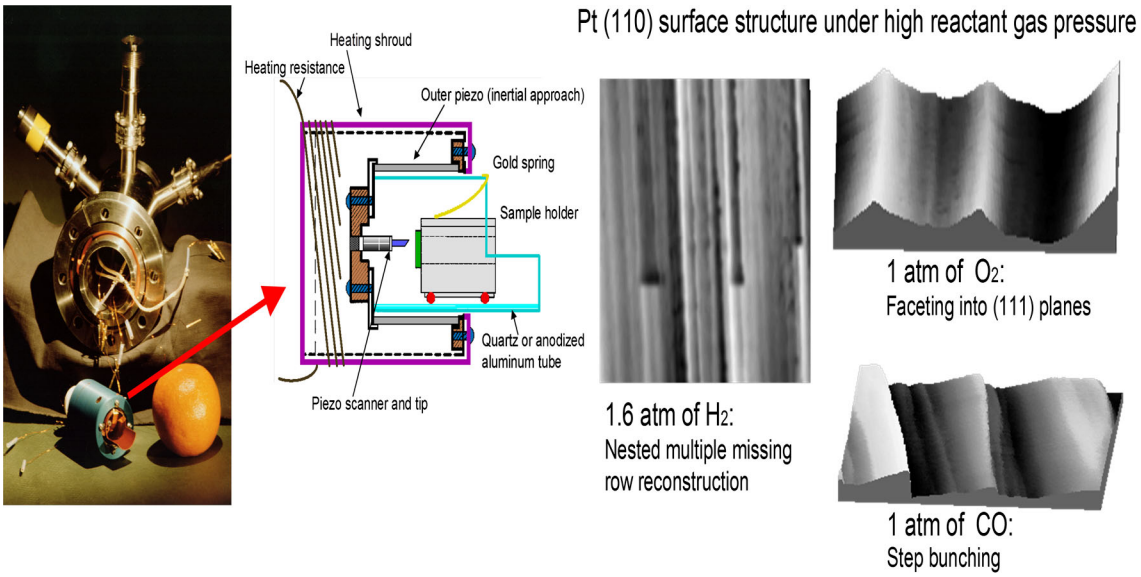

FIG. 13 (color online). Left: Photograph and schematic of a STM scan head inside a reactor cell. From Bonnell, 2000. Right: STM images of Pt(110) surfaces inside the reactor with gas environments of 1.6 atm of H_2 and 1 atm of O_2 and CO. The crystal surface reconstructs into missing rows, facets, and step bunching, respectively. From McIntyre, Salmeron, and Somorjai, 1993.

This approach is being applied to an increasing range of important reactions. Structures formed by NO on Rh(111) (Rider *et al.*, 2001) and by CO on Pt(111) (Longwitz *et al.*, 2004) have been determined at high pressures. Coadsorption of CO and NO in model automobile exhaust catalysts (Rider *et al.*, 2002) and the structure of Pt(110) during catalytic oxidation of CO with O_2 (Hendriksen and Frenken, 2002) have been examined. So have metal clusters supported on oxide surfaces (Goodman, 2003) and the restructuring of stepped Pt catalyst surfaces by high CO coverage (Tao *et al.*, 2010).

These and related results enable the determination of the structures of surfaces in equilibrium with reactant gases, which are otherwise difficult to obtain. Despite the need for the application of HPSTM to studies of surface chemistry and catalysis, only a few groups around the world have actually built HPSTM for atomic-resolution imaging studies under catalytic reaction environments, including the groups of Besenbacher, Goodman, Salmeron, Somorjai, and vom Frenken (Hendriksen *et al.*, 1998; Kolmakov and Goodman, 2000; Laegsgaard *et al.*, 2001).

Difficulties and challenges include (1) the fragile nature of the tip, particularly under reaction conditions where it can undergo undesirable changes in composition; (2) tunneling gap instabilities, caused by the rapid diffusion of atoms and molecules in the tip-surface gap; (3) temperatures above room temperature requiring long equilibration times with the reactor cell; (4) thermal drift; and (5) risk of depolarization of the piezoelectric transducers, if they are located in the same chamber. Some of these problems have been addressed by sturdy and rigid scan heads (Laegsgaard *et al.*, 2001), by separation of the tip and scanner piezoelectric transducer from the reactor chamber (Hendriksen *et al.*, 1998), and by symmetric head designs that correct for the differential expansions of the various elements.

The explosive progress in the synthesis of nanostructured materials holds great promise for providing systems with tailored performance in energy-related and other applications. Surface science investigations typically rely on macroscopic, single-crystal samples with flat surfaces, raising the important question of whether, or to what extent, traditional investigations are applicable to nanostructures. The local nature of scanning probe microscopy makes it an ideal tool to overcome this traditional and newly evolving "materials gap." In terms of instrument development, the integration of a scanning electron microscope (SEM) with a STM enables accurate positioning of the STM probe tip on a specific nanostructure and is now commercially available and yielding fruitful results (Hänel *et al.*, 2006); improved configurations are being pursued (Jaschinsky *et al.*, 2006). For many materials, however, one example being metal oxides, electron-beam-induced artifacts (Dulub *et al.*, 2007) could represent a significant problem with such instruments. Recent STM imaging of nanostructures, e.g., of plasma vapor deposition-grown SnO_2 nanobelts (see Fig. 14) (Katsiev, Kolmakov, Fang, and Diebold, 2008; Katsiev *et al.*, 2008), shows that optimizing sample preparation as well as a choice of substrate is important in such investigations. Figures 14(a) and 14(c) contrast the difference between large single-crystal surfaces and nanostructures, in this case "nanobelts." STM images from an individual nanobelt with increasing spatial resolution are shown in Fig. 14(d), demonstrating the potential to obtain atomic-scale information on complex structures.

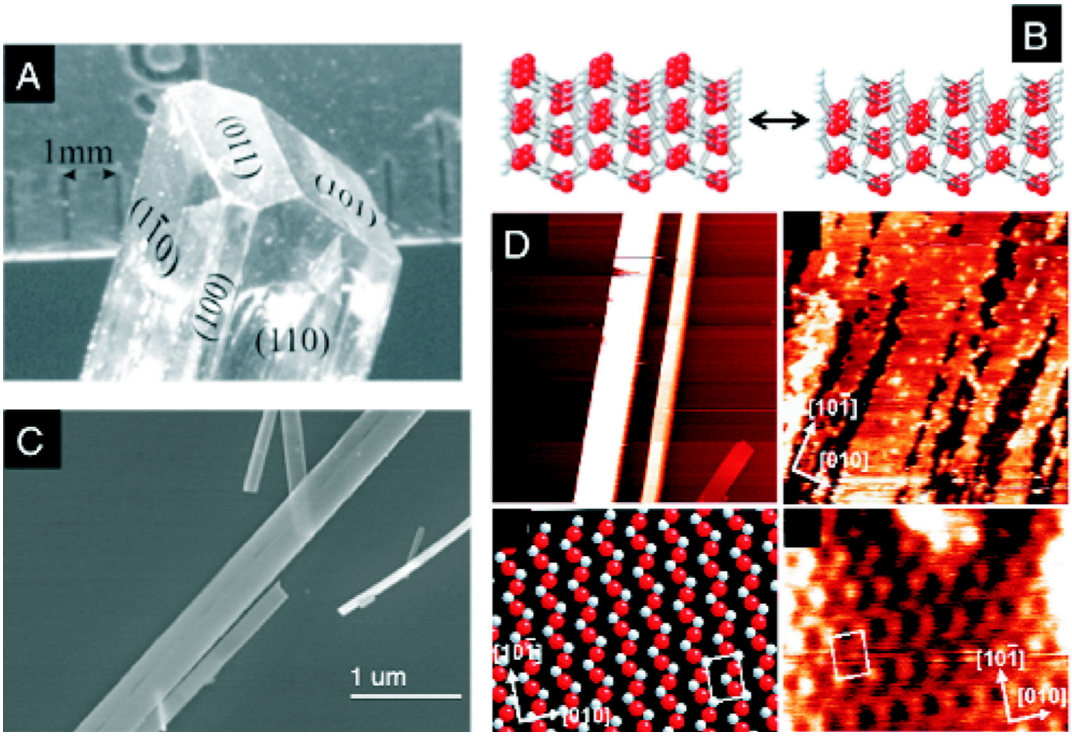

FIG. 14 (color online). (a) Photograph of a SnO_2 single crystal. The (101) surface displayed in (b) is of particular interest because it can be reversibly produced in fully oxidized and reduced form, making this an ideal model system to study processes relevant in chemical sensing. (c) SEM image of SnO_2 "nanobelts." The wide sides of the nanobelts have (101) orientations. (d) STM images of SnO_2 nanobelts with different magnifications. From Batzill *et al.*, 2005.

B. Dynamic processes

A topic of great importance in surface chemistry is the measurement of dynamic properties in surface processes, e.g., diffusion, time-resolved molecular rotation, vibration, and dissociation. The improvement in scanning speeds provided by well-designed heads with high-frequency mechanical resonances enables possible video-rate imaging (Kuipers *et al.*, 1995; Rost *et al.*, 2005). This is useful for studying diffusion processes with dynamics in the range of milliseconds to seconds, which for room temperature implies energy barriers on the order of 1 eV. For lower barriers, even by a small amount, the diffusion rates are much too high. A more efficient approach is to bring the thermally activated ''diffusion'' time to within the scanning rate by reducing the temperature, since the rates are exponentially dependent on temperature. Many measurements of diffusion have been done in this way. Examples include the diffusion of H on Cu (Lauhon and Ho, 2000), water on Pd (Mitsui *et al.*, 2002), and benzene on Au (Mantooth *et al.*, 2007). Subsurface impurities have also been observed and their diffusion measured in this way (Rose *et al.*, 2001). Many dynamical changes, for example, the dynamical proton transfer dynamics in a water overlayer on a metal oxide surface (Dulub, Meyer, and Diebold, 2005), require much higher temporal resolution. For processes in the picosecond and femtosecond ranges, one must resort to pump-probe methods, if the process can be set up to be repetitive. This has been attempted by Weiss *et al.* (1993) and others (Bartolini *et al.*, 2007). In terms of the diagram in Fig. 1, these efforts represent a projection of STM along the temporal axis into the regime of higher functionality.

C. Atomic-scale spectroscopy

In addition to being a tool for imaging surfaces with unprecedented resolution, the STM has many other equally important applications. The atomically sharp tip can be used to move atoms at will, and to interrogate molecules by spectroscopic methods, taking advantage of the fact that the bias voltage selects the electron states in the tip and in the surface that participate in the tunneling process. Atom manipulation, i.e., the ability to move, to desorb, and to dissociate atoms and molecules, was first demonstrated by Eigler and co-workers (Eigler and Schweizer, 1990; Weiss and Eigler, 1992), and was followed by others (Stroscio and Eigler, 1991; Hla *et al.*, 2000a, 2000b). Vibrational and electronic spectroscopy can be performed at the atomic scale with the STM, and it is there that some of its most spectacular results have been obtained. Electronic state spectroscopy mapping was demonstrated by Feenstra *et al.* (1987) to distinguish Ga from As atomic sites in GaAs(110). Ho and co-workers were the first to demonstrate vibrational spectroscopy, studying C_2H_2 adsorbed on Cu(100) (Stipe, Rezaei, and Ho, 1998a) via inelastic tunneling. Figure 15(a) shows an STM image of C_2H_2 on Pt(111) along with calculations of the effect of orbital structure on the STM contrast. The tunneling electrons cause the molecule to rotate in the site, which is indicated in the contrast changes in the series. The inelastic tunneling spectroscopy (IETS) exhibits a peak at 358 meV associated with a C-H stretch, which shifts to 266 meV for deuterated acetylene; see Fig. 15(b). The difference in the manner in which the electrons cause molecular rotation between the two molecules is identified based on the localized inelastic spectroscopy.

Kawai and co-workers (Kim, Komeda, and Kawai, 2002), Pascual (Pascual *et al.*, 2001; Pascual, 2003), and others (Blake *et al.*, 2009) have shown the great promise of vibration spectroscopy applied to chemical properties of adsorbed molecules. A natural extension of the technique is the study of excitation and deexcitation channels of molecules, to determine reaction pathways and coordinates (Hahn and Ho, 2005). For example, one or more quanta of vibration energy imparted to a molecule by tunneling electrons produce a short-lived excited molecular state that decays via anharmonic coupling to other modes, potentially resulting in molecular dissociation, desorption, diffusion, rotation, etc. (see Fig. 15) (Stipe, Rezaei, and Ho, 1998b; Sykes *et al.*, 2006). The possibility of excitation and subsequent reaction of a molecule as a function of site, i.e., on a flat terrace, near a step, or near other atoms or impurities, opens unique opportunities for understanding the roles of some active sites in catalysis. This powerful capability of the STM will expand as better instruments become more widely available.

D. Atomic and molecular manipulation

One of the most striking capabilities of STM is the ability to manipulate atoms and molecules. This was first done to find out what was underneath adsorbed Xe atoms to determine why they were at particular sites (Weiss and Eigler, 1992). It was later used to set up scattering centers and structures to form specific interference patterns (Crommie *et al.*, 1993; Heller *et al.*, 1994; Moon *et al.*, 2008, 2009). Understanding and manipulating these patterns yields a means of tuning and patterning the local density of states (LDOS), to guide dynamics, structures, and chemistry. Likewise, artificial structures can be formed by manipulation and then their electronic interactions can be measured with STM and local spectroscopies, as in the chain of Au atoms constructed by Ho and co-workers (Nilius *et al.*, 2002). Hla, Ho, Rieder, Rosei, Weiss, and others used manipulation to align reactants and intermediates, to induce reaction, and to preclude reaction (Lee and Ho, 1999; Hla *et al.*, 2000; McCarty and Weiss, 2004; Lipton-Duffin *et al.*, 2009). Many of these studies require low-temperature operation, both for the stability of the structures formed and for stability of the STM in moving atoms and molecules without damaging the surface and/or the probe tip.

Lyding and co-workers used the STM to desorb hydrogen-passivated Si surfaces, so as to change the local electronic structure and reactivity (Lyding *et al.*, 1994; Avouris *et al.*, 1996). This patterning and nanolithography at the smallest possible scales enables tests of electronics and electronic interactions at the ultimate limits of miniaturization. It is also possible to manipulate molecules at room temperature and to watch how assemblies reconstruct to move toward more stable structures; this was done for organometallic sandwich compounds under solution (Takami *et al.*, 2010).

A number of other scanning probe lithography techniques have been developed, notably dip-pen nanolithography and nanografting. Dip-pen nanolithography was developed and

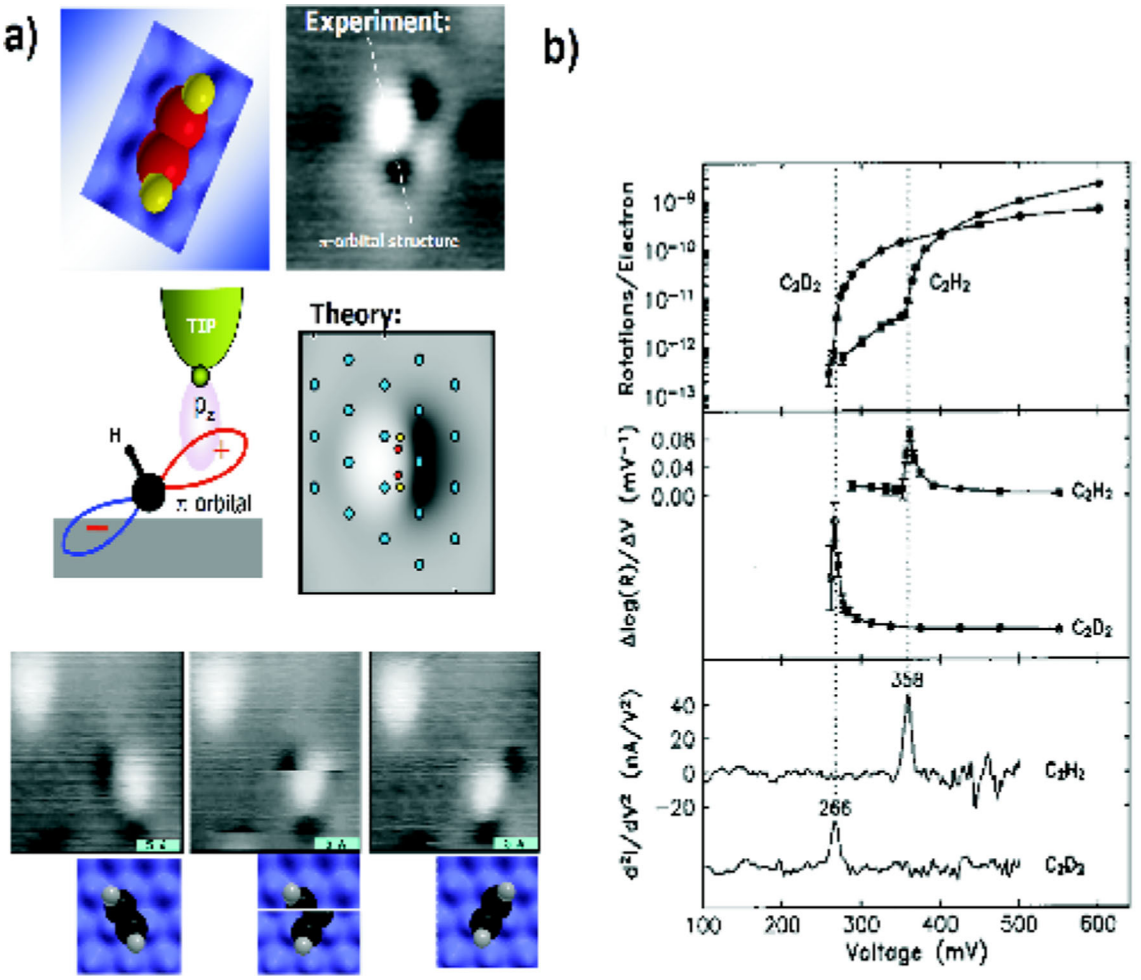

FIG. 15 (color online). (a) Schematic of a C_2H_2 molecule adsorbed on Pd(111) and associated STM image. Shown below them is a calculated image showing the modulation of the tunneling current by the orbital structure of the molecule. Tunneling electrons can cause the molecule to rotate in its three fold hollow site. (b) Inelastic electron tunneling spectra obtained by Stipe, Rezaei, and Ho (1998a) on C_2H_2 molecules on Cu(100). Tunneling probability changes due to excitation of CH stretch vibrational modes are visible.

commercialized by Mirkin and others, and uses ''ink'' molecules placed on atomic force microscope tips to draw structures on surfaces (Piner *et al.*, 1999). In nanografting, developed by Liu and co-workers, sections of monolayers are removed with a scanning probe microscope tip while other molecules come from solution to replace those removed (Xu and Liu, 1997; Liu *et al.*, 2000).

These advances are leading to a broader range of systems that can be manipulated and constructed, as well as the conditions under which this can be done, while maintaining the exquisite precision that was already demonstrated. The capability to assemble precise structures may ultimately lead to the discovery of high-value structures that might be targeted for fabrication by other methods. In the meantime, this rich test bed enables small experimental variations in structures that can subsequently be measured by scanning probe microscopy and spectroscopies to understand the effects of defects, periodicity, and dimensionality on other properties.

E. Coupling theory with experiment

Scanning tunneling microscopy images by themselves are a collection of maxima and minima on a two-dimensional energy-specific electronic map. The topography of this map is not an ''atomic height'' contour. Rather, it reflects the structure of the electronic states responsible for the tunneling, which have the largest contribution from orbitals near the Fermi level of the tip and surface (Eigler *et al.*, 1991; Hofer *et al.*, 2003). When atoms and molecules adsorb on the surface, their identity and the contrast they produce are not easily known. Once a molecule dissociates into various possible product atoms and molecules, identifying these fragments is a challenging task. As indicated, vibrational spectroscopy can in some cases identify the species present, as in IR and Raman spectroscopy.

As noted, one of the key elements of STM for chemistry is the ability to map the filled and empty states (and orbitals) of the surface. This was first demonstrated for GaAs(110) (Feenstra *et al.*, 1987), showing the charge transfer from Ga to As on this stoichiometric surface, and thus the localization of empty states on Ga and of filled states on As. The relevance to chemistry is that atoms, molecules, or parts of molecules favor filled or empty states according to whether they are electrophilic or nucleophilic, respectively (Kamna *et al.*, 1996; Sykes *et al.*, 2003; Barth *et al.*, 2005). In fact, the situation is more complicated in that adsorbates interact

and react with specific energies of filled and empty DOS or orbitals. Thus, the ability to map the energy-resolved LDOS and specifically the local perturbations enables using the STM to "see" the surface as mobile adsorbates would. Potentials felt by adsorbate and interadsorbate potentials have been extracted in selected cases (Repp *et al.*, 2000; Knorr *et al.*, 2002; Kulawik *et al.*, 2005; Sykes *et al.*, 2005; Nanayakkara, 2007), but by indirect means (i.e., postmortem analyses of quenched adsorbate positions or from measured dynamics; *vide infra*). One of the goals of the field is to learn to use theory to transform energy-resolved maps of electronic structure directly into potentials felt by adsorbates.

Theoretical analyses are, or should be, an essential part of many STM imaging experiments [see Fig. 15(a)]. Theoretical developments have been vigorously pursued by Tersoff and Hamann (1983), Chen (1992), Lang (Eigler *et al.*, 1991), Sautet (Sautet and Joachim, 1988; Sautet *et al.*, 1993), Cerdá *et al.* (1997), Foster and Hofer (2006), their co-workers, and others. Today, density functional theory (DFT) methods and programs are available and can be used to provide insight to help in the analysis of STM images and spectra. Density functional theory helps to determine the energetically favored structures of the surface and the tip, and provide projections of the density of states at the Fermi level (that already contain essential elements of the STM image).

The real insight from theory comes from how and why the LDOS varies due to atomic rearrangements, surface and subsurface features, adsorbates, and chemical interactions. The STM images and local spectra are consequences and give important local insight into surface chemistry, structures, and dynamics. Before the invention of scanning probe microscopes, these "chemical views" were missing and ensemble-averaging measurements often led to incorrect conclusions because the important roles of minority surface sites were missed.

Theory is also useful in interpreting images and sequences of images that reveal surface processes, such as diffusion and reaction. The time dependence of nanometer-scale surface features can be obtained without being able to monitor the underlying atomic motion directly (because it is typically too fast). For example, statistical mechanical theories (Bartelt, Einstein, and Williams, 1994) have shown how images of thermal fluctuations of surface steps can be used to determine adatom diffusion coefficients, even when adatoms are not directly observed. Often mass transport on surfaces is mediated by fast-moving vacancies that cannot be imaged. However, much information about the vacancies can be deduced from experimental images as starting configurations in atomic-scale simulations of surface dynamics. If the simulated large-scale surface evolution reproduces the evolution observed in STM "movies" (image sequences), then one has confidence in the atomic model. This approach has been used successfully to interpret STM observations of the thermal coarsening of 2D islands (Icking-Konert, Giesen, and Ibach, 1998), as well as the coarsening of surface domain structures in adsorbed films (Stranick *et al.*, 1994; Schmid, Hwang, and Bartelt, 1998).

F. Metal oxide surfaces: Structure, defects, adsorbates, and functionality

The surface science of metal oxides has progressed considerably during the past two decades. The vast interest in these materials, with energy-related applications ranging from catalysis to solid-state lighting, provides strong motivation for increased efforts to understand the atomic-scale surface and interface properties of metal oxides, as this may ultimately improve materials performance. The electronic and geometric structures of metal oxides are intimately coupled, and local effects such as defects are key to their functioning (Diebold, 2003; Diebold, Li, and Schmid, 2010). Thus, the imaging at the atomic scale of both clean and modified materials, as well as adsorbates and overlayers, is critical for progress in this area (Bonnell and Garra, 2008). In lockstep with STM measurements, the development of theory has been instrumental for recent successes. Density functional theory calculations of large unit cells are now routinely performed and methods for modeling "realistic" environments have been devised (Reuter and Scheffler, 2003).

Surface defects on metal oxides represent reactive sites, because the formation of a defect (e.g., a step edge, an oxygen vacancy, or a subsurface impurity atom) modifies the *local* electronic structure. Atomically resolved STM, as a principal probe of the local electronic structure, is an ideal tool for investigating such effects. Surface oxygen vacancies on metal oxides have been a recent focus in the literature (with the formation of ordered arrays of vacancies recently achieved). The most studied transition-metal oxide surface is $TiO_2(110)$. After several years of debate, there is now consensus on the interpretation of STM contrast on this surface. Figure 16 shows a "ball and stick" model of the (1×1) surface structure and the associated atomic-resolution image. Oxygen vacancies result in defect states, shown in the photoemission spectrum, and as apparent protrusions in the STM image. With this understanding, interactions of the surface with adsorbates can be examined systematically.

Scanning tunneling microscopy has proven its immense capability to unravel adsorption and reaction mechanisms at the atomic scale. Prime examples of this are studies of adsorption of small molecules on $TiO_2(110)$ and ZnO(1010); see Figs. 16 and 17. An adsorbed hydroxyl is evident on the (110) surface of TiO_2 in Fig. 16. Figure 17 (Meyer *et al.*, 2004; Dulub, Meyer, and Diebold, 2005) shows the case of water adsorption on ZnO(1010) for which there are two atomic configurations with similar energies; in one the water is half dissociated, resulting in a (2×1) surface structure, and in the other, the water is intact, resulting in a (1×1) overlayer. Scanning tunneling microscope images reveal the structures of these adsorbate interactions, as well as an intermediate transition structure.

A large number of insightful studies have shown the intricate detail of an apparently simple (but important) reaction such as the dissociation of water on $TiO_2(110)$ (Pang *et al.*, 2008). Considering the wide range of important and interesting oxide materials, the focus thus far has been rather narrow; of the many bulk oxides possible, only a few systems are reasonably well understood (Diebold, 2003; Wöll, 2007; Bonnell and Garra, 2008; Pang *et al.*, 2008).

A major barrier to expansion to other interesting materials is that many of them are too insulating for conventional STM. A band gap of $\sim$3 eV in combination with intrinsic defect doping appears to be a practical limit for atomically resolved

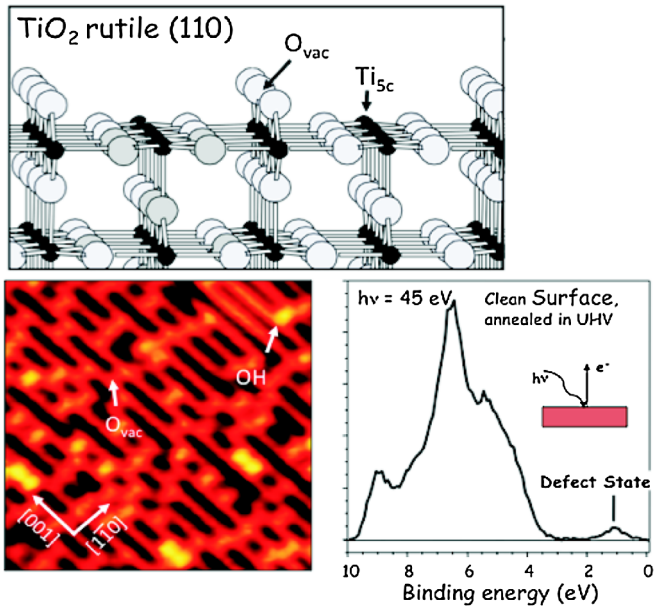

FIG. 16 (color online). The rutile TiO_2(110) surface has become one of the most studied systems in oxide surface science, and STM measurements have been instrumental in understanding this system. Oxygen vacancies (point defects) are easily created through sputtering and annealing. These contribute to a defect state in the band gap, visible in photoemission. In empty-state STM images, oxygen vacancies appear as protrusions between the rows of (protruding) Ti_{5c} atoms; surface hydroxyl (OH) moieties are somewhat more protruding. Adapted from Diebold, Li, and Schmid, 2010.

STM. Certainly the further development of AFM (see Sec. V) will have great impact in this area. So far, several research groups have resorted to the growth of ultrathin films on metal substrates in order to investigate more insulating materials such as Al_2O_3, MgO, or SiO_2 (Freund and Pacchioni, 2008). As these films are only up to a few monolayers thick, they often have interface-dominated structures. Again, STM has been instrumental in resolving the geometric structures of these systems, which have become important models in heterogeneous catalysis (Kresse *et al.*, 2005). Another important current and future application of STM is the resolution of the surface structure and reactivity of the ultrathin oxides that form on top of noble metals such as Rh, Pt, or Pd (Lundgren *et al.*, 2006). There are indications that these two-dimensional surface oxides might be important in the catalytic activity of these materials, a notion that is disputed by others (Gao, Wulfhekel, and Kirschner, 2008). Again, the improved development of high-pressure and high-temperature instruments will help resolve these and many other issues.

G. Quantification through large-scale acquisition and analyses of functional and dynamic atomic-scale imaging

As indicated, SPMs have great power not only in imaging, but also in combination with dynamic and spectroscopic measurements. This was evident from the first measurements of the electronic and vibrational spectra on surfaces, as described above. Typically, scanning probe data are acquired in small numbers; images and spectra are then "interpreted" or compared to calculations. These small data sets make it difficult to acquire quantitative information and to explore systematic variations of molecular and nanostructure function. Further, there is little to indicate whether images and spectra are truly representative of the overall surface.

Now it is becoming possible to record statistically significant data sets, comparable to those obtained for ensemble-averaging macroscopic techniques while still retaining the heterogeneity intrinsic to the single-molecule and

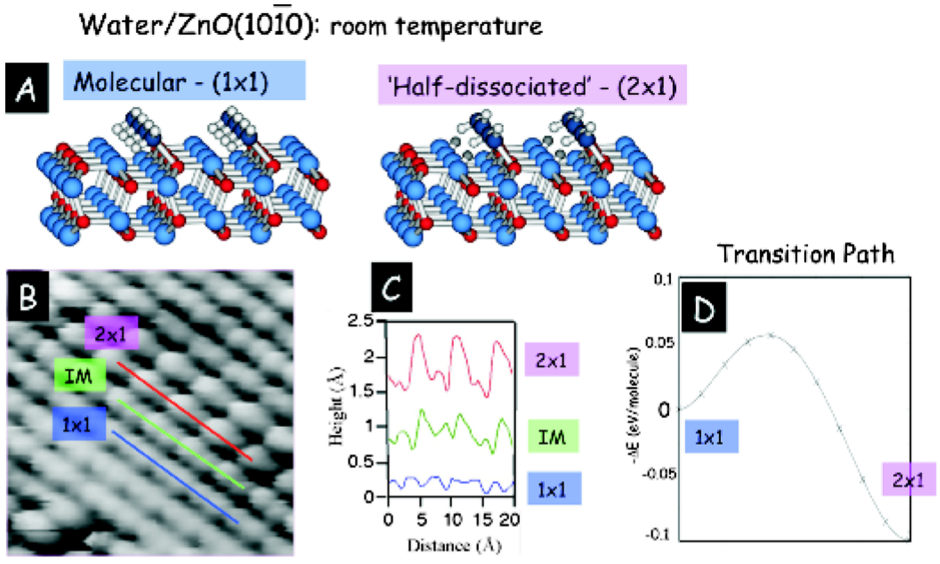

FIG. 17 (color online). Water adsorption on the nonpolar ZnO(1010) surface. In the lowest-energy state, every other molecule is dissociated. Such a configuration results in a saturated overlayer with (2×1) periodicity. A (1×1) overlayer, where every water molecule is still intact, is very close in energy. (a) Atomic models for both structures. (b) The STM image shows rows of water molecules that exhibit either (2×1), (1×1), or an "intermediate" (IM) configuration; (c) line profiles for each of these cases. (d) The estimated transition path between these two structures. Note that the activation energy is rather small (0.05 eV). At room temperature, water switches back and forth between these two states; if the switching occurs more rapidly than the sampling time of the STM measurement, an apparent IM structure is observed. From Dulub, Meyer, and Diebold, 2005.

nanostructure measurements (Donhauser *et al.*, 2001; Mantooth *et al.*, 2007; Weiss, 2008; Claridge *et al.*, 2011). While the stability of low-temperature microscopes makes the acquisition process more straightforward, such extreme conditions are by no means a requirement. Through integrated instrument design, sufficient stability can be reached for a wide range of conditions.

Key to obtaining quantitative, statistically significant single-molecule and nanostructure data are the following (Claridge *et al.*, 2011):

- Stabilizing instruments so that the same structures can be measured repeatedly.
- Developing tools to automate (repeated and systematic) image and spectral acquisition.
- Developing tools to automate image and spectral analyses to extract and to sort key functional, structural, spectral, and dynamic changes, and to associate these with specific local environments, structures, measurement conditions, or other key properties—a set of nanoscopic data-mining tools.
- Coupling of the extracted information to theory (*vide supra*).

Two examples, one chemical and one functional, of the development and application of methods to acquire such data sets illustrate this. The first example, discussed above, involves using ''chemical goggles'' to look at both empty and occupied orbitals with atomic resolution (Feenstra *et al.*, 1987; Weiss and Eigler, 1993; Sykes *et al.*, 2003; Han and Weiss, 2012). One can determine the energies and strengths of the interactions of the (perturbed) substrate electronic structure with the adsorbates. From here, the sites to which adsorbates will go, the structures they form, and their interaction potentials with the substrate and with each other can be elucidated. As noted, a critical step will be going from STM images and spectra directly to interaction potentials experienced by adsorbates. The second example involves repeated measurements to enable analyses and data mining to sort out the relationships of structure, function, environment, and other parameters on key properties. This approach has been taken by Mantooth *et al.* (2007) in determining the intermolecular potentials and likelihood of motion for benzene on Au{111}. This methodology can be applied broadly (and also beyond scanning probe microscopy). One of the keys to the future is recording over a broad dynamic range, from chemical time scales (femtoseconds) to more typical imaging time scales (seconds to minutes) and beyond. There are great advantages that can be exploited in scanning probes in ''focusing'' on the critical species and measurements.

IV. VISUALIZING SPATIAL STRUCTURE IN ELECTRONIC, MAGNETIC, AND BOSONIC PROPERTIES OF MATERIALS

New materials, which may have potential for novel applications, often present new experimental and theoretical challenges. For example, it has become increasingly clear that the exotic properties displayed by correlated electronic materials, such as high-temperature (high-T_c) superconductivity in cuprates, ''colossal'' magnetoresistance in manganites, and properties of heavy-fermion compounds are intimately related to the coexistence of competing nearly degenerate states that simultaneously couple active degrees of freedom: charge, lattice, orbital, and spin states. This competition and frustration often produce states that exhibit inhomogeneity in real space. The striking phenomena associated with these materials is due, in large part, to spatial electronic inhomogeneities, or nanoscale phase separation. In many of these hard materials, the functionality is a result of the *soft* electronic component that leads to self-organization. Birgeneau and Kastner (2000) wrote in the introduction to the special issue of *Science* dedicated to correlated electron systems: ''A remarkable variety of new materials have been discovered that cannot be understood at all with traditional ideas.''

Correlated electron materials and especially transition-metal oxides show great promise for new device applications in the semiconductor industry to go beyond complementary metal oxide semiconductor (CMOS) devices for future information processing technologies, which could be based on ''state'' variables such as spin. As stated in the 2007 International Technology Roadmap for Semiconductors (http://www.itrs.net/Links/2007ITRS/Home2007.htm), chapters on Emerging Research Devices and Emerging Research Materials, highly correlated electron systems exhibit coupling between orbital hybridization, charge, and spin that may enable new devices. ''The challenge is to determine whether these properties can be used to enable new devices at the nanometer scale.'' Applications of these materials must take into account their environments of broken symmetry and reduced dimensionality. Another important class of materials potentially important for applications is the recently discovered 3D topological insulators (Zhang *et al.*, 2009). The surface states of these materials exhibit unique properties such as Dirac dispersion, a protected Dirac node in the absence of broken time-reversal symmetry, and chiral spin texture, which could find use in spintronics and quantum computation.

Advanced experimental probes revealing the variation of diverse physical observables in real space have played a preeminent role in the studies of complex materials where it has been possible to directly visualize dramatic variations of electronic and magnetic properties at the nanoscale. In particular, the ability of the STM to measure and to map the LDOS, with atomic resolution has yielded important information that could not have been observed by any other techniques. Several important examples are highlighted in Sec. III. While the basic STM technique entails measurements of differential conductance as a function of energy and position $[dI/dV(\boldsymbol{r}, E)]$, STM has proved to be a far more versatile instrument than originally envisioned. With vastly improved stability and high energy and spatial resolution, one finds the instrument capable of momentum-resolved (k-resolved) density of states measurements with Fourier transform scanning tunneling spectroscopy (FT-STS), magnetic information using spin-polarized STM (SP-STM), and bosonic mode (phonons or spin excitations) information by inelastic tunneling spectroscopy. This array of capabilities can be made even more powerful by one of the most exciting recent developments: the ability to perform STM measurements while simultaneously varying the position of the relative Fermi energy with respect to the bulk bands using back gating. Back-gating STM, which has been enormously

successful in graphene (Zhang *et al.*, 2008; Jung *et al.*, 2011), is likely to be more widely used for other materials in the future.

A. Spectroscopic-imaging scanning tunneling microscopy for electronic wave functions in complex electronic materials

In SI-STM studies $dI/dV(\mathbf{r}, E)$ is imaged with subatomic spatial resolution and submillivolt energy resolution. The most immediate utility of spatially resolved $dI/dV(\mathbf{r}, E)$ measurements is the ability to map out the variations in electronic properties at various energy and length scales. This has been used, for example, to measure the nanoscale variations in the superconducting gap of high-T_c superconductors, visualize vortex lattices, or to map out the inhomogeneous electronic states of graphene. But $dI/dV(\mathbf{r}, E)$ maps also encode momentum space (k-space) information which makes STM a powerful and unique probe of the electronic properties in both real and momentum space. When elastic scattering mixes momentum eigenstates $\mathbf{k}_1$ and $\mathbf{k}_2$, an interference pattern with wave vector $\mathbf{q} = \mathbf{k}_2 - \mathbf{k}_1$ manifests as real-space modulations with wavelength, $\lambda = 2\pi/|\mathbf{q}|$. This interference is observable as modulations in $dI/dV(\mathbf{r}, E)$ which are essentially a measure of the local density of states [LDOS($\mathbf{r}$, E)]. By analyzing the Fourier transform of the real-space LDOS($\mathbf{r}$, E) images, certain constant energy contours in k space can be reconstructed. The technique of obtaining k-space information from STM data was first used to relate Fourier transforms of Friedel oscillations in STM images to band structure (Hofmann *et al.*, 1997). A highly developed version of this technique, FT-STS [a technique using the Fourier transform of STM dI/dV maps (spectroscopic maps) to obtain q-space information], is now being used to yield real-space and k-space electronic structure simultaneously as a function of energy. Fourier-transform STS requires the ability to obtain large-area spectroscopic maps with very low drift and a high signal-to-noise ratio in the spectroscopy. It is important to remember that FT-STS provides q-space information and that going from q space to k space may require additional information from other k-space probes. Furthermore, only a selection of all possible $\mathbf{q}$ vectors is visible in STM. Nevertheless, FT-STS has had remarkable success in providing new k-space information augmenting traditional real-space data. As an example, FT-STS measurements of high-T_c superconductors in the superconducting state (Hoffman *et al.*, 2002) allow simultaneous measurements of the location of the Fermi surface arc and the spatially averaged DOS(E) in cuprates. Figure 18(a) shows the Fourier transform of the LDOS and a small region in k space that exhibits that behavior [see Fig. 18(b)]. In other regions of k space the states are localized in real space [see Fig. 18(c)]. These capabilities have been used to demonstrate that cuprate Bogoliubov quasiparticles (broken Cooper pairs) occupy only a restricted region of k space that shrinks rapidly with diminishing hole density as shown in Fig. 18(b) (Kohsaka *et al.*, 2008). Temperature-dependent studies of the interference patterns in cuprates revealed stripelike correlations in the pseudogap state, which Parker *et al.* (2010) showed are a result of the presence of the pseudogap state.

Another system where FT-STS has been extraordinarily successful is in studies of the surface states of topological insulators. Because of the chiral nature of the surface states in these materials, backscattering into opposite momentum space states is theoretically forbidden. Fourier-transform STS studies of $Bi_{1-x}Sb_x$ (Roushan *et al.*, 2009) and Bi_2Te_3 (Zhang *et al.*, 2009) have been critical in demonstrating many aspects of the topological insulators, including the absence of backscattering in time-reversal invariant systems and the restoration of backscattering in systems with broken time-reversal symmetry (Okada *et al.*, 2011). Figure 19 shows the interference patterns observed in a topological insulator that are consistent with the absence of backscattering, which is the hallmark of topological states, and the observation of new backscattering channels in samples doped with magnetic impurities.

B. Spin-polarized scanning tunneling microscopy

Besides the important role they play as storage devices in modern information technology, magnetic materials are key components of novel concepts such as spintronics and spin-based quantum computing. Since the application of these concepts requires a detailed understanding of dependencies and interactions between magnetic nanostructures down to the atomic level, high-resolution microscopy techniques with

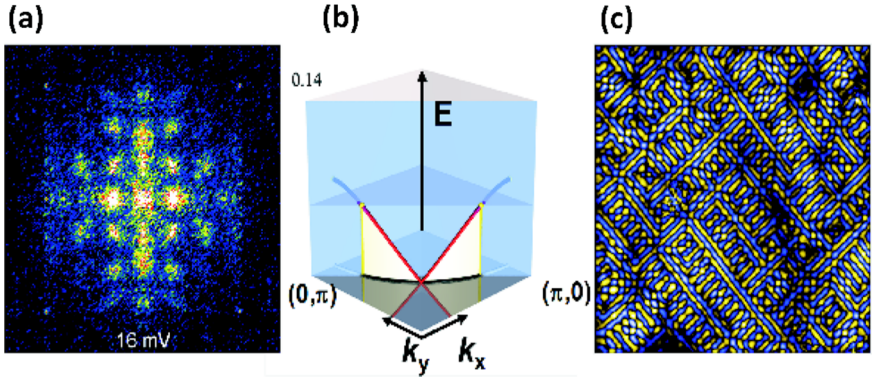

FIG. 18 (color online). Fourier transform of cuprate LDOS modulations exhibiting signature Bogoliubov excitations from d-wave Cooper pairs. (a) These excitations are detected only in k space in the region shaded white in (b). Beyond the k-space line connecting p, 0 to 0, p, the states are not the excitations of d-wave Cooper pairs but localized in r space as in (c). From Kohsaka *et al.*, 2008.

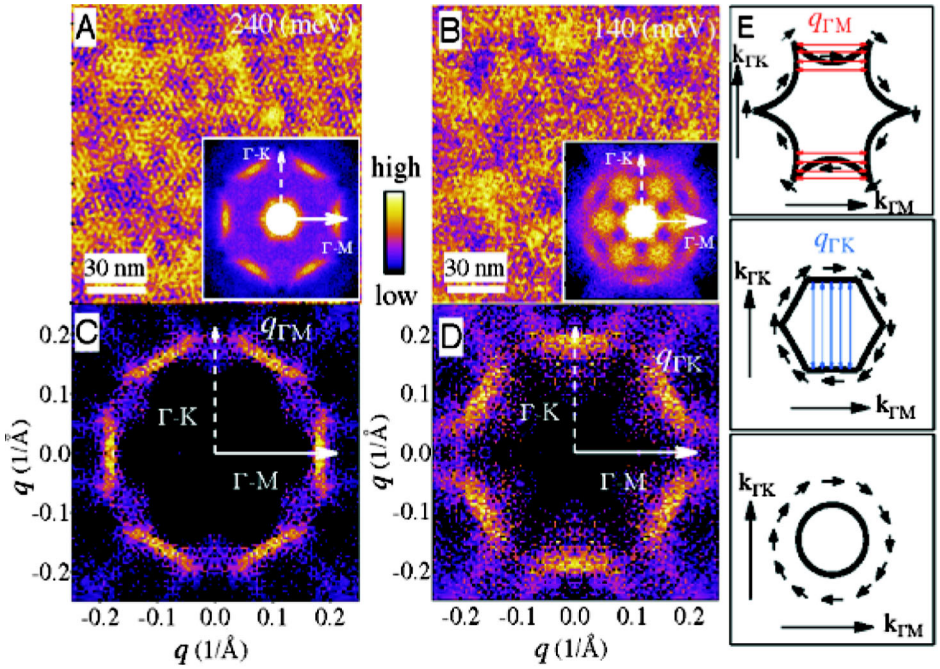

FIG. 19 (color online). Scanning tunneling microscopy data on Fe-doped topological Bi_2Te_3 (a), (b) $dI/dV(r, E)$ maps showing interference patterns, with the inset showing the corresponding Fourier transform. (c), (d) Same data as insets in (a), (b) but divided by the Fourier transform at +60 meV to remove nondispersing features at small **q** vectors. The **q** vector along LK was not reported in previous samples without time-reversal symmetry breaking impurities. (e) Schematic diagram of constant energy contours showing the nested regions that result in the primary q vectors observed in STM at low energies along LK and higher energies along LM. From Okada *et al.*, 2011.

magnetic or even single-spin sensitivity are in high demand. In fact, soon after the invention of scanning tunneling microscopy in 1982 (Binnig and Rohrer, 1982), Pierce proposed measuring the local sample magnetization by making the tip sensitive to the spin of the tunneling electron (Pierce, 1988), a technique we call spin-polarized scanning tunneling microscopy today. Several concepts for achieving spin sensitivity were discussed, among them the use of superconducting tips in strong magnetic fields (Meservey and Tedrow, 1994), GaAs tips excited by helically polarized light (Alvarado and Renaud, 1992), and magnetic tip materials (Johnson and Clarke, 1990). While the former two use external stimuli to generate a spin imbalance at the Fermi level E_F, the latter relies on the spontaneous polarization of magnetic materials. Because the spin of the tunneling electron, to a first approximation, has to be conserved as it crosses the tunneling barrier, both the tunneling current and the junction conductance depend on the relative magnetization direction of tip and sample.

While attempts to achieve magnetic sensitivity with superconducting or GaAs tips had only limited success, several major breakthroughs were made with magnetic tips (Wiesendanger *et al.*, 1990; Bode, Getzlaff, and Wiesendanger, 1998; Wulfhekel and Kirschner, 1999; Wiesendanger, 2011). One key ingredient was the use of a test sample with a suitable magnetic domain structure; an example is the Cr(001) surface. Bulk Cr is an antiferromagnet with alternating (001) planes being magnetized in opposite directions, i.e., on Cr(001) the magnetization ought to reverse whenever a monatomic step edge is crossed. The simple surface topography of Cr(001) enables the detection of spin-dependent contributions to the signal even in constant-current STM images (Wiesendanger *et al.*, 1990). The schematic principle is shown in Fig. 20(a). If the spin-dependent DOS of tip and sample are parallel (antiparallel), symbolized by arrows, E_F is governed by electrons of the same (a different) spin character, i.e., a high DOS of occupied

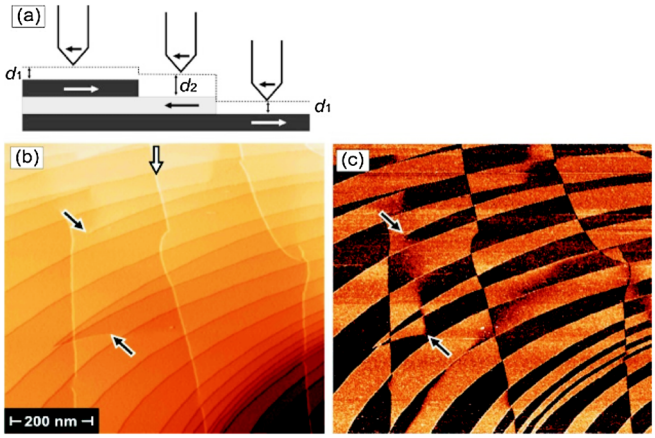

FIG. 20 (color online). (a) Schematic representation of spin-polarized STM. Spin-polarized tunneling results in a tip-sample distance that depends on the relative magnetization direction of tip and sample. (b) Topography and (c) magnetic dI/dU map of a Cr (001) surface measured with an Fe-coated probe tip at 300 K. Screw (arrows) and edge dislocations (one example marked by an arrow) can be recognized in (a). The tunneling parameters are $I = 3$ nA and $U = -0.7$ V. As for other monatomic step edges the edge dislocations lead to a change of the magnetic contrast due to the layered antiferromagnetic structure of Cr(001). Typically, a domain wall is found between two screw dislocations, e.g., between the two arrows in (b). From Bode *et al.*, 2007.

majority states in one electrode is matched (not matched) by a high DOS of empty majority states in the other. For a STM operated in constant-current mode, where feedback adjusts the vertical position of the tip to keep the current constant, this results in a magnetization-direction-dependent tip-sample separation (d_1 vs d_2) which translates into different apparent step heights. In fact, when using magnetic CrO_2 tips alternating step heights have been observed (Wiesendanger *et al.*, 1990).

Although constant-current mode is suitable for imaging the spin structure of sufficiently flat surfaces, complications arise if large areas or relatively rough surfaces are scanned because the topographic and magnetic contributions cannot be sufficiently separated. This limitation can be overcome by recording the differential conductance (dI/dV signal) simultaneously with the topographic image. In many cases, this yields clear separation of the two signals. After this approach was first demonstrated on Gd (Bode, Getzlaff, and Wiesendanger, 1998), it was successfully applied to several surfaces and thin films (Wulfhekel and Kirschner, 1999; Pietzsch *et al.*, 2000; Wachowiak *et al.*, 2002; Yang *et al.*, 2002; Bergmann, Bode, and Wiesendanger, 2004; Kubetzka *et al.*, 2005; Gao *et al.*, 2008). Figures 20(b) and 20(c) show the simultaneously recorded topography and magnetic dI/dV signal on Cr(001), which reveal the close correlation between the surface structure containing numerous dislocations and the magnetic domain structure (Ravlic *et al.*, 2003).

Spin-polarized STM is particularly important for imaging antiferromagnetic nanoparticles and thin films in which magnetic dipoles are aligned in an antiparallel manner. Because the total magnetic moments virtually cancel, imaging techniques that rely on a net magnetic moment but average over distances larger than the atomic lattice constant do not exhibit any magnetic contrast. Figure 21(a) shows the constant-current image of a Mn monolayer island grown on W(110). While the topography is featureless if measured with a nonmagnetic tip, stripes along the [001] direction can be recognized in Fig. 21(a). The zoomed image shown in Fig. 21(b) reveals that this stripe pattern is not homogeneous but exhibits periodic modulations also visible in the averaged line section of Fig. 21(c). Density functional theory calculations reveal that the underlying spin structure is an antiferromagnetic cycloidal spin antiferromagnetic spiral (Bode *et al.*, 2007) driven by a spin-orbit-induced chiral exchange term, the so-called Dzyaloshinskii-Moriya interaction.

The state of the art of SP-STM enables the investigation of magnetic nanostructures with unprecedented high spatial (Yayon *et al.*, 2007) and energy resolution. Imaging ferromagnetic, antiferromagnetic, and even more complex static spin structures on surfaces of conducting samples is routinely achieved down to the atomic scale. The use of modulation techniques (Bode, 2003; Schlickum, Wulfhekel, and Kirschner, 2003) enables the separation of topographic structure and magnetic contributions to the signal. Tips made of antiferromagnetic materials avoid the artifact where sample domain structure is unintentionally modified by the tip stray field (Kubetzka *et al.*, 2002). The hysteretic response of magnetic nanostructures (Pietzsch *et al.*, 2001) and even single atoms (Meier *et al.*, 2008) on external fields can be studied.

In contrast, the time resolution of SP-STM is rather limited. Superparamagnetic (Bode *et al.*, 2004) and current-induced switching events (Krause *et al.*, 2007) were studied up to frequencies of several hertz, but systematic investigations of dynamic magnetic properties, of fluctuations around the Curie temperature, and of behavior of quantum systems close to the quantum critical point require much higher temporal resolution. Recently, the Loth *et al.* (2010) developed a voltage "pump-probe" technique that, combined with spin-sensitive STM contrast, can measure spin relaxation times of individual atoms with nanosecond time resolution. They placed Fe atoms on a Cu_2N overlayer on Cu(100), a structure that exhibits significant magnetocrystalline

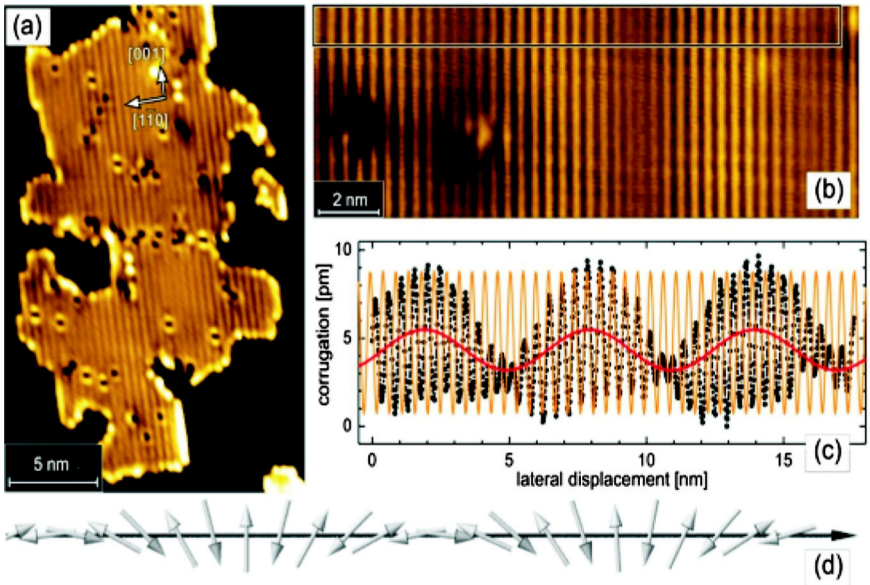

FIG. 21 (color online). (a) Topography of Mn islands on W(110) measured with an Fe-coated tip. Lines along the [001] direction indicate row-wise antiferromagnetic order. (b) A higher-magnification image reveals that the corrugation is not constant but modulated. (c) Averaged line section (dots) taken along the box in (b). (d) Schematic representation of the antiferromagnetic cycloidal spin spiral. From Bode *et al.*, 2007.

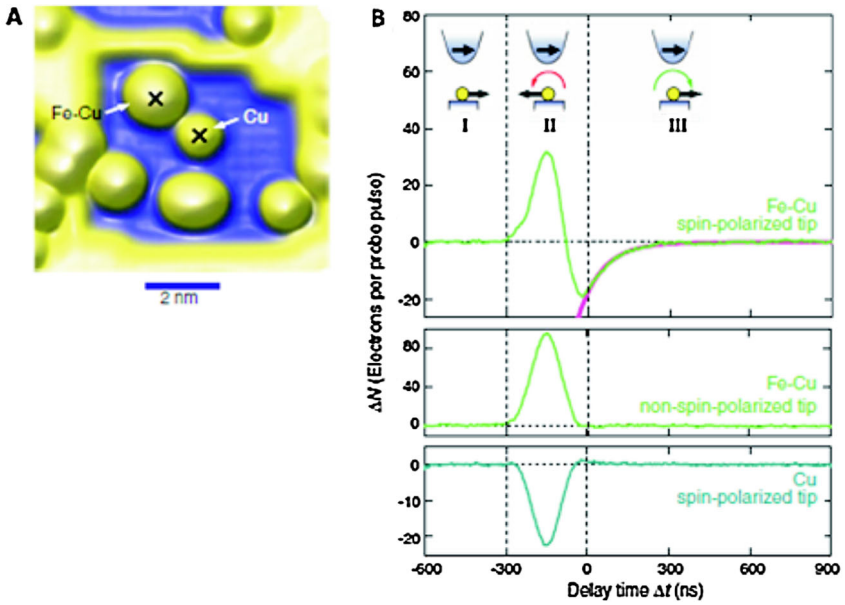

FIG. 22 (color online). Measurement of spin relaxation time. (a) STM topographic image of a Fe-Cu heterodimer and a Cu adatom. (b) Voltage pump-probe measurements of the dimer and two control structures: the dimer probed with a non-spin-polarized tip; a nonmagnetic atom probed with a spin-polarized tip. In region I, the probe precedes the pump; in region II, the pump and probe overlap; in region III, the probe follows the pump and any postexcitation is detected. The Fe-Cu dimer exhibits a relaxation time of 87 ± 1 ns. From Loth *et al.*, 2010.

anisotropy. Large magnetic anisotropy is associated with long spin relaxation times that are necessary for any application. They further increased the anisotropy by placing the Fe atom adjacent to a Cu atom, forming a heterodimer; see Fig. 22(a). Figure 22(b) compares the pump-probe measurements for the Cu-Fe dimer with a spin-polarized tip, with a non-spin-polarized tip, and of an isolated Cu atom with a spin-polarized tip. The process can be considered in three regions: in I, the probe pulse precedes the pump pulse and nothing is detected; in II, the pump and probe pulses overlap and a signal is detected; in III, the probe pulse follows the pump pulse and the postexcitation dynamics are detected. In region II, the spin orientation of the Fe is reoriented; in region III, the time for relaxation back to the original state is detected. In this case, in the Fe-Cu dimer the time is 87 ± 1 ns. The absence of any relaxation signal in the other two cases in which none is expected demonstrates that the postexcitation is due to the spin. This is an exciting advance since it could be generalized to probe conformational changes in molecules, the evolution of excited states as well as relaxation times, and even the precession of spin. The requirements are that the excitation must be driven by spins, the tunnel junction conductance must exhibit a postexcitation time dependence, and the processes must occur at accessible time scales.

C. Inelastic tunneling spectroscopy

In addition to providing electronic density of states information, STM can also provide information on low-energy bosonic modes (spin, phonon, or local vibrational excitations). The coupling between electrons and bosons leads to a renormalization of the density of states, which is possible to observe in the dI/dV spectra for sharp modes or modes where the electron-boson coupling is strong. There is, however, another effect that provides a clearer signal of inelastic tunneling processes. Inelastic tunneling occurs when the tunneling electron excites a boson before occupying its final state. Since energy is either gained or lost in this process, it can happen only when the tunneling electron has energy greater than that of the bosonic excitation, creating a steplike feature in the LDOS at the energy of the bosonic mode, which can be observed symmetrically across the Fermi energy in the dI/dV spectra. Such features were first observed in STM spectroscopy of vibrationally active molecules on the surface (Stipe, Rezaei, and Ho, 1998a), as described in Sec. III.C. The technique of IETS has, however, recently been extended to the study of phonons in graphene, spin excitations in magnetic atoms and clusters, and phonons and spin modes in high-T_c superconductors. As an example, Figs. 23(a) and 23(b) show large-scale and atomic-resolution STM images of a graphene flake on a SiO_2 surface (Zhang *et al.*, 2008). The spectra exhibit a symmetric gaplike feature rather than the linear density of states expected for elastic tunneling; see Fig. 23(c). By gating the sample, they showed that the gap is due to an inelastic interaction associated with a mode pinned in energy, thereby demonstrating that it is a phonon mode. Using IETS, Hirjibehedin *et al.* (2006) probed the interactions between spins in individual atomic-scale magnetic structures and showed that they could observe changes in spin orientation as well as magnitude. The conductance spectra in Fig. 23(d) compare the behavior of a single Mn atom with that of a Mn trimer as a function of magnetic fields applied in the plane of the sample. The dip centered at 0 V results from spin-flip excitations such as those shown in Fig. 22 and the magnetic-field dependence provides insight into the spin coupling. Other examples were summarized by Wiesendanger (2009).

In high-T_c materials, inelastic spectroscopy yielded information that is critical to understanding pairing mechanisms.

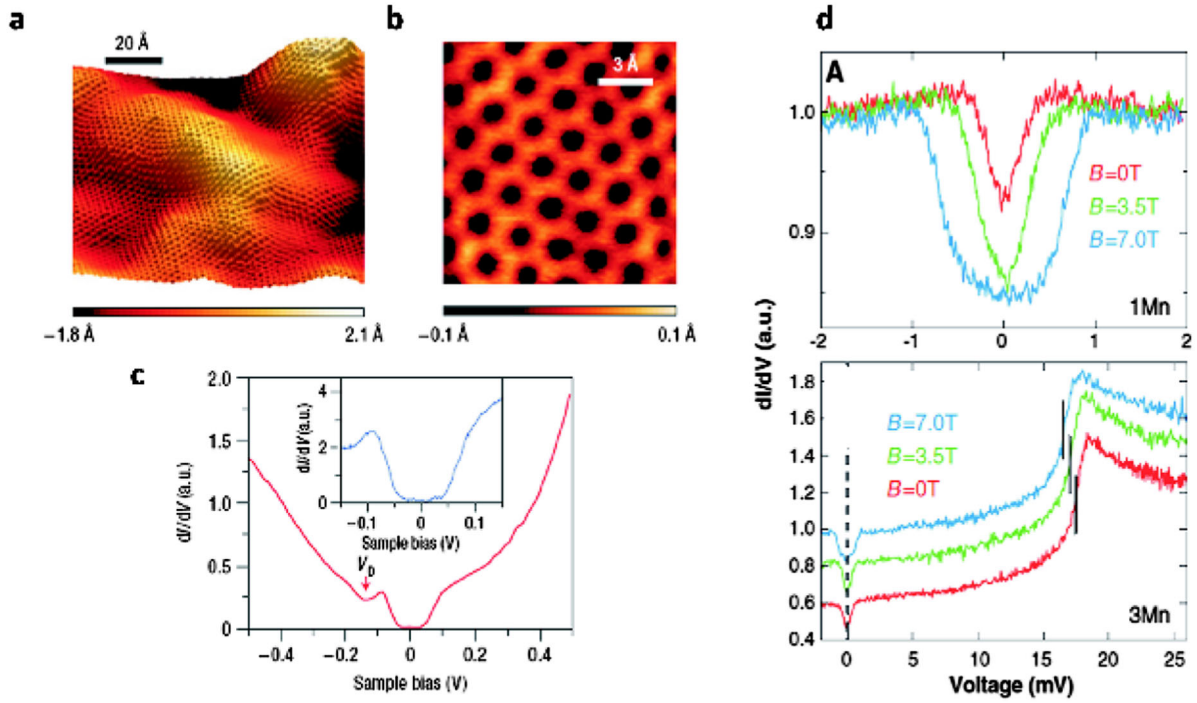

FIG. 23 (color online). (a) Phonon-mediated tunneling in graphene. From Zhang *et al.*, 2008. (b) Magnetic-field dependence of spin excitations in a single magnetic Mn atom and a cluster of three atoms. (c) The density of states showing the gap state in the inset. (d) Temperature dependence of conductance spectra for a single Mn atom and a Mn trimer. From Hirjibehedin, Lutz, and Heinrich, 2006.

In hole-doped high-T_c materials a classic isotope shift in the electron-boson interactions of the cuprate superconductors (Lee *et al.*, 2006), and its subsequent confirmation using angle-resolved photoemission spectroscopy, has made it clear that electron-lattice interactions strongly impact the electronic structure. In contrast, electron-doped superconductors show strong signatures of coupling to the ubiquitous (π, π) spin-resonance mode observed by neutron scattering (Niestemski *et al.*, 2007). Figure 24 shows STM evidence for strong electron-phonon and electron-spin coupling. Lee *et al.* (2006) used oxygen isotopes to label in-plane and out-of-plane oxygen vibration modes. Then, from conductance maps similar to those in Figs. 18 and 19, the second-derivate maps, which highlight inelastic transitions, were used to quantify the relation between mode energy and energy gap in histograms; see Fig. 24(b). The shift in mode energy with the isotope, shown in Fig. 24(a), was the same for empty states as for filled states, which is expected for electron-boson interactions in strong-coupling superconductivity (Lee *et al.*, 2006). This is a tremendously exciting new avenue for exploration of the pnictide high-temperature superconductors. It is highly likely that these lower-temperature systems form Cooper pairs by some form of electron-boson interaction, and IETS is advancing our understanding of these interactions.

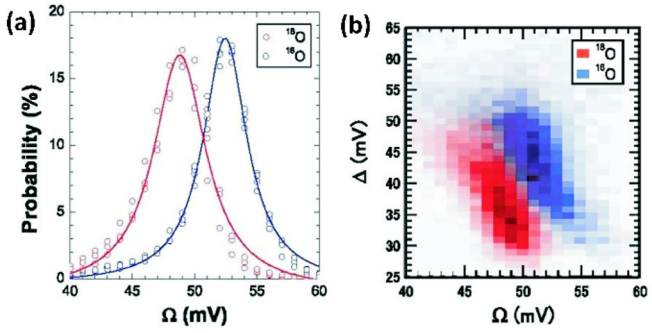

FIG. 24 (color online). Distribution of mode energies detected by d^2I/dV^2 imaging of Bi-2212 crystals containing only ^{16}O and ^{18}O. (a) 2D histograms of mode energies plotted vs the associated energy gap values D for Bi-2212 crystals containing ^{16}O and ^{18}O. (b) The mode detected here as part of the superconducting electronic structure involves vibrations of the oxygen atoms. Distribution of mode energies detected by d^2I/dV^2 imaging. From Lee *et al.*, 2006.

V. PROBING FORCES AND ENERGIES WITH ATOMIC RESOLUTION

Since its invention in 1986 (Binnig, Quate, and Gerber, 1986), the success of AFM is derived from its combination of high-resolution imaging capabilities and broad versatility, as it is capable of imaging almost any type of surface without the need for lengthy sample preparation. This is because force microscopy relies on the detection of interaction forces between a probe tip and a surface rather than a tunneling current. In the most common mode of operation, used in the original instrument, a sharp tip mounted on a leaf spring (cantilever) senses the repulsive forces as it is pressed against a surface. The applied force is usually very low (1–100 nN), so that if operated correctly, no damage occurs to the sample during AFM imaging. Excellent instruments employing this basic imaging mode can be purchased from a number of manufacturers. Treatments of basic principles and monographs summarizing particular aspects of the field can be found by Morita, Wiesendanger, and Meyer (2002), Morita (2005), and Garcia (2010).

Atomic-resolution imaging, however, requires atomically sharp tips. Since the intimate contact between tip and surface in the repulsive regime blunts probe tips and yields tip-sample contact areas typically comprising hundreds or even thousands of atoms, no sustained atomic resolution is possible in this ''standard'' mode. Instead, AFM operation in the noncontact regime is required, as realized in nc-AFM. To avoid tip-sample contact, the cantilever is oscillated by mechanically driving the cantilever base at its resonance frequency f, while the cantilever oscillation amplitude is kept constant. If the tip is located so close to the surface that it senses attractive surface forces, its actual resonance frequency f differs from the eigenfrequency of the undisturbed cantilever f_0. Noncontact AFM uses this frequency shift $\Delta f = f - f_0$ for distance control rather than relying on a tunneling current (Albrecht *et al.*, 1991; Giessibl, 1995, 2003), which is why it can be applied to conducting (Orisaka *et al.*, 1999; Loppacher *et al.*, 2000; Caciuc *et al.*, 2008), semiconducting (Kitamura and Iwatsuki, 1995; Sugawara *et al.*, 1995; Ueyama *et al.*, 1995; Schwarz *et al.*, 2000), and insulating materials (Bammerlin *et al.*, 1997; Allers *et al.*, 1999; Barth and Reichling, 2001; Hoffmann *et al.*, 2003; Schirmeisen, Weiner, and Fuchs, 2006) while still achieving atomic resolution.

From the above descriptions, it is evident that nc-AFM images represent planes of constant Δf rather than force maps. For comparison with theory as well as for intuitive interpretation of AFM data in terms of local binding strengths, etc., the availability of quantitative force and/or energy data would be desirable. Because of the nonlinear nature of the tip-sample interaction, mathematical procedures to recover forces and energies require knowledge of Δf for all tip-sample separations (z) back to a distance where the cantilever oscillates unaffected by the sample's surface forces (Dürig, 1999; Hölscher *et al.*, 1999; Sader and Jarvis, 2004). The acquisition of such $\Delta f(z)$ curves has been successfully employed to measure the site-specific distance dependence of the interaction force between AFM tips and surfaces (''force-distance curves'') (Lantz *et al.*, 2001; Hoffmann *et al.*, 2004; Abe *et al.*, 2005; Hembacher *et al.*, 2005; Sugimoto *et al.*, 2007a). A particularly impressive demonstration of the benefits of this capability was produced recently, where it was used to identify the different chemical species in an alloy of Si, Sn, and Pb (see Fig. 25) (Sugimoto *et al.*, 2007a).

In order to achieve quantitative imaging and characterization of local short-range forces and to determine chemical functionality, it is important to expand these capabilities further by systematically acquiring Δf for dense arrays of x, y, and z values. Based on these data, the 3D atomic force fields just beyond the sample surface can be determined. Despite being experimentally challenging due to the large number of sampling points that make long-term drift and tip stability an issue (Albers *et al.*, 2009a), 3D atomic force fields have been successfully recorded by combining large numbers of force-distance curves (Hölscher *et al.*, 2002; Ashino *et al.*, 2008; Gross *et al.*, 2009), topographical images where the Δf set point had been progressively reduced (Albers *et al.*, 2009a), and a combination of these modes where a slow Δf feedback has been combined with a fast z oscillation (Fukuma *et al.*, 2010). The interest in these 3D force-field techniques stems from their ability to deliver not only exact quantitative values for the surface-normal force field acting between tip and sample, but also a wealth of additional information such as lateral force fields, potential energy barriers, tunneling currents, and energy dissipated during

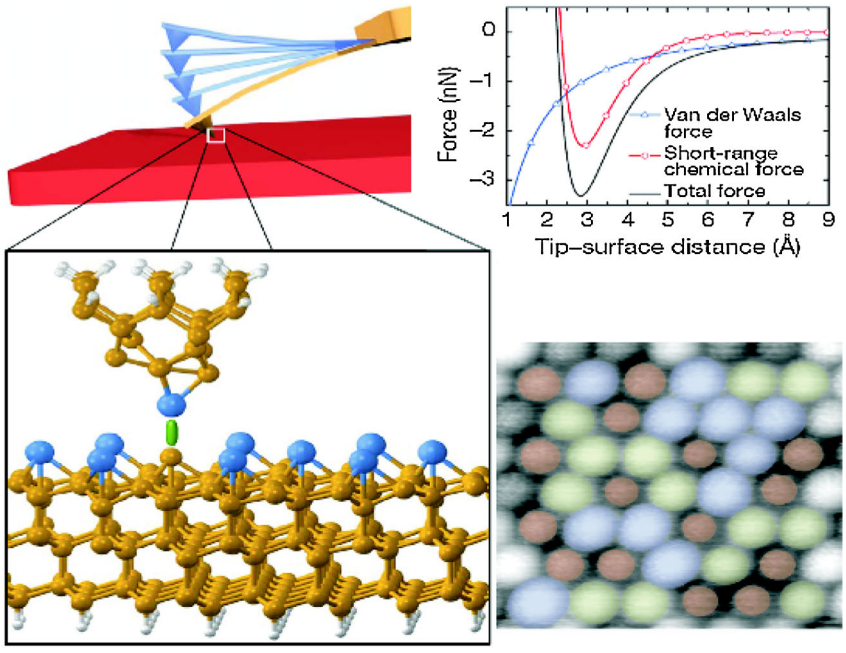

FIG. 25 (color online). Single-atom chemical identification by nc-AFM. The schematic illustrates the operation mode, with the tip oscillating at its resonance frequency, modified by interaction forces with the substrate atoms. The image at the bottom right is the atom-resolved topography of a surface alloy composed of Si, Sn, and Pb atoms blended in equal proportions on a Si(111) substrate. From Sugimoto *et al.*, 2007b.

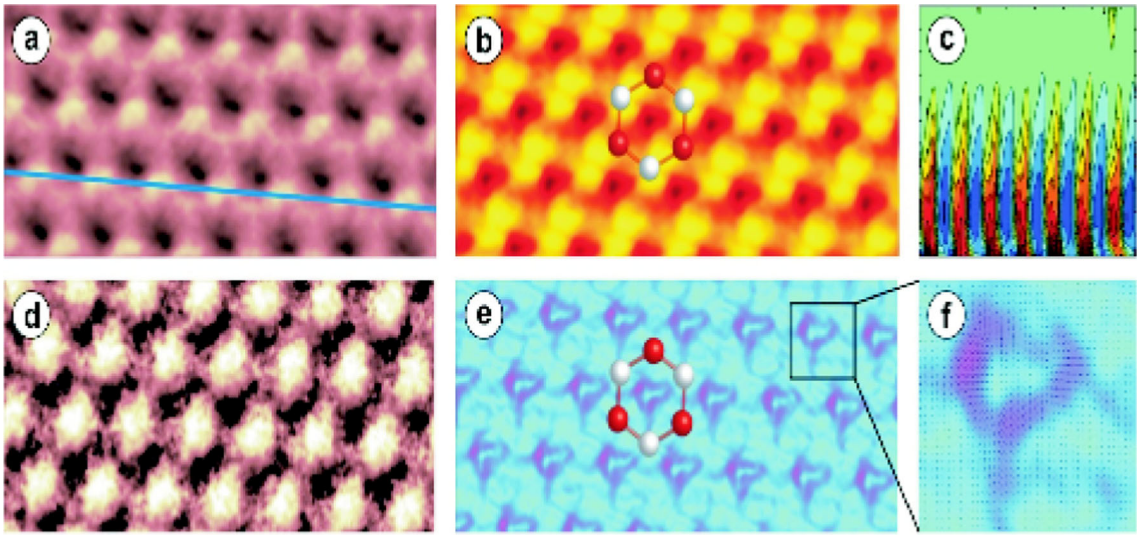

FIG. 26 (color online). 1750×810 pm^2 3D force microscopy on graphite, illustrating some of the various information channels that can be recorded simultaneously (Albers *et al.*, 2009a, 2009b; Baykara *et al.*, 2010). (a) *x*-*y* cut through the 3D force data at constant height. The average attractive force in this image is -2.306 nN with a total force corrugation of about 70 pN. (b) *x*-*y* potential energy data from the same height over the surface as in (a). The average energy is -5.47 eV with a total corrugation of $\sim$38 meV. (c) 2D cross section along the line plotted in (a), showing how the sample's surface force field extends into the vacuum (height 220 pm). The average force at each height has been subtracted to enhance contrast. Contour lines mark force differences of 8 pN at every height. (d) Map of the energy dissipated during oscillation. The color scale spreads from 250 meV (dark) to 295 meV (bright). (e) Map of the absolute values of the lateral forces acting on the tip during closest approach. Lateral forces are between 0 and 120 pN. (f) Zoom into the area highlighted in (e), where the direction and strength of the lateral forces are indicated by vectors. Note that in (b) and (e), the positions of the carbon atoms have been marked with an exemplary hexagonal ring. From Albers *et al.*, 2009b.

oscillation (Ternes *et al.*, 2008; Baykara *et al.*, 2010). Several channels of information are illustrated in Figs. 26(a)–26(f). Such information may have importance in fields such as surface catalysis, thin-film growth, chemical identification, imaging of individual surface species, molecular electronics, device fabrication, and nanotribology.

VI. HIGH-RESOLUTION OPTICAL MICROSCOPY AND SPECTROSCOPY

Among the key challenges for nanoscale metrology are the development of (1) instrumentation for subsurface imaging and characterization, (2) minimally invasive instrumentation, and (3) chemically specific characterization techniques. Nanoscale subsurface characterization is a key requirement for the study of buried interfaces, analysis of material defects, and for imaging functional devices underneath protecting capping layers. Existing high-resolution microscopies, such as scanning electron microscopy, AFM, or STM, are mostly surface sensitive. On the other hand, all materials are transparent in selected electromagnetic frequency windows, which opens up the possibility of probing subsurface features. However, diffraction associated with wave propagation limits the attainable resolution, usually to a fraction of the wavelength λ. Since the wavelength is inversely proportional to the energy E, the brute-force approach to increasing spatial resolution is to increase the energy of the incoming radiation. However, a high-energy dose affects the properties of the sample under investigation and can lead to artifacts and sample damage. Furthermore, high-energy radiation is not matched with the energy range associated with electronic and vibrational transitions of matter (typically <10 and <1 eV, respectively) and hence the spectroscopic information content is limited.

Figure 27 illustrates the trade-off between microscopy and spectroscopy. While microscopy aims at visualizing a sample with high spatial resolution, spectroscopy is focused on identifying the composition of a sample through the analysis of the vibrational modes or electronic processes in a material.

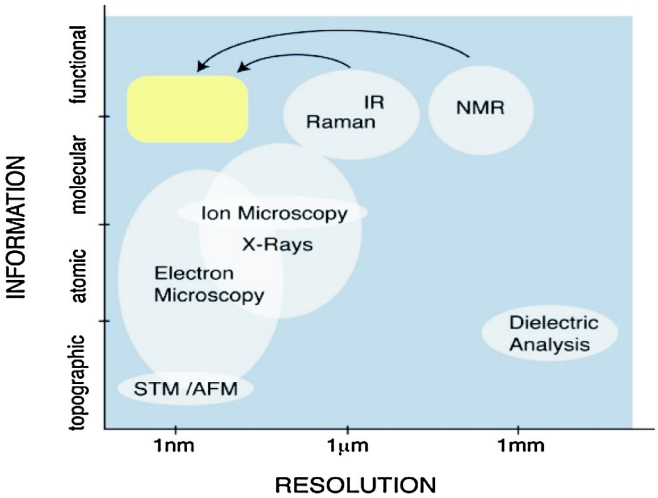

FIG. 27 (color online). Trade-off between chemical specificity and spatial resolution. The combination of chemically specific techniques (NMR, IR, Raman) with high-resolution techniques (STM, AFM) holds promise for measurements providing high-information-resolution products. Adapted from Courjon, 2003.

Making use of spectral information in microscopy makes it possible to enhance spatial resolution, and vice versa. For example, two point emitters can be resolved optically with diffraction-unlimited resolution if their electronic and/or vibrational structure is known. In fact, many microscopic techniques that claim ultrahigh spatial resolution require a high level of prior information about the properties of the sample, be it electronic or vibrational structure, or conductive or dielectric properties. The true challenge in microscopy is to visualize and to identify sample properties without requiring prior information about the sample. Chemical information is associated with the molecular structure in which the atoms are embedded. Various techniques provide information about a sample's elemental (atomic) composition, but since atoms can arrange in different molecular structures, elemental information is not sufficient for chemical imaging. Chemical information is related to the knowledge of how atoms are interacting in a molecular structure. The predominant analytical techniques for determining the chemical composition of materials are NMR and vibrational spectroscopy, such as infrared (IR) absorption or Raman scattering, as shown in Fig. 27. While the resolution of NMR is defined by the sensitivity (the smallest detection volume), the resolution of IR and Raman spectroscopic imaging are usually limited by diffraction. Several research efforts are currently under way to bring the spatial resolution of NMR and optical spectroscopy down to the nanometer range, thereby defining a high-resolution-information product. This section concentrates on optical techniques.

A. Specificity of light-matter interactions

Optical spectroscopy provides a wealth of information on structural, molecular, and dynamical properties of materials, which is due to the fact that the energy of light quanta (photons) is in the energy range of electronic and vibrational transitions. Diverse phenomena, such as the discrete energy levels in atomic gases, blackbody radiation, or the expanding universe, have been indirectly discovered by analyzing the properties of light. Today, chemically specific optical techniques such as IR absorption or Raman scattering are widely used in the pharmaceutical and food industries for measuring sample composition and quality control of products. However, besides its chemical specificity, the light-matter interaction has other favorable aspects:

- Light-matter interactions are weak (perturbation theory) and hence there is no strong perturbation of the sample properties.
- There is nomechanical contact and hence no wear of sample or probes.
- Materials have transparent frequency windows (for subsurface imaging).
- The light-matter interaction is fast (for time-resolved studies).
- The photon energies used are in the range of electronic and vibrational energies (for chemical specificity).
- Additional contrast mechanisms are available via polarization, coherence, or nonlinear interactions.

Infrared and optical spectroscopy embraces many attractive properties, and combining optical spectroscopy with microscopy is especially desirable because the spectral features can be spatially resolved. Until recently, the diffraction limit prevented researchers from resolving features smaller than half a wavelength of the applied radiation. Over the past two decades, different near-field approaches have been proposed and spatial resolution of 10 nm is now routinely achieved (Novotny and Stranick, 2006). However, most techniques are still challenged by technical difficulties and reproducibility of results. Once these challenges are overcome, near-field optical spectroscopy has the potential of providing high spatial resolution simultaneously with accurate chemical information. This information will be essential for understanding physical and chemical properties of nanoscale materials including proteins, semiconductor quantum structures, and nanocomposite materials.

B. Near-field optics

Nanoscale optical spectroscopy has its origins in near-field optics, the study of strongly localized fields and associated light-matter interactions (Novotny and Hecht, 2006). As illustrated in Fig. 28(a), the spatial resolution Δx of standard

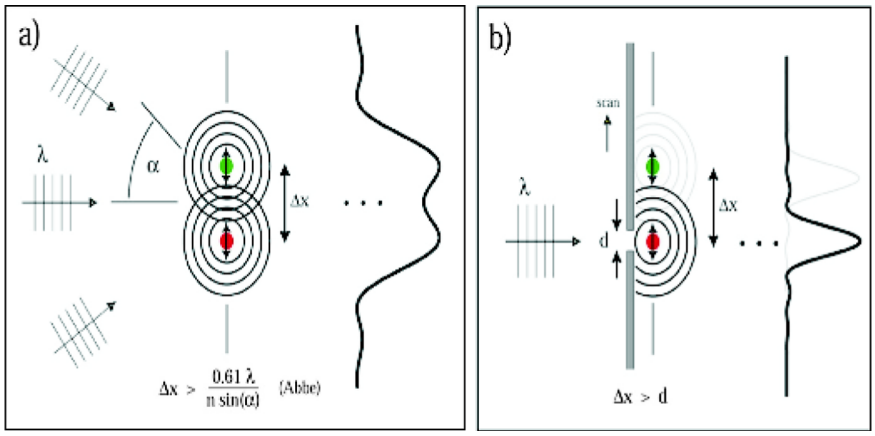

FIG. 28 (color online). Comparison of diffraction-limited optical microscopy and near-field optical microscopy. (a) Schematic of the diffraction limit showing the minimum detectable separation of two scatterers. (b) Schematic of aperture scanning near-field microscopy. To a first approximation, resolution is defined by the aperture size and not by the wavelength of the exciting radiation.

optical microscopy is limited by diffraction to roughly (Abbé criterion)

$$\Delta x = 0.61\lambda/\mathrm{NA},$$

where λ is the wavelength of the interacting radiation and $\mathrm{NA} = n\sin\alpha$ is the numerical aperture of the objective lens. The NA can be increased by a large index of refraction n of the surrounding medium or a larger angle of acceptance α. The latter two strategies are routinely applied in confocal microscopy (e.g., solid immersion lens microscopy or 4π microscopy).

In near-field optical microscopy, the resolution Δx no longer depends on λ but on a characteristic length d (e.g., aperture diameter, tip diameter, etc.) of a local probe. Near-field optical microscopy relies on a confined photon flux between the probe and the sample surface. The probe is raster scanned over the sample surface, and for every position (x, y) of the probe a remote detector acquires an optical response forming the contrast in the scan image. Synge (1928) conceptualized a local probe consisting of a small aperture in a perfectly reflecting metal screen [see Fig. 28(b)]. Immediately behind the irradiated screen, the light field is spatially confined to the size of the aperture (d). Only if a scatterer is within a distance d from the aperture will it interact with the radiation field. Synge's idea was soon forgotten because nanofabrication techniques were not available at the time. The experimental realization at optical frequencies had to wait for more than five decades (Lewis *et al.*, 1984; Pohl, Denk, and Lanz, 1984).

In the most widely adapted aperture approach (Betzig and Trautman, 1992), light is sent down an aluminum-coated fiber tip of which the foremost end is left uncoated to form a small aperture. Unfortunately, only a small fraction of the light coupled into the fiber is emitted through the aperture because of the cutoff of propagation of the waveguide modes (Novotny, 2007a). The low light throughput and the finite skin depth of the metal are the limiting factors for resolution. It is now doubted that an artifact-free resolution of 50 nm will be surpassed by the aperture technique. However, many applications in nanoscience, such as the study of membrane proteins, the characterization of defects and dopants in nanotubes, or local stress analysis in strained semiconductor devices, require higher spatial resolution. Moreover, the aperture technique has other practical complications: (1) the difficulty in obtaining smooth aluminum coatings introduces nonreproducibility in probe fabrication as well as measurements, (2) the flat ends of the aperture probes are not suitable for simultaneous topographic imaging with high resolution, and (3) the absorption of light in the metal coating causes significant heating and poses a problem for temperature-sensitive applications. Early progress in near-field optics has been summarized in several recent review articles (Fischer, 1998; Dunn, 1999; Courjon, 2003; Novotny, 2007a).

C. Optical antennas

At the heart of nanoscale optical spectroscopy is the strong localization of the light-matter interaction. Unlike other forms of scanning probe microscopy, the localization of optical fields relies on the *overall* shape of the local probe and not just on its foremost apex. The local probe assumes the function of an optical antenna, analogous to radio frequency and microwave antennas used to couple receivers or transmitters to free-propagating radiation (Novotny, 2007a). An optical antenna is defined as a device designed to convert free-propagating optical radiation efficiently to localized energy, and vice versa. In the context of microscopy, an optical antenna effectively replaces a conventional focusing lens or objective, concentrating external laser radiation to dimensions smaller than the diffraction limit. Using optical antennas to localize the light-matter interaction it became possible to resolve optically, for example, single proteins in cell membranes (de Bakker *et al.*, 2008; Garcia-Parajo, 2008; Hoeppener and Novotny, 2008), local stress and charges in semiconductor devices (Huber *et al.*, 2007), defects in nanotubes (see Fig. 29) and other nanomaterials (Anderson, Hartschuh, and Novotny, 2007), and phase transitions in strongly correlated materials (see Fig. 31) (Qazibash *et al.*, 2007). The techniques go under different names, such as tip-enhanced near-field optical microscopy, tip-enhanced Raman scattering, or more generally scanning near-field optical microscopy (SNOM or NSOM).

The analogy between near-field optics and antenna theory provides a solid theoretical foundation for enhancing the local light-matter interaction and for designing efficient optical probes for high-resolution imaging (Novotny, 2007a; Taminiau *et al.*, 2007, 2008). Among the implemented and studied optical antenna structures are bow-tie antennas (Farahani *et al.*, 2005; Schuck *et al.*, 2005), nanoparticle antennas (Kühn *et al.*, 2006; Bharadwaj, Anger, and Novotny, 2007), half-wave antennas (Novotny, 2007a), and quarter-wave antennas (Taminiau *et al.*, 2007, 2008). It was demonstrated that the transition rates and the efficiencies of single quantum emitters, such as molecules, ions, or quantum dots, can be controlled with an optical antenna (Anger, Bharadwaj, and Novotny, 2006). These studies validate existing theoretical models for the light-matter interaction and they open the door for engineering the properties of optical materials at the single-molecule level. Furthermore, they provide important feedback for the design of photovoltaic cells and light-emitting devices with improved efficiency (Taminiau *et al.*, 2008; Schuller, Taubner, and Brongersma, 2009).

It is important to emphasize that what is measured in a near-field optical experiment is not the optical properties of the sample but rather the optical interaction between the probe (antenna) and the sample. Theoretical studies showed that the electric field $\mathbf{E}$ associated with the probe-sample interaction can be written as a series of interaction orders (Carney *et al.*, 2004; Sun, Schotland, and Carney, 2007)

$$\mathbf{E} = \mathbf{E}P + \mathbf{E}S + \mathbf{E}SP + \mathbf{E}PS + \mathbf{E}PSP + \cdots.$$

Here $\mathbf{E}P$ corresponds to the field scattered by the probe and $\mathbf{E}S$ to the field scattered by the sample. Correspondingly, $\mathbf{E}SP$ is the field scattered by the sample and then by the probe, $\mathbf{E}PS$ is the field scattered by the probe and then by the sample, and $\mathbf{E}PSP$ is the field scattered by the probe then the sample and finally the probe again. Modulation techniques have been developed to reject the two lowest-order terms $\mathbf{E}P$ and $\mathbf{E}S$ (Taubner, Hillenbrand, and Keilmann, 2003; Deutsch,

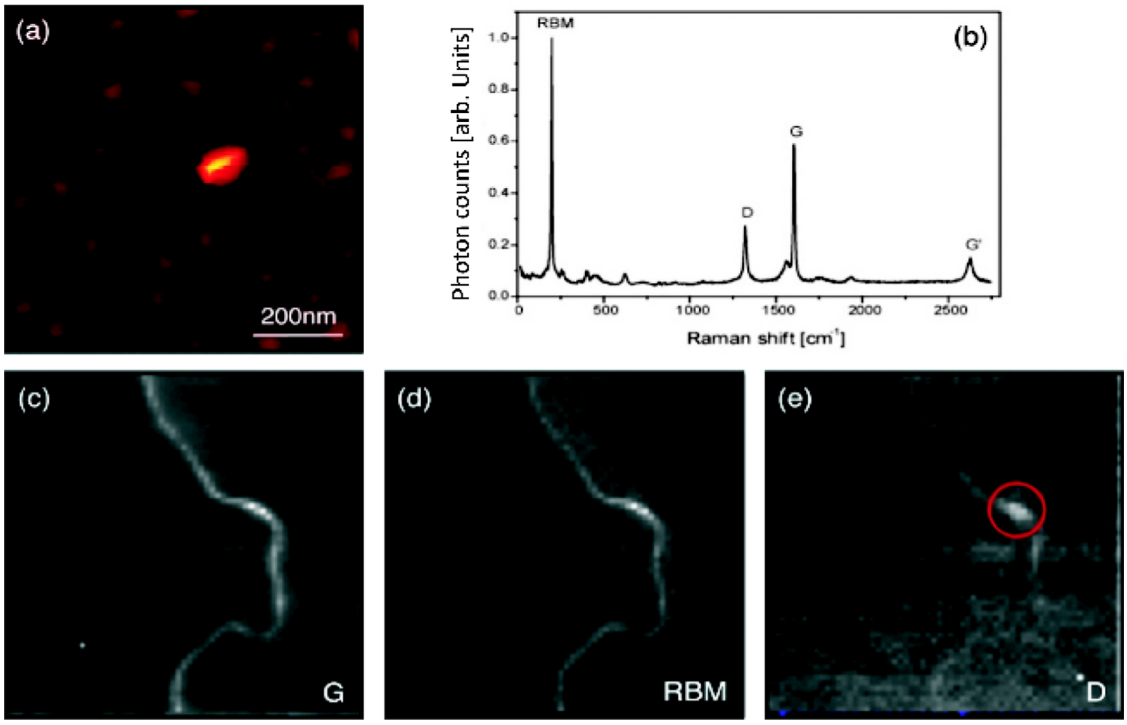

FIG. 29 (color online). Near-field Raman imaging of single-walled carbon nanotubes. (a) Topography showing individual catalyst particles and a hidden carbon nanotube. (b) Near-field Raman scattering spectrum of a carbon nanotube. Near-field Raman images of the (c) *G*-band intensity, (d) ring breathing mode (RBM) intensity, and (e) *D*-band intensity. All images are acquired simultaneously. The RBM frequency of 259 cm^{-1} identifies the tube as an (8,5) nanotube with a diameter of 0.9 nm. The *D*-band intensity is related to defects in the carbon nanotube structure. (e) The nanotube is locally perturbed by a larger catalyst particle.

Hillenbrand, and Novotny, 2008; Rang *et al.*, 2008), and depending on the experimental situation (e.g., strong probe and weak sample) it is possible to reduce the interaction series to only one term. Of special interest are the higher-order terms ($\mathbf{E}PSP$, $\mathbf{E}SPS$, etc.) because they do not linearly propagate from one plane ($z = \text{const}$) above the sample to another such plane. In other words, while it is possible to propagate the field $\mathbf{E}SP$ from the sample surface to any other plane above the surface, the same cannot be accomplished with $\mathbf{E}PSP$. Consequently, the field $\mathbf{E}PSP$ measured in different planes $z = \text{const}$ provides nonredundant information, which can be used in tomographic reconstructions of nanoscale features buried underneath the sample surface (Sun *et al.*, 2009). Future experiments will show if subsurface near-field tomography can be successfully translated into practice.

D. Near-field infrared nanoscopy

Applications of IR spectromicroscopy in science and technology extend to such diverse areas as physics, chemistry, life sciences and biology, materials science and engineering, forensics, and national security. The underlying reason behind such an unprecedented scope is that many fundamental properties of matter have characteristic energy scales in the infrared range. Conventional and synchrotron-based IR microscopy enables characterization of these properties in inhomogeneous substances with the diffraction-limited spatial resolution (10–50 μm). The impact of IR microscopy in both life and materials and physical sciences strongly motivates the development of experimental approaches suitable for an infrared probe of matter at the nanoscale. Recently, significant progress in infrared *nanoscopy* was achieved by several research groups through an innovative combination of atomic force microscopy and IR lasers. Novel scanning near-field IR instrumentation facilitates both spectroscopy and imaging with the spatial resolution down to 10 nm or better.

Figure 30 shows a schematic of a near-field nanoscope originally developed by Keilmann and Hillenbrand (2004). Here the tip of an AFM is illuminated with radiation from a tunable IR laser: a CO_2 laser, quantum cascade laser, or broadband IR frequency-comb source based on femtosecond lasers. The cantilever tip, an IR laser, and detector are arranged in a Michelson interferometer scheme. The principal task of the interferometer is to enable measurements of both the amplitude and phase of backscattered radiation. Since both the amplitude and phase are directly accessible, this instrument allows one to infer local values of the optical constants of studied specimens at the frequency of the laser source (Hillenbrand and Keilmann, 2000). The operation principle displayed in Fig. 30 is compatible with spectroscopy and imaging across a broad region of the electromagnetic spectrum: from gigahertz (Ma and Levy, 2006; Lai *et al.*, 2007) and terahertz (Huber *et al.*, 2008; Planken, 2008) frequencies to visible light. Importantly, the spatial resolution is determined solely by the radius of the tip appex and not by the wavelength of light. This latter circumstance allows one to achieve imaging with the resolution on the order of 10 nm even at gigahertz frequencies. These functionalities of near-field IR nanoscopy already enabled nanoscale exploration of previously unattainable characteristics of a variety of materials including semiconductors, polymers (Raschke *et al.*, 2005), correlated electron oxides (see Fig. 31), as well as

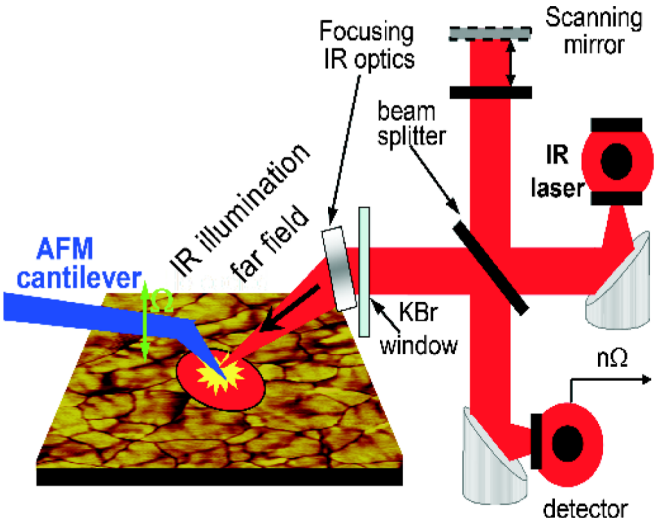

FIG. 30 (color online). Schematics (not to scale) of the scattering scanning near-field infrared nanoscope. The basic building block of the proposed apparatus is an AFM. The tip of the AFM is illuminated with an infrared laser. The scattered signal is registered using an interferometric scheme enabling direct measurements of both amplitude and phase of the scattered light. Interferometric detection is imperative to produce images of local values of optical constants free of topographic artifacts.

single viruses (Brehm *et al.*, 2006). A combination of broadband ellipsometry and near-field nanoimaging facilitated significant advances in the understanding of the electronic correlations in transition-metal oxides (Qazibash *et al.*, 2007; Driscoll *et al.*, 2008; Frenzel *et al.*, 2009).

The proximity of an optical probe (antenna) close to an atomic or molecular system introduces new interaction channels that are not present in free space. For example, energy transfer from an excited atom or molecule to the antenna can lead to fluorescence quenching, and local modification of the electromagnetic density of states influences the transition rates between states and, in the extreme case, can even affect the eigenstates of the system (Novotny, 2008; Taminiau *et al.*, 2008). In free space, the momentum of a photon with energy $E = h\nu$ is $p_{\mathrm{ph}} = h\nu/c$, with ν the frequency and c the speed of light. In contrast, the momentum of an unbound electron with the same energy is $p_e = (2m^*h\nu)^{1/2}$, which is a factor of $(2m^*c^2/h\nu)^{1/2} \approx 10^2$–$10^3$ larger than the photon momentum. Therefore, the photon momentum can be neglected in electronic transitions. However, near optical antennas, the photon momentum is no longer defined by its free-space value. Instead, it is related to the spatial confinement Δ of the localized optical fields, which results in near-field photon momenta as high as $p_{\mathrm{ph}} = h/\Delta$. For confinements $\Delta = 1$–10 nm the photon momentum can be increased by a factor of $\lambda/\Delta \approx 100$ over its free-space value. Thus, momentum associated with localized optical fields is comparable with the electron momentum in matter, especially in materials with small effective mass m^*. This correspondence can give rise to "diagonal" transitions in an electronic band diagram, thereby increasing the overall absorption strength.

Field localization affects not only the photon momentum but also the selection rules associated with the light-matter interaction. The latter involves matrix elements of the form $\langle f|\mathbf{pA}|i\rangle$, with $\mathbf{p}$ and $\mathbf{A}$ the momentum and field operators, respectively. As long as the quantum wave functions of states $|i\rangle$ and $|f\rangle$ are much smaller than the spatial extent over which $\mathbf{A}$ varies it is legitimate to move $\mathbf{A}$ out of the matrix element. The remaining expression $\langle f|\mathbf{p}|i\rangle$ gives rise to the familiar dipole approximation and dipole selection rules. However, the localized fields near optical antennas vary over length scales of a few nanometers and hence it may no longer be legitimate to invoke the dipole approximation. This is especially the case in semiconductor nanostructures, where the low effective mass gives rise to quantum orbitals with large spatial extents (Zurita-Sanchez and Novotny, 2002).

The resolution and the sensitivity in nanoscale optical spectroscopy depend on the efficiency of optical antennas, i.e., on the ability of an optical probe to enhance the local fields. The study of optical antennas is in its infancy and much work remains to be done. At first sight, one could attempt to downscale traditional antenna designs from the radio frequency to the optical regime. Unfortunately, this downscaling fails because metals are no longer good conductors at optical frequencies, but instead behave as strongly coupled plasmas. Hence, the antenna response is dictated not only by the incident radiation but also by the dynamics of the

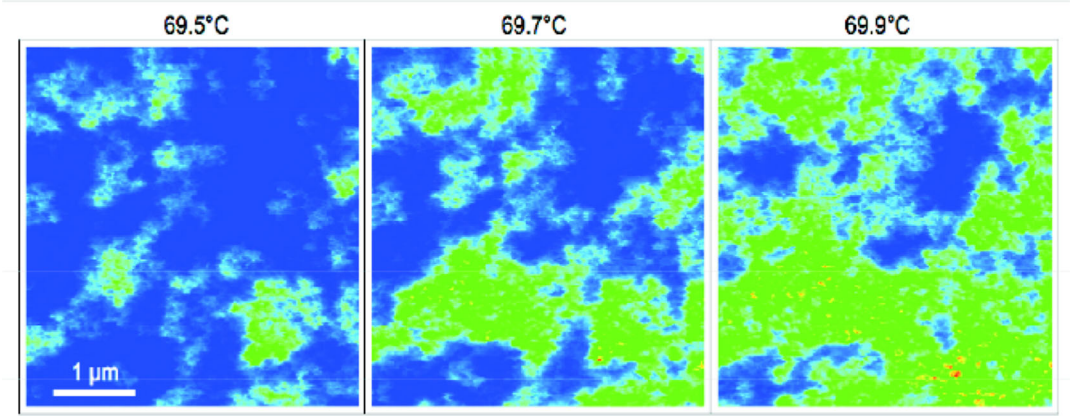

FIG. 31 (color online). Infrared snapshot images taken during the critical temperature range of the Mott transition of VO_2. The transition from insulator to metal proceeds by temperature-induced growth and coalescence of initially separate metal puddles. From Qazilbash *et al.*, 2007.

electrons in the metal (Novotny, 2007a; Bryant, de Abajo, and Aizpurua, 2008). The coupling between the antenna and the sample also needs further study as it influences the antenna properties and its efficiency. Light localization with optical antennas is ultimately limited by the nonlocal material response, which comes into play when the size of the structures becomes comparable with the electron mean free path (Aizpurua and Rivacoba, 2008; de Abajo, 2008; Zuloaga, Prodan, and Nordlander, 2009), such as near corners, tips, and gaps. Nonlocal effects have thus far been studied only qualitatively and more dedicated studies are necessary to understand the limits of light localization and enhancement.

The local light-matter response needs to be discriminated from the background due to direct sample irradiation. Different approaches have been put forth in the past years, ranging from modulation techniques (Hillenbrand and Keilmann, 2000; Gerton *et al.*, 2004; Novotny, 2007a) to irradiation with inhomogeneous laser beams. Improved schemes for background suppression lead to better sensitivity and a better signal-to-noise ratio. Different light-matter interaction mechanisms are being explored in nanoscale optical spectroscopy, including fluorescence, Raman scattering, coherent anti-Stokes Raman spectroscopy , IR absorption, and terahertz-frequency spectroscopy. Of particular interest are nonlinear interactions (Sanchez, Novotny, and Xie, 1999; Ichimura *et al.*, 2004; Danckwerts and Novotny, 2007) that scale with higher powers of the local field enhancement factor and therefore allow much higher sensitivities to be achieved.

Near-field nanoscopy is likely to enable breakthrough results in studies of imhomogeneous and phase-separated systems. Such inhomogeneties are known to occur in many systems of great current interest in the context of energy technologies including but not limited to high-T_c superconductors, plastic solar cells, electrochromics, materials employed for hydrogen storage, etc. In systems where multiple phases coexist on the nanometer scale, the dynamical properties of these individual electronic phases remain unexplored because methods appropriate to study charge dynamics (transport, infrared, optical, and many other spectroscopies) lack the required spatial resolution. Scanning near-field infrared nanoscopy can circumvent this long-standing limitation. Provided that near-field nanoscopy can be accomplished in cryogenic environments, one can expect major impact of these experiments in a variety of subfields of condensed matter physics and materials science. Equally important is a realization of true broadband near-field spectroscopy carried out simultaneously with imaging. Extension of nanoimaging and spectroscopy to far-IR and terahertz frequencies is particularly challenging and potentially beneficial.

VII. NANOELECTROMECHANICAL PHENOMENA IN SCANNING PROBE MICROSCOPY

Coupling between electrical and mechanical phenomena is one of the fundamental physical mechanisms manifested in materials ranging from ferroelectrics and III-V nitrides to electroactive polymers to biological systems (Kalinin *et al.*, 2007a; MRS Bulletin, Sept. 2009). Electromechanics refers to a broad class of phenomena in which mechanical deformation is induced by an external electric field, or, conversely, electric charge separation is generated by the application of an external force. Examples of electromechanical coupling include piezoelectricity (i.e., polarization-strain coupling) in inorganic piezoelectrics- and ferroelectrics (Newnham, 2005), flexoelectricity (i.e., polarization,–strain gradient coupling) in nanomaterials (Cross, 2006; Maranganti, Sharma, and Sharma, 2006), 2D crystals (Kalinin and Meunier, 2008; Naumov, Bratkovsky, and Ranjan, 2009), cellular membranes (Petrov and Sachs, 2002), and complex electromechanical phenomena associated with phase transitions and electrochemical reactions. In most materials, electromechanical activity is directly related to their structure and functionality. In polar compounds, local piezoelectric properties are strongly affected by structural defects and disorder. In ferroelectrics and multiferroics, electromechanical behavior can be used to study a wide range of phenomena including polarization reversal mechanisms, domain wall pinning, and cross-coupled phenomena. Finally, electromechanical coupling is a key component of virtually all electrochemical transformations, in which changes in the oxidation state are associated with changes in molecular shape and bond geometry, and is an integral factor in operation of solid-state energy storage and conversion materials.

The measurements of bias-induced sample deformation in piezoelectric materials using scanning acoustic microscopy (Güthner, Glatz-Reichenbach, and Dransfeld, 1991) and STM (Birk *et al.*, 1991) were reported as early as 1991. Force-based methods were extended to piezoelectric materials (Güthner and Dransfeld, 1992) and to ferroelectric domain visualization (Luthi *et al.*, 1993; Bae *et al.*, 1994) shortly thereafter. Papers by Takata *et al.* (1994) and Takata (1996) using strain imaging via tunneling acoustic microscopy, Franke *et al.* (1994), Kolosov *et al.* (1995, 1995), Gruverman *et al.* (1995, 1997), Gruverman, Auciello, and Tokumoto (1996, 1998), Gruverman, Hatano, and Tokumoto (1997), and Hidaka *et al.* (1997) followed. The work of Gruverman and colleagues demonstrated imaging and switching in inorganic ferroelectrics and they coined the terms ''piezoresponse'' and ''piezoresponse force microscopy'' (PFM), which have now become standard, opening the pathway for broad use of PFM by ferroelectric and oxide community. In the past decade and a half, PFM has become the key tool for studying static and dynamic properties of ferroelectric materials (Hong, 2004; Alexe and Gruverman, 2004; Gruverman and Kholkin, 2006; Kalinin and Gruverman, 2007; Kalinin *et al.*, 2007a; Gysel *et al.*, 2008; Rai *et al.*, 2010). Piezoresponse force microscopy has been extended to ferroelectric polymers (Matsushige *et al.*, 1998; Rankin *et al.*, 2007; Rodriguez *et al.*, 2007a; Gaynutdinov *et al.*, 2008; piezoelectric semiconductors GaN (Rodriguez *et al.*, 2002a; Stoica *et al.*, 2007), AlN (Rodriguez *et al.*, 2002a; Dalmau *et al.*, 2005), ZnO (Zhao, Wang, and Mao, 2004; Fan, Werner, and Zacharias, 2006; Scrymgeour *et al.*, 2007), and piezoelectric biopolymers (Halperin *et al.*, 2004; Kalinin *et al.*, 2005b; Kalinin *et al.*, 2007b; Minary-Jolandan and Yu, 2009a, 2009b).

A. Probing electromechanics at the nanoscale

Electromechanical coupling is ubiquitous in inorganic, biological, and molecular systems. However, small electromechanical coupling coefficients ($\sim$ 2–100 pm/V) render

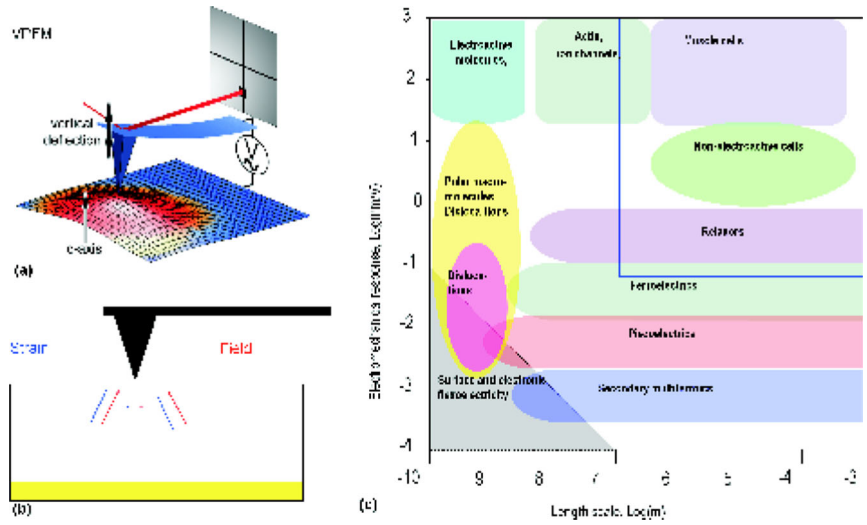

FIG. 32 (color online). (a) Schematics of piezoresponse force microscopy (PFM) measurements. Electric bias applied to an SPM tip in contact with the surface creates an electric field within material (b) that generates strain due to piezoelectric or more complex electromechanical coupling. The nonuniform strain results in surface deformation detected as the SPM tip deflection. (c) Electromechanical coupling in functional materials. The solid lines correspond to estimated limits of nanoindentation and atomic force microscopy, while the dashed lines correspond to the ultimate limits that can be achieved through the instrumentation development including resonant-enhanced modes, low-noise beam deflection position systems, and high-stability platforms. From Kalinin *et al.*, 2008a.

measurements difficult, even in piezoelectric crystals, since typical piezoelectric displacements induced by moderate (1–100 V) biases are typically in the low nanometer range. The properties of thin films have become accessible only in the last two decades with the advent of single- and double-beam interferometry techniques (Kholkin, Wuthrich *et al.*, 1996; Kholkin *et al.*, 1996; Maeder *et al.*, 1996; Muralt *et al.*, 1996; Kholkin *et al.*, 1997). However, difficulties in technical implementation and poor spatial resolution have resulted in only limited applications. The breakthrough in electromechanical imaging and spectroscopy of polar and ferroelectric materials has been enabled in the last decade by the emergence of PFM, as illustrated in Fig. 32.

In PFM, an electrically conductive cantilevered tip traces surface topography using standard deflection-based feedback, also known as contact-mode imaging. During scanning, a sinusoidally varying electrical bias is applied to the tip, and the electromechanical response of the surface is detected as the first harmonic component of the bias-induced tip deflection. The response amplitude and phase provide a measure of the local electromechanical activity of the surface (Gruverman and Kholkin, 2006). The operation of the PFM is complementary to that of conventional SPMs. For techniques such as STM, an electrical bias is applied to a metal tip, and the tunneling current is measured. In the case of AFM, a force is applied, and the resulting tip deflection is measured. In PFM, an electrical bias is applied to a tip, and the tip deflection resulting from the deformation of the sample is measured. In AFM, this results in an image formation mechanism that is sensitive to surface topography and can be enhanced by resonance techniques. However, the contact stiffness of the tip-surface junction scales proportionally with the contact radius, resulting in the topographic cross talk inherent to many force-based SPM imaging modes (e.g., phase imaging). In contrast, the electromechanical response in PFM depends only weakly on the tip-contact area, thus minimizing cross talk for low-frequency imaging (Kalinin *et al.*, 2007c). Despite uncertainties in the quantitative interpretation of PFM, it has emerged as the primary tool for studying polarization dynamics in ferroelectric materials, bringing about advances such as sub-10 nm resolution imaging of domain structures (Gruverman, Auciello, and Tokumoto, 1998), domain patterning for nanostructure fabrication (Kalinin *et al.*, 2002; Hanson *et al.*, 2006; Zhang *et al.*, 2007), and local spectroscopic studies of bias-induced phase transitions (Guo *et al.*, 2002; Le Rhun, Vrejoiu, and Alexe, 2007). The development of high-sensitivity PFM has enabled probing piezoelectric phenomena in weakly piezoelectric compounds such as III-V nitrides (Rodriguez *et al.*, 2002b) and biopolymers (~ 15 pm/V) (Halperin *et al.*, 2004; Kalinin *et al.*, 2006; Minary-Jolandan and Yu, 2009a), providing spectacular sub-10 nm resolution images of materials structures, based on differences in the local piezoelectric response.

B. Probing local bias-induced phase transitions

Strong coupling between polarization and electromechanical response allows using the latter as a functional basis of nanoscale probing of polarization distribution and switching processes in ferroelectrics. In PFM of ferroelectric and piezoelectric materials, the amplitude of the response is directly proportional to local polarization. This approach can be directly extended to probe local polarization dynamics. The probe concentrates an electric field to a nanoscale volume of material (diameter $\sim$10 nm), and induces local domain formation; see Fig. 33(a). Simultaneously, the probe detects the onset of nucleation and the size of a forming domain via detection of the electromechanical response of the material to a small ac bias (Jesse, Baddorf, and Kalinin, 2006); see Fig. 33(b). Thus, the local hysteresis loops obtained contain information on domain nucleation and growth processes; see Figs. 33(e) and 33(f).

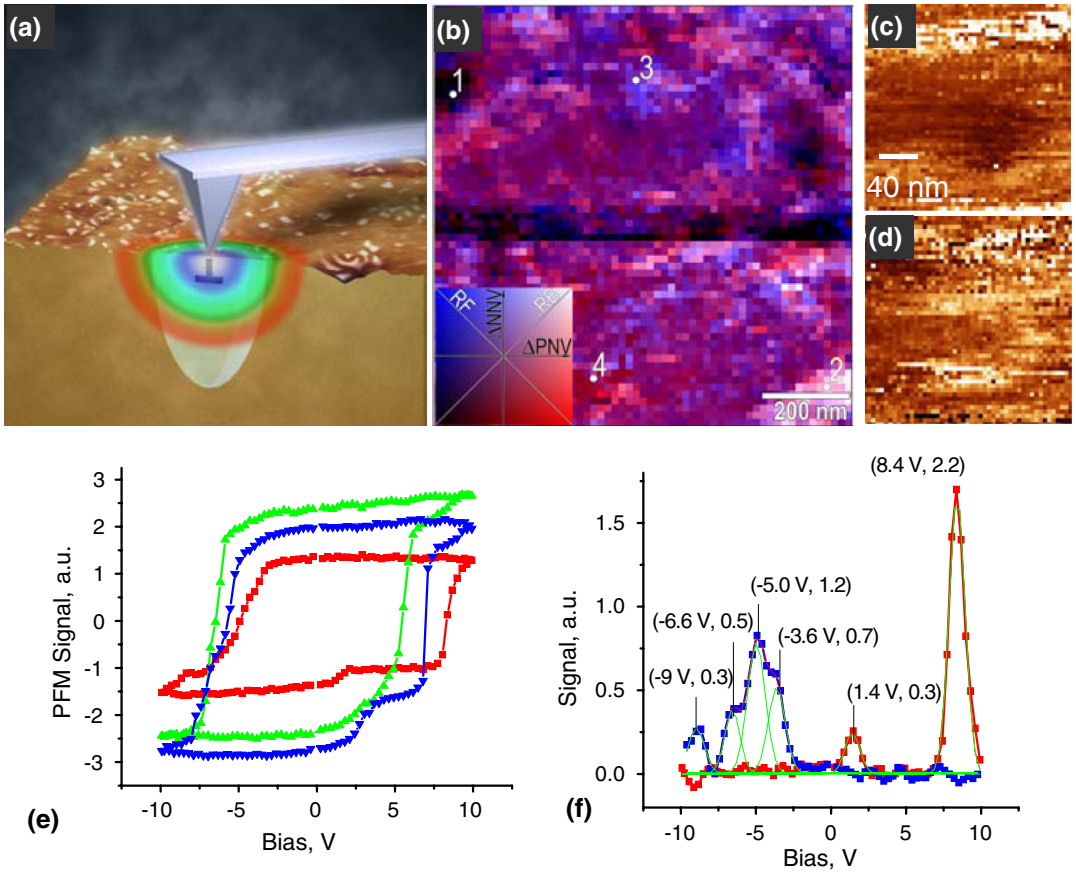

FIG. 33 (color online). (a) The confinement of an electric field by an AFM probe enables probing a bias-induced phase transition within a defect-free volume or at a given separation from defects. From Jesse *et al.*, 2008b. The color map (b) illustrates the disorder potential in an epitaxial lead zirconate titanate film. (c), (d) A single defect in multiferroic $BiFeO_3$ determined from the nucleation bias and fine structure features on a (e), (f) hysteresis loop. From Kalinin *et al.*, 2008b.

In switching spectroscopy PFM (SSPFM), hysteresis loops are acquired at each point of the image and analyzed to yield 2D maps of coercive and nucleation biases, imprint, work of switching, and switchable polarization. Maps of switching behavior can be correlated with surface structure and morphology. Recently, *spectroscopic* 3D (Jesse, Baddorf, and Kalinin, 2006; Jesse, Lee, and Kalinin, 2006; Rodriguez *et al.*, 2007a) and 4D (Jesse *et al.*, 2008b) PFM modes have been implemented on ambient SPM platforms to study switching processes in ferroelectrics. Measurements of local electromechanical response as a function of dc tip bias provide information on the size of the domains formed below the tip, and demonstrated that switching on low-defect-density samples is nearly intrinsic (Kalinin *et al.*, 2007a). This finding can be directly related to the signal generation volume in PFM (30 nm), which is well below that of the smallest ferroelectric capacitor, and thus contains a significantly smaller number (ideally, none) of the extended defects (e.g., dislocation spacing in high-quality epitaxial ferroelectric films can be as large as 100–300 nm). Furthermore, the edge effects, inevitable when material confinement is used, are minimized when field confinement by a SPM probe is employed. This finding was further corroborated by the temperature dependence of polarization switching achieved using low-temperature UHV PFM (Maksymovych, 2009). Recently, the development of the analytical (Morozovska *et al.*, 2009) and phase-field (Choudhury *et al.*, 2008) models opened the pathway toward predicting the mechanisms of bias-induced transitions. In systems with defects, the hysteresis loops were shown to demonstrate pronounced fine structure containing information on the interaction of nascent ferroelectric domain with localized defect (Le Rhun, Vrejoiu, and Alexe, 2007).

The spatially resolved mapping capabilities of SSPFM enabled insight into the spatial variability of switching in ferroelectric materials and nanosystems. Mapping the work of switching in ferroelectric nanodot arrays and within a single nanodot was demonstrated by Rodriguez *et al.* (2008). The variation of nucleation biases along the surface has been used to map the random-field and random-bond components of the disorder potential (Jesse *et al.*, 2008b). Extending spatial resolution further, the effects of *single* (unidentified) localized defects on the thermodynamics of local polarization switching were determined (Kalinin *et al.*, 2008b). Finally, the synergy of the systems with atomically engineered defect structures and phase-field modeling enabled deciphering mesoscopic phase transition mechanisms of the level of a single well-defined defect (bicrystal grain boundary) (Rodriguez *et al.*, 2009). This knowledge led to an approach to control the switching pathways in systems with multiple equivalent polarization states (Balke *et al.*, 2009), thus enabling control of strain and magnetization states in multiferroic materials.

The synergy between PFM and current detection enables studies of coupling between polarization and transport properties. In these measurements, the local bias applied to the SPM probe results in local polarization reversal; the simultaneously measured tip-surface current provides information on polarization-mediated tunneling (Maksymovych *et al.*, 2009); see Fig. 34. Alternatively, transport can be measured across the ferroelectric domain walls (Seidel *et al.*, 2009; Yunseok, Marin, and Ekhard, 2010) or between domains (see Fig. 33) (Garcia *et al.*, 2009; Gruverman *et al.*, 2009). Beyond polarization, the local bias can induce a local metal-insulator transition (Yang *et al.*, 2009), suggesting the potential for energy-storage devices based on reversible electrochemical processes. Notably, similar approaches can be used for mapping thermal phase transitions, when the heated tip is used to confine the thermal field to a small volume of material (Nelson and King, 2007), and thermomechnical strains allow detection of dynamic changes in material structure (Jesse *et al.*, 2008a).

C. Band excitation PFM and SSPFM

One of the key aspects of force-based dynamic SPMs is the systematic use of resonant enhancement, which allows amplification of the weak interactions at the tip-surface junction due to the mechanical amplifier effect (Sarid, 1994). However, for PFM the direct use of resonant enhancement is impossible, since the contact resonance frequency strongly depends on position on the (uneven) sample surface. At the same time, the use of phase-locked loop frequency tracking methods is obviated by the lack of a one-to-one relationship between the applied bias and phase of the response (as opposed to the acoustically driven SPMs). To address this problem, a number of alternative dynamics modes have been developed. In the dual ac resonant tracking mode, the amplitude-based feedback is used for maintaining resonance and directly determining the dissipation from peak width or response phases (Rodriguez *et al.*, 2002c, 2007a, 2007b; Gannepalli *et al.*, 2011). The band excitation (BE) approach provides alternatives to standard single-frequency methods by exciting and detecting response at all frequencies *simultaneously* (Jesse *et al.*, 2007). Band excitation introduces a synthesized digital signal that spans a continuous band of frequencies and monitors the response within the same (or larger) frequency band; see Figs. 35(a)–35(c). The cantilever response is detected using high-speed data acquisition methods and then Fourier transformed. The resulting amplitude-frequency and phase-frequency curves are collected at each point and stored in 3D data arrays. These data are analyzed to extract relevant parameters of the cantilever behavior. For example, the resonance frequencies, response amplitudes, and Q factors are deconvoluted and stored as images [see Figs. 35(e)–35(g)], and, in the case of adaptive control, can be used as a feedback signal in microscope operation.

The band excitation and spectroscopic SPM can be synergistically combined to give rise to new families of multidimensional SPM methods, as exemplified by band excitation switching spectroscopy PFM. Conventional piezoforce spectroscopy utilizes a pulse train of increasing magnitude to switch the probed volume of the ferroelectric, while a single-frequency ac signal is used to measure the piezoresponse of the switched volume between the pulses. The band excitation wave form exciting the tip during the bias-off step enables the rapid (~3 ms) sampling of the full

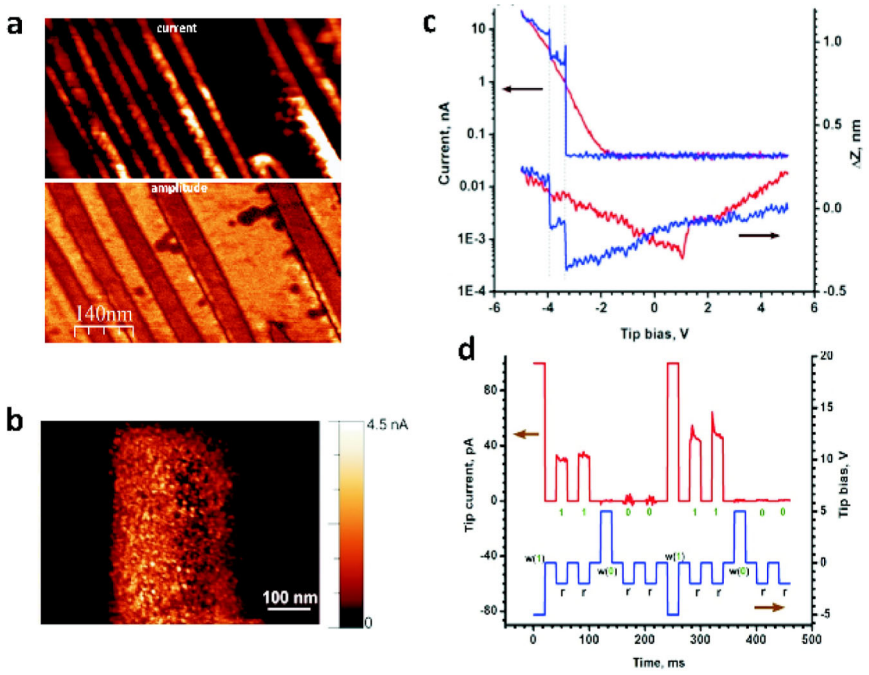

FIG. 34 (color online). (a) Domain wall conductance in $BiFeO_3$ thin films. (b) Tip-induced metal-insulator transition in Ca-doped $BiFeO_3$. (c) Simultaneous measurements of bias-induced strain and tip-surface current, illustrating the perfect correlation between polarization switching and transport. The double peak is due to the presence of defect and is observed in ~10% of cases. (d) The combination of high-voltage writing and low-voltage readout enables nonvolatile data storage. From Yang *et al.*, 2009 and Maksymovych *et al.*, 2009.

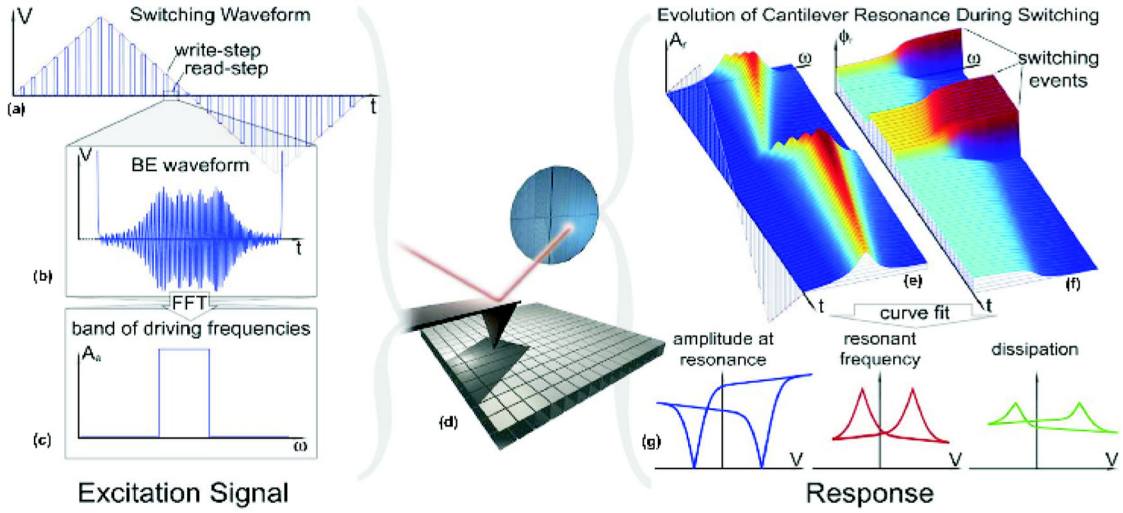

FIG. 35 (color online). Data acquisition and processing. (a) Ferroelectric switching is induced by a pulse train of increasing dc bias while the changes in the piezoresponse, contact stiffness, and dissipation are measured by exciting the cantilever over a narrow frequency band around its contact resonance (b),(c). The ferroelectric hysteresis is measured across a grid of points (d) resulting in a spatially resolved 4D data set, where each point represents the cantilever's resonant response along the local hysteresis loop (e),(f). The resonant response (amplitude and phase) is then by a simple harmonic oscillator model to yield the resonance amplitude, resonance frequency, and Q factor (g) as a function of the dc bias. From Jesse, Maksymovych, and Kalinin, 2008.

response-frequency curve in the vicinity of the resonance. After acquisition, the resulting 4D data set is analyzed to yield the voltage dependence of the materials properties. Briefly, the frequency response curve $\{A, \theta\}(\omega)$ at each spatial and voltage point (x, y, V_{dc}) is modeled to yield local electromechanical response, Q factor (i.e., dissipation), and resonant frequency. The bias dependence of the electromechanical activity, defined as either response at maximum or integrated peak intensity, yields the local PFM hysteresis loop. The hysteresis loop data can be analyzed to provide the local nucleation and coercive biases, remanent response, and work of switching that can be plotted as 2D maps. Provided that the resonant frequency and Q factor are bias independent, these can be plotted as local maps of elastic and dissipative properties. Alternatively, the bias-related changes in resonant frequency and Q factor within a cycle (reversible) and between the cycles (irreversible) provide insight into previously inaccessible polarization- and voltage-related changes in local contact mechanics and dissipation. Recently, this approach was further extended to map the local Preisach densities (Mayergoyzid, 1986), giving rise to more complex 5D acquisition schemes.

A key element is the development of analysis methods to interpret multidimensional SPM data. Historically, interpretation of spectroscopic data is performed once a single 1D data array was available (e.g., as intensity and positions of the peaks) and images were interpreted as 2D maps of corresponding properties. As an example, Morozovska, Bdikin, and co-workers developed an extensive analytical framework for the analysis of bias-induced phase transitions from single spectra (Eliseev *et al.*, 2010):

- Describe the thermodynamics of bias-induced switching, including the defect effects.
- Determine the domain geometry for a given bias from the minimum of free energy (Kalinin *et al.*, 2005a).
- Determine the signal as a convolution of domain and signal generation volume (Morozovska *et al.*, 2006).
- Calibrate the probe geometry (Kalinin and Gruverman, 2007; Tian *et al.*, 2008).

However, the analytical solutions are extremely limited (e.g., to semiellipsoidal domains with only two geometric parameters), inconsistent with the lack of rotational symmetry in the problem and experimental observations.

The 3D and 4D spatially resolved spectroscopic tools necessitate data analysis in higher-dimensional parameter space, e.g., making correlations between spectra that are generally beyond our ability to visualize. Correlative models based on artificial neural networks (Haykin, 1998; Hagan, Demuth, and De Jesús, 2002) may offer a solution. In this approach, phase-field modeling or DFT is used to generate high-dimensional spectroscopic-imaging data describing defects of various kinds for a range of tip parameters to *predict* experimental 3D sets. These examples are analyzed using principal-component analysis or other projection and clustering techniques (e.g., self-organized feature maps) to extract the salient components. Thus, compressed data become the training sets for a neural network. Upon successful training, the neural network itself becomes a highly efficient, fast, and portable emulator of the computation model and can be used to interpret experimental data.

VIII. SUMMARY AND PROSPECTS

The previous sections reviewed how spatially localized probes of electromagnetic, electronic, optical, and force-based interactions are transforming our understanding of processes ranging from chemical reactions at surfaces to electron correlations in solids to dielectric polarization of atoms and molecules. These examples illustrate the fact that

the junction of a probe tip and surface contains a vast amount of information that can be experimentally accessed. In the context of Fig. 1, these advances represent extensions into the 3D regime of space, time, and function.

The continued development and application of the approaches presented here will undoubtedly have significant impact on our understanding of local phenomena, as have STM and AFM already. Transitioning probes of so-called continuum properties into the single-molecule regime will likely lead to a shift from many-body to quantum properties, and to new physical models. Spatially localized studies of electron correlation and electron spin are in their infancy. Localized probes will enable both understanding and applications in the rapidly developing field of plasmonics. Quantifying dynamics of chemical reactions and bond vibrational properties will open new windows to chemical control. The recent ability to use precision force control to map and to manipulate atoms at room temperature may lead to the construction of new compounds and structures. The ability to map a vector property such as piezoelectricity at nanometer spatial resolution opens new pathways to study systems ranging from viruses to information storage materials.

These results also suggest approaches that might be taken to address future challenges, such as the ultimate goal of atomic-resolution 3D imaging with high temporal resolution. Combinations and hybrids of the strategies outlined here will certainly be developed and further combined with electron and photon scattering tools. There remains plenty of room in the space-time-function regime to explore.

ACKNOWLEDGMENTS

This paper is one outcome of a workshop sponsored by the U.S. Department of Energy, Basic Energy Sciences on Frontiers in Imaging Functionality at the Atomic Scale in September 2008

REFERENCES

Abe, M., *et al.*, 2005, Appl. Phys. Lett. **87**, 173503.
Aizpurua, J., and A. Rivacoba, 2008, Phys. Rev. B **78**, 035404.
Albers, B. J., *et al.*, 2009a, Nanotechnology **20**, 264002.
Albers, B. J., *et al.*, 2009b, Nature Nanotech. **4**, 307.
Albrecht, T. R., *et al.*, 1991, J. Appl. Phys. **69**, 668.
Alexe, M., and A. Gruverman, 2004, Eds., *Nanoscale Characterization of Ferroelectric Materials* (Springer, Heidelberg).
Allers, W., *et al.*, 1999, Europhys. Lett. **48**, 276.
Alvarado, S. F., and P. Renaud, 1992, Phys. Rev. Lett. **68**, 1387.
Anderson, N., A. Hartschuh, and L. Novotny, 2007, Nano Lett. **7**, 577.
Anger, P., P. Bharadwaj, and L. Novotny, 2006, Phys. Rev. Lett. **96**, 113002.
Aoki, N., *et al.*, 2005, Appl. Phys. Lett. **87**, 223501.
Ashino, M., *et al.*, 2008, Nature Nanotech. **3**, 337.
Avouris, Ph., *et al.*, 1996, Surf. Sci. **363**, 368.
Bachtold, A., *et al.*, 2000, Phys. Rev. Lett. **84**, 6082.
Bae, M. K., T. Horiuchi, K. Hara, Y. Ishibashi, and K. Matsushige, 1994, Jpn. J. Appl. Phys. **33**, 1390.
Bai, C., 2000, *Scanning Tunneling Microscopy* (Springer, Berlin).
Balke, N., *et al.*, 2009, Nature Nanotech. **4**, 868.
Bammerlin, M., *et al.*, 1997, Probe Microsc. **1**, 3.
Bartelt, N. C., T. L. Einstein, and E. D. Williams, 1994, Surf. Sci. **312**, 411.
Barth, C., and M. Reichling, 2001, Nature (London) **414**, 54.
Barth, J. V., *et al.*, 2005, Nature (London) **437**, 671.
Bartolini, P., *et al.*, 2007, Philos. Mag. **87**, 731.
Batzill, M., K. Katsiev, J. M. Burst, U. Diebold, and B. Delley, 2005, Phys. Rev. B **72** 165414.
Baykara, M. Z., *et al.*, 2010, Adv. Mater. **22**, 2838.
Bergmann, K. V., M. Bode, and R. Wiesendanger, 2004, Phys. Rev. B **70**, 174455.
Besenbacher, F., 1996, Rep. Prog. Phys. **59**, 1737.
Betzig, E., and J. K. Trautman, 1992, Science **257**, 189.
Bharadwaj, P., P. Anger, and L. Novotny, 2007, Nanotechnology **18**, 044017.
Binnig, G., C. F. Quate, and Ch. Gerber, 1986, Phys. Rev. Lett. **56**, 930.
Binnig, G., and H. Rohrer, 1982, Helv. Phys. Acta **55**, 726.
Birgeneau, R. J., and M. A. Kastner, 2000, Science **288**, 437.
Birk, H., J. Glatz-Reichenbach, L. Jie, E. Schreck, and K. Dransfeld, 1991, J. Vac. Sci. Technol. B **9**, 1162.
Blake, M. B., *et al.*, 2009, J. Phys. Chem. A **113**, 13 167.
Bockrath, M., W. Liang, D. Bozovic, J. H. Hafner, C. M. Lieber, M. Tinkham, and H. Park, 2001, Science **291**, 283.
Bode, M., 2003, Rep. Prog. Phys. **66**, 523.
Bode, M., M. Getzlaff, and R. Wiesendanger, 1998, Phys. Rev. Lett. **81**, 4256.
Bode, M., *et al.*, 2004, Phys. Rev. Lett. **92**, 067201.
Bode, M., *et al.*, 2007, Nature (London) **447**, 190.
Bonnell, D. A., 2000, Ed., *Scanning Probe Microscopy: Theory and Applications* (Wiley, New York), 2nd ed.
Bonnell, D. A., 2008, ACS Nano **2**, 1753.
Bonnell, D. A., and J. Garra, 2008, Rep. Prog. Phys. **71**, 044501.
Bonnell, D. A., and R. Shao, 2003, Curr. Opin. Solid State Mater. Sci. **7**, 161.
Brehm, M., T. Taubner, R. Hillenbrand, and F. Keilmann, 2006, Nano Lett. **6**, 1307.
Brukman, M., and D. A. Bonnell, 2008, Phys. Today **61**, 36.
Bryant, G. W., F. J. G. de Abajo, and J. Aizpurua, 2008, Nano Lett. **8**, 631.
Bumm, L. A., *et al.*, 1996, Science **271**, 1705.
Caciuc, V., *et al.*, 2008, Phys. Rev. B **77**, 045411.
Carney, P. S., *et al.*, 2004, Phys. Rev. Lett. **92**, 163903.
Cerdá, J., *et al.*, 1997, Phys. Rev. B **56**, 15 885.
Chen, C. J., 1992, Phys. Rev. Lett. **69**, 1656.
Chen, C. J., 2008, *Introduction to Scanning Tunneling Microscopy* (Oxford University Press, Oxford, UK), 2nd ed.
Chiesa, M., ,L. Burgi, J.-S. Kim, R. Shikler, R. H. Friend, and H. Sirringhaus 2005, Nano Lett. **5**, 559.
Cho, Y., and R. Hirose, 2007, Phys. Rev. Lett. **99**, 186101.
Choudhury, S., *et al.*, 2008, Appl. Phys. Lett. **93**, 162901.
Claridge, S. A., *et al.*, 2011, ACS Nano **5**, 693.
Coffey, D., and S. Ginger, 2006, Nature Mater. **5**, 735.
Courjon, D., 2003, *Near Field Microscopy and Near Field Optics* (Imperial College Press, London, UK).
Crommie, M. F., *et al.*, 1993, Science **262**, 218.
Cross, L. E., 2006, J. Mater. Sci. **41**, 53.
Dalmau, R., *et al.*, 2005, J. Cryst. Growth **281**, 68.
Danckwerts, M., and L. Novotny, 2007, Phys. Rev. Lett. **98**, 026104.
de Abajo, F. J. G., 2008, J. Phys. Chem. C **112**, 17 983.
de Bakker, B. I., *et al.*, 2008, J. Cell Sci. **121**, 627.
Deutsch, B., R. Hillenbrand, and L. Novotny, 2008, Opt. Express **16**, 494.
Diebold, U., 2003, Surf. Sci. Rep. **48**, 53.
Diebold, U., S. Li, and M. Schmid, 2010, Annu. Rev. Phys. Chem. **61**, 129.

Donhauser, Z. J., *et al.*, 2001, Science **292**, 2303.
Douheret, O., S. Bonsels, and S. Anand, 2005, J. Vac. Sci. Technol. B **23**, 61.
Driscoll, T., *et al.*, 2008, Appl. Phys. Lett. **93**, 024101.
Dulub, O., B. Meyer, and U. Diebold, 2005, Phys. Rev. Lett. **95**, 136101.
Dulub, O., *et al.*, 2007, Science **317**, 1052.
Dunn, B., 1999, Chem. Rev. **99**, 2891.
Dürig, U., 1999, Appl. Phys. Lett. **75**, 433.
Eguchi, T., *et al.*, 2004, Phys. Rev. Lett. **93**, 266102.
Eigler, D. M., and E. K. Schweizer, 1990, Nature (London) **344**, 524.
Eigler, D. M., P. S. Weiss, E. K. Schweizer, and N. D. Lang, 1991, Phys. Rev. Lett. **66**, 1189.
Electromechanics on the Nanoscale, MRS Bulletin, September, 2009.
Eliseev, E. A., A. N. Morozovska, M. D. Glinchuk, B. Y. Zaulychny, V. V. Skorokhod, and R. Blinc, 2010, Phys. Rev. B **82**, 085408.
Enevoldsen, G. H., , T. Glatzel, M. C. Christensen, J. V. Lauritsen, and F. Besenbacher, 2008, Phys. Rev. Lett. **100**, 236104.
Eyben, P., T. Janssens, and W. Vandervorst, 2005, Mater. Sci. Eng. B **124–125**, 45.
Eyben, P., *et al.*, 2004, J. Vac. Sci. Technol. B **22**, 364.
Fan, H. J., P. Werner, and M. Zacharias, 2006, Small **2**, 700.
Farahani, J. N., *et al.*, 2005, Phys. Rev. Lett. **95**, 017402.
Feenstra, R. M., *et al.*, 1987, Phys. Rev. Lett. **58**, 1192.
Feldstein, M. J., *et al.*, 1996, J. Phys. Chem. **100**, 4739.
Fischer, U. Ch., 1998, in *Scanning Probe Microscopy. Analytical Methods*, edited by R. Wiesendanger, Topics in Scanning Near-Field Optical Microscopy (Springer, New York), p. 161.
Foster, A., and W. A. Hofer, 2006, *Scanning Probe Microscopy* (Springer, New York).
Franke, K., J. Besold, W. Haessler, and C. Seegebarth, 1994, Surf. Sci. Lett. **302**, L283.
Freitag, M., A. T. Johnson, S. V. Kalinin, and D. A. Bonnell, 2002, Phys. Rev. Lett. **89**, 216801.
Frenzel, A., M. M. Qazilbash, M. Brehm, Byung-Gyu Chae, Bong-Jun Kim, Hyun-Tak Kim, A. V. Balatsky, F. Keilmann, and D. N. Basov, 2009, Phys. Rev. B **80**, 115115.
Freund, H., and G. Pacchioni, 2008, Chem. Soc. Rev. **37**, 2224.
Fukuma, T., *et al.*, 2010, Phys. Rev. Lett. **104**, 016101.
Fumagalli, L., G. Ferrari, M. Sampietro, and G. Gomila, 2009, Nano Lett. **9**, 1604.
Gannepalli, A., *et al.*, 2011, Nanotechnology **22**, 355705.
Gao, C. L., W. Wulfhekel, and J. Kirschner, 2008, Phys. Rev. Lett. **101**, 267205.
Gao, F., Y. Wang, Y. Cai, and D. W. Goodman, 2009, J. Phys. Chem. C **113**, 174.
Garcia, R., 2010, *Amplitude Modulated Atomic Force Microscopy* (Wiley, New York).
Garcia, V., *et al.*, 2009, Nature (London) **460**, 81.
Garcia-Parajo, M. F., 2008, Nature Photon. **2**, 201.
Gaynutdinov, R. V., *et al.*, 2008, Appl. Phys. Lett. **92**, 172902.
Gekhtman, D., *et al.*, 1999, Phys. Rev. Lett. **82**, 3887.
Gerton, J. M., *et al.*, 2004, Phys. Rev. Lett. **93**, 180801.
Giessibl, F. J., 1995, Science **267**, 68.
Giessibl, F. J., 2003, Rev. Mod. Phys. **75**, 949.
Goodman, D. W., 2003, J. Catal. **216**, 213.
Grafström, S., 2002, J. Appl. Phys. **91**, 1717.
Gross, L., *et al.*, 2009, Science **325**, 1110.
Gruverman, A., O. Auciello, and R. Ramesh, and H. Tokumoto, 1997, Nanotechnology **8**, A38.
Gruverman, A., O. Auciello, and H. Tokumoto, 1996, Appl. Phys. Lett. **69**, 3191.
Gruverman, A., O. Auciello, and H. Tokumoto, 1998, Annu. Rev. Mater. Sci. **28**, 101.
Gruverman, A., J. Hatano, and H. Tokumoto, 1997, Jpn. J. Appl. Phys. **36**, 2207.
Gruverman, A., and A. Kholkin, 2006, Rep. Prog. Phys. **69**, 2443.
Gruverman, A., *et al.*, 1995, J. Vac. Sci. Technol. B **13**, 1095.
Gruverman, A., *et al.*, 2009, Nano Lett. **9**, 3539.
Guo, H. Y., *et al.*, 2002, Appl. Phys. Lett. **81**, 715.
Güthner, P., and K. Dransfeld, 1992, Appl. Phys. Lett. **61**, 1137.
Güthner, P., J. Glatz-Reichenbach, and K. Dransfeld, 1991, J. Appl. Phys. **69**, 7895.
Gysel, R., *et al.*, 2008, J. Appl. Phys. **103**, 084120.
Hagan, M. T., H. B. Demuth, and O. De Jesús, 2002, Int. J. Robust Nonlinear Control 12, 959.
Hahn, J. R., and W. Ho, 2005, J. Chem. Phys. **122**, 244704.
Halperin, C., *et al.*, 2004, Nano Lett. **4**, 1253.
Han, P., and P. S. Weiss, 2012, Surf. Sci. Rep. **67**, 19.
Han, P., *et al.*, 2009, ACS Nano **3**, 3115.
Hänel, K., *et al.*, 2006, Surf. Sci. **600**, 2411.
Hanson, J. N., *et al.*, 2006, Nanotechnology **17**, 4946.
Haykin, S., 1998, *Neural Networks: A Comprehensive Foundation* (Prentice-Hall, Upper Saddle River, NJ), 2nd ed.
Heller, E. J., *et al.*, 1994, Nature (London) **369**, 464.
Hembacher, S., *et al.*, 2005, Phys. Rev. Lett. **94**, 056101.
Hendriksen, B. L. M., and J. W. M. Frenken, 2002, Phys. Rev. Lett. **89**, 046101.
Hendriksen, B. L. M., *et al.*, 1998, Rev. Sci. Instrum. **69**, 3879.
Hidaka, T., *et al.*, 1997, Integr. Ferroelectr. **17**, 319.
Hillenbrand, R., and F. Keilmann, 2000, Phys. Rev. Lett. **85**, 3029.
Hirjibehedin, C. F., C. P. Lutz, and A. J. Heinrich, 2006, Science **312**, 1021.
Hla, S. W., *et al.*, 2000a, Surf. Sci. **454–456**, 1079.
Hla, S.-W., *et al.*, 2000b, Phys. Rev. Lett. **85**, 2777.
Hoeppener, C., and L. Novotny, 2008, Nano Lett. **8**, 642.
Hofer, W. A., *et al.*, 2003, Rev. Mod. Phys. **75**, 1287.
Hoffman, J., *et al.*, 2002, Science **297**, 1148.
Hoffmann, R., *et al.*, 2003, Phys. Rev. B **67**, 085402.
Hoffmann, R., *et al.*, 2004, Phys. Rev. Lett. **92**, 146103.
Hofmann, Ph., *et al.*, 1997, Phys. Rev. Lett. **79**, 265.
Hölscher, H., *et al.*, 1999, Phys. Rev. Lett. **83**, 4780.
Hölscher, H., *et al.*, 2002, Appl. Phys. Lett. **81**, 4428.
Hong, S., 2004, Ed., *Nanoscale Phenomena in Ferroelectric Thin Films* (Kluwer, Dordrecht), http://www.itrs.net/Links/2007ITRS/Home2007.htm.
Hsu, J. W. P., *et al.*, 2003, Appl. Phys. Lett. **83**, 4559.
Huber, A., *et al.*, 2007, Adv. Mater. **19**, 2209.
Huber, A. J., F. Keilmann, J. Wittborn, J. Aizpurua, and R. Hillenbrand, 2008, Nano Lett. **8**, 3766.
Ichimura, T., *et al.*, 2004, Phys. Rev. Lett. **92**, 220801.
Icking-Konert, G. S., M. Giesen, and H. Ibach, 1998, Surf. Sci. **398**, 37.
Jaschinsky, P., *et al.*, 2006, Rev. Sci. Instrum. **77**, 093701.
Jesse, S., A. P. Baddorf, and S. V. Kalinin, 2006, Appl. Phys. Lett. **88**, 062908.
Jesse, S., H. N. Lee, and S. V. Kalinin, 2006, Rev. Sci. Instrum. **77**, 073702.
Jesse, S., P. Maksymovych, and S. V. Kalinin, 2008, Appl. Phys. Lett. **93**, 112903.
Jesse, S., *et al.*, 2007, Nanotechnology **18**, 435503.
Jesse, S., *et al.*, 2008a, Appl. Phys. Lett. **93**, 073104.
Jesse, S., *et al.*, 2008b, Nature Mater. **7**, 209.
Johnson, M., and J. Clarke, 1990, J. Appl. Phys. **67**, 6141.
Jung, S., *et al.*, 2011, Nature Phys. **7**, 245.
Kalinin, S. V., and D. A. Bonnell, 2002, Appl. Phys. Lett. **91**, 3816.
Kalinin, S. V., and A. Gruverman, 2007, Eds., *Scanning Probe Microscopy of Electrical and Electromechanical Phenomena at the Nanoscale* (Springer, Berlin).

Kalinin, S. V., and V. Meunier, 2008, Phys. Rev. B **77**, 033403.
Kalinin, S. V., *et al.*, 2002, Nano Lett. **2**, 589.
Kalinin, S. V., *et al.*, 2005a, J. Appl. Phys. **97**, 074305.
Kalinin, S. V., *et al.*, 2005b, Appl. Phys. Lett. **87**, 053901.
Kalinin, S. V., *et al.*, 2006, Ultramicroscopy **106**, 334.
Kalinin, S. V., *et al.*, 2007a, Proc. Natl. Acad. Sci. U.S.A. **104**, 20204.
Kalinin, S. V., *et al.*, 2007b, Annu. Rev. Mater. Sci. **37**, 189.
Kalinin, S. V., *et al.*, 2007c, Appl. Phys. Lett. **90**, 212905.
Kalinin, S. V., *et al.*, 2008a, Mater. Today **11**, 16.
Kalinin, S. V., *et al.*, 2008b, Phys. Rev. Lett. **100**, 155703.
Kamna, M. M., *et al.*, 1996, Science **274**, 118.
Kathan-Galipeau, K., *et al.*, 2011, ACS Nano **5**, 4835.
Katsiev, K., A. Kolmakov, M. Fang, and U. Diebold, 2008, Surf. Sci. Lett. **602**, L112.
Katsiev, K., *et al.*, 2008, Surf. Sci. Lett. **602**, L112.
Keilmann, F., and R. Hillenbrand, 2004, Phil. Trans. R. Soc. A **362**, 787.
Kholkin, A. L., Ch. Wuthrich, D. V. Taylor, and N. Setter, 1996, Rev. Sci. Instrum. **67**, 1935.
Kholkin, A. L., *et al.*, 1996, Appl. Phys. Lett. **68**, 2577.
Kholkin, A. L., *et al.*, 1997, Appl. Phys. Lett. **71**, 2044.
Kim, M. H., *et al.*, 2011, Science **331**, 1312.
Kim, Y., T. Komeda, and M. Kawai, 2002, Phys. Rev. Lett. **89**, 126104.
Kitamura, S., and M. Iwatsuki, 1995, Jpn. J. Appl. Phys. **34**, L145.
Kolmakov, A., and D. W. Goodman, 2000, Catal. Lett. **70**, 93.
Knorr, N., *et al.*, 2002, Phys. Rev. B **65**, 115420.
Kohsaka, Y., *et al.*, 2008, Nature (London) **454**, 1072.
Kolosov, O., A. Gruverman, J. Hatano, K. Takahashi, and H. Tokumoto, 1995, Phys. Rev. Lett. **74**, 4309.
Krause, S., *et al.*, 2007, Science **317**, 1537.
Kresse, G., M. Schmid, E. Napetschnig, M. Shishkin, L. Köhler, and P. Varga, 2005, Science **308**, 1440.
Kubetzka, A., *et al.*, 2002, Phys. Rev. Lett. **88**, 057201.
Kubetzka, A., *et al.*, 2005, Phys. Rev. Lett. **94**, 087204.
Kühn, S., *et al.*, 2006, Phys. Rev. Lett. **97**, 017402.
Kuipers, L., *et al.*, 1995, Rev. Sci. Instrum. **66**, 4557.
Kuk, Y., *et al.*, 1991, J. Vac. Sci. Technol. B **9**, 545.
Kulawik, M., *et al.*, 2005, Surf. Sci. Lett. **590**, L253.
Laegsgaard, E., *et al.*, 2001, Rev. Sci. Instrum. **72**, 3537.
Lai, K., *et al.*, 2007, Rev. Sci. Instrum. **78**, 063702.
Lantz, M. A., *et al.*, 2001, Science **291**, 2580.
Lauhon, L. J., and W. Ho, 2000, Phys. Rev. Lett. **85**, 4566.
Lee, H. J., and W. Ho, 1999, Science **286**, 1719.
Lee, J., *et al.*, 2006, Nature (London) **442**, 546.
Le Rhun, G., I. Vrejoiu, and M. Alexe, 2007, Appl. Phys. Lett. **90**, 012908.
Lewis, A., M. Isaacson, A. Harootunian, and A. Murray, 1984, Ultramicroscopy **13**, 227.
Lipton-Duffin, J. A., *et al.*, 2009, Small **5**, 592.
Liu, G.-Y., *et al.*, 2000, Acc. Chem. Res. **33**, 457.
Longwitz, S. R., *et al.*, 2004, J. Phys. Chem. B **108**, 14 497.
Loppacher, Ch., *et al.*, 2000, Phys. Rev. B **62**, 16 944.
Loth, S., M. Etzkorn, C. P. Lutz, D. M. Eigler, and A. J. Heinrich, 2010, Science **329**, 1628.
Lundgren, E., *et al.*, 2006, J. Phys. Condens. Matter **18**, R481.
Luthi, R., *et al.*, 1993, Surf. Sci. **285**, L498.
Lyding, J. W., *et al.*, 1994, Appl. Phys. Lett. **64**, 2010.
Ma, H., and J. Levy, 2006, Nano Lett. **6**, 341.
Maeder, T., *et al.*, 1996, Appl. Phys. Lett. **68**, 776.
Maksymovych, P., 2009, Phys. Rev. Lett. **102**, 017601.
Maksymovych, P., *et al.*, 2009, Science **324**, 1421.
Mantooth, B. A., *et al.*, 2007, J. Phys. Chem. C **111**, 6167.
Maranganti, R., N. D. Sharma, and P. Sharma, 2006, Phys. Rev. B **74**, 014110.
Martin, Y., D. Abraham, and H. Wickramasinghe, 1988, Appl. Phys. Lett. **52**, 1103.
Matsushige, K., H. Yamada, H. Tanaka, T. Horiuchi, and X. Q. Chen, 1998, Nanotechnology **9**, 208.
Mayergoyzid, 1986, Phys. Rev. Lett. **56**, 1518.
McCarty, G. S., and P. S. Weiss, 2004, J. Am. Chem. Soc. **126**, 16772.
McEllistrem, *et al.*, 1993, Phys. Rev. Lett. **70**, 2471.
McIntyre, B. J., M. Salmeron, and G. A. Somorjai, 1993, J. Vac. Sci. Technol. A **11**, 1964.
Meier, F., *et al.*, 2008, Science **320**, 82.
Meservey, R., and P. M. Tedrow, 1994, Phys. Rep. **238**, 173.
Meyer, B., D. Marx, O. Dulub, U. Diebold, M. Kunat, D. Langenberg, and C. Woell, 2004, Angew. Chem., Int. Ed. **43**, 6641.
Meyer, E., J. Hug, and R. Bennewitz, 2004, *Scanning Probe Microscopy: The Lab on a Tip* (Springer-Verlag, Berlin).
Minary-Jolandan, M., and M. F. Yu, 2009a, Nanotechnology **20**, 085706.
Minary-Jolandan, M., and M. F. Yu, 2009b, ACS Nano **3**, 1859.
Mitsui, T., *et al.*, 2002, Science **297**, 1850.
Moon, C. R., *et al.*, 2008, Science **319**, 782.
Moon, C. R., *et al.*, 2009, Nature Nanotech. **4**, 167.
Moore, A. M., *et al.*, 2010, ACS Nano **4**, 7630.
S. Morita, 2005, Ed., *Roadmap of Scanning Probe Microscopy* (Springer-Verlag, Berlin).
Morita, S., R. Wiesendanger, E. Meyer, 2002, *Non Contact Atomic Force Microscopy* (Springer, Berlin).
Morozovska, A. N., *et al.*, 2006, Appl. Phys. Lett. **89**, 192901.
Morozovska, A. N., *et al.*, 2009, Phys. Rev. B **80**, 214110.
Muralt, P., *et al.*, 1996, Sens. Actuators A, Phys. **53**, 398.
Nanayakkara, S. U., 2007, Phys. Rev. Lett. **98**, 206108.
Naumov, I., A. M. Bratkovsky, and V. Ranjan, 2009, Phys. Rev. Lett. **102**, 217601.
Nelson, B. A., and W. P. King, 2007, Rev. Sci. Instrum. **78**, 023702.
Newnham, R. E., 2005, *Properties of Materials: Anisotropy, Symmetry, Structure* (Oxford University Press, Oxford, UK).
Niestemski, F. C., *et al.*, 2007, Nature (London) **450**, 1058.
Nikiforov, M., *et al.*, 2009, J. Appl. Phys. **106**, 114307.
Nikiforov, M. P., M. J. Brukman, and D. A. Bonnell, 2008, Appl. Phys. Lett. **93**, 182101.
Nikiforov, M. P., *et al.*, 2008, Nano Lett. **8**, 110.
Nilius, N., *et al.*, 2002, Science **297**, 1853.
Novotny, L., 2007a, Prog. Opt. **50**, 137.
Novotny, L., 2007b, Phys. Rev. Lett. **98**, 266802.
Novotny, L., 2008, Nature (London) **455**, 887.
Novotny, L., and B. Hecht, 2006, *Principles of Nano-Optics* (Cambridge University Press, Cambridge, UK).
Novotny, L., and S. J. Stranick, 2006, Annu. Rev. Phys. Chem. **57**, 303.
O'Hayre, R., M. Lee, and F. Prinz, 2004, J. Appl. Phys. **95**, 8382.
O'Hayre, R., G. Feng, W. D. Nix, and F. Prinz, 2004, J. Appl. Phys. **96**, 3540.
Okada, Y., *et al.*, 2011, Phys. Rev. Lett. **106**, 206805.
Orisaka, S., *et al.*, 1999, Appl. Surf. Sci. **140**, 243.
Otero, R., F. Rosei, and F. Besenbacher, 2006, Annu. Rev. Phys. Chem. **57**, 497.
Pang, C. L., R. Lindsay, and G. Thornton, 2008, Chem. Soc. Rev. **37**, 2328.
Park, S.-E., *et al.*, 2006, J. Vac. Sci. Technol. B **24**, 404.
Parker, C., *et al.*, 2010, Nature (London) **468**, 677.
Pascual, J. I., 2003, Nature (London) **423**, 525.

Pascual, J. I., *et al.*, 2001, Phys. Rev. Lett. **86**, 1050.
Petrov, A. G., and F. Sachs, 2002, Phys. Rev. E **65**, 021905.
Pierce, D. T., 1988, Phys. Scr. **38**, 291.
Pietzsch, O., A. Kubetzka, M. Bode, and R. Wiesendanger, 2000, Phys. Rev. Lett. **84**, 5212.
Pietzsch, O., *et al.*, 2001, Science **292**, 2053.
Piner, R. D., *et al.*, 1999, Science **283**, 661.
Pingree, L., and M. Hersam, 2005, Appl. Phys. Lett. **87**, 233117.
Pingree, L., *et al.*, 2009, Adv. Mater. **21**, 19.
Planken, P., 2008, Nature (London) **456**, 454.
Pohl, D. W., W. Denk, and M. Lanz, 1984, Appl. Phys. Lett. **44**, 651.
Qazilbash, M. M., *et al.*, 2007, Science **318**, 1750.
Rai, R., *et al.*, 2010, Mater. Chem. Phys. **119**, 539.
Rang, M., *et al.*, 2008, Nano Lett. **8**, 3357.
Rankin, C., *et al.*, 2007, ACS Nano **1**, 234.
Raschke, M. B., L. Molina, T. Elsaesser, D. H. Kim, W. Knoll, and K. Hinrichs, 2005, Chem. Phys. Chem. **6**, 2197.
Ravlic, R., *et al.*, 2003, Phys. Rev. B **67**, 174411.
Repp, J., *et al.*, 2000, Phys. Rev. Lett. **85**, 2981.
Reuter, K., and M. Scheffler, 2003, Phys. Rev. B **68**, 045407.
Rider, K. B., K. Hwang, M. Salmeron, and G. Somorjai, 2002, J. Am. Chem. Soc. **124**, 5588.
Rider, K. B., *et al.*, 2001, Phys. Rev. Lett. **86**, 4330.
Rodriguez, B. J., *et al.*, 2002a, Appl. Phys. Lett. **80**, 4166.
Rodriguez, B. J., *et al.*, 2002b, J. Cryst. Growth **246**, 252.
Rodriguez, B. J., *et al.*, 2002c, Appl. Phys. Lett. **80**, 4166.
Rodriguez, B. J., *et al.*, 2007a, Nanotechnology **18**, 475504.
Rodriguez, B. J., *et al.*, 2007b, Appl. Phys. Lett. **90**, 122904.
Rodriguez, B. J., *et al.*, 2008, Adv. Mater. **20**, 109.
Rodriguez, B. J., *et al.*, 2009, Adv. Funct. Mater. **19**, 2053.
Rose, M., *et al.*, 2001, J. Chem. Phys. **115**, 10 927.
Rost, M. J., *et al.*, 2005, Rev. Sci. Instrum. **76**, 053710.
Roushan, P., *et al.*, 2009, Nature (London) **460**, 1106.
Sader, J. E., and S. P. Jarvis, 2004, Appl. Phys. Lett. **84**, 1801.
Sanchez, E. J., L. Novotny, and X. S. Xie, 1999, Phys. Rev. Lett. **82**, 4014.
Sarid, D., 1994, *Scanning Force Microscopy: With Applications to Electric, Magnetic, and Atomic Forces* (Oxford University Press, Oxford, England).
Sautet, P., and C. Joachim, 1988, Phys. Rev. B **38**, 12 238.
Sautet, P., *et al.*, 1993, Surf. Sci. **295**, 347.
Schirmeisen, A., D. Weiner, and H. Fuchs, 2006, Phys. Rev. Lett. **97**, 136101.
Schlickum, U., W. Wulfhekel, and J. Kirschner, 2003, Appl. Phys. Lett. **83**, 2016.
Schmid, A. K., R. Q. Hwang, and N. C. Bartelt, 1998, Phys. Rev. Lett. **80**, 2153.
Schuck, P., *et al.*, 2005, Phys. Rev. Lett. **94**, 017402.
Schuller, J. A., T. Taubner, and M. L. Brongersma, 2009, Nature Photon. **3**, 658.
Schwarz, A., *et al.*, 2000, Phys. Rev. B **61**, 2837.
Scrymgeour, D. A., *et al.*, 2007, J. Appl. Phys. **101**, 014316.
Seidel, J., *et al.*, 2009, Nature Mater. **8**, 229.
Shao, R., *et al.*, 2003, Appl. Phys. Lett. **82**, 1869.
Stipe, B. C., M. A. Rezaei, and W. Ho, 1998a, Science **280**, 1732.
Stipe, B. C., M. A. Rezaei, and W. Ho, 1998b, Phys. Rev. Lett. **81**, 1263.
Stoica, T., *et al.*, 2007, Appl. Surf. Sci. **253**, 4300.
Stranick, S. J., and P. S. Weiss, 1994, J. Phys. Chem. **98**, 1762.
Stranick, S. J., *et al.*, 1994, J. Phys. Chem. **98**, 7636.
Street, S. C., C. Xu, and D. W. Goodman, 1997, Annu. Rev. Phys. Chem. **48**, 43.
Stroscio, J. A., and D. M. Eigler, 1991, Science **254**, 1319.
Sugawara, Y., *et al.*, 1995, Science **270**, 1646.
Sugimoto, Y., *et al.*, 2007a, Appl. Phys. Lett. **91**, 093120.
Sugimoto, Y., *et al.*, 2007b, Nature (London) **446**, 64.
Sun, J., J. Schotland, and P. S. Carney, 2007, J. Appl. Phys. **102**, 103103.
Sun, J., J. Schotland, R. Hillenbrand, and P. S. Carney, 2009, Appl. Phys. Lett. **95**, 121108.
Sykes, E. C. H., *et al.*, 2003, Acc. Chem. Res. **36**, 945.
Sykes, E. C. H., *et al.*, 2005, J. Am. Chem. Soc. **127**, 7255.
Sykes, E. C. H., *et al.*, 2006, J. Phys. Chem. B **110**, 7380.
Synge, E. H., 1928, Philos. Mag. **6**, 356.
Takami, T., *et al.*, 2010, J. Am. Chem. Soc. **132**, 16460.
Takata, K., 1996, J. Vac. Sci. Technol. B **14**, 882.
Takata, K., K. Kushida, K. Torii, and H. Miki, 1994, Jpn. J. Appl. Phys. **33**, 3193.
Taminiau, T. H., *et al.*, 2007, Nano Lett. **7**, 28.
Taminiau, T. H., *et al.*, 2008, Nature Photon. **2**, 234.
Tanaka, K., Y. Kurihashi, T. Uda, Y. Daimon, N. Odagawa, Hirose, Y. Hiranaga, and Y. Cho, 2008, Jpn. J. Appl. Phys. **47**, 3311.
Tao, F., *et al.*, 2010, Science **327**, 850.
Taubner, T., R. Hillenbrand, and F. Keilmann, 2003, J. Microsc. **210**, 311.
Ternes, M., *et al.*, 2008, Science **319**, 1066.
Tersoff, J., and D. R. Hamann, 1983, Phys. Rev. Lett. **50**, 1998.
The October 2007 issue of Materials Today, Vol. 10, Issue 10, pp. 1–56 dedicated to ''Complexity and Diversity.''
Tian, L., A. Vasudevarao, A. N. Morozovska, E. A. Eliseev, S. V. Kalinin, and V. Gopalan, 2008, J. Appl. Phys. **104**, 074110.
Tseleva, A., *et al.*, 2007, Rev. Sci. Instrum. **78**, 044701.
Ueyama, H., *et al.*, 1995, Jpn. J. Appl. Phys. **34**, L1086.
van de Walle, *et al.*, 1987, Appl. Phys. Lett. **50**, 22.
Vang, R. T., *et al.*, 2008 Chem. Soc. Rev. **37**, 2191.
Wachowiak, A., *et al.*, 2002, Science **298**, 577.
Weisendanger, R., 1994, *Scanning Probe Microscopy and Spectroscopy*, Cambridge University Press, Cambridge, England.
Weiss, P. S., 2008, Acc. Chem. Res. **41**, 1772.
Weiss, P. S., and D. M. Eigler, 1992, Phys. Rev. Lett. **69**, 2240.
Weiss, P. S., and D. M. Eigler, 1993, Phys. Rev. Lett. **71**, 3139.
Weiss, P. S., and G. S. McCarty, 2003, U.S. Patent No. 6,597,194.
Weiss, S., *et al.*, 1993, Appl. Phys. Lett. **63**, 2567.
Wiesendanger, R., 1998, Ed., in *Scanning Probe Microscopy. Analytical Methods, Topics in Scanning Near-Field Optical Microscopy* (Springer, New York).
Wiesendanger, R., 2009, Rev. Mod. Phys. **81**, 1495.
Wiesendanger, R., 2011, Curr. Opin. Solid State Mater. Sci. **15**, 1.
Wiesendanger, R., *et al.*, 1990, Phys. Rev. Lett. **65**, 247.
Williams, C. C., W. P. Hough, and S. A. Rishton, 1989, Appl. Phys. Lett. **55**, 203.
Wöll, C., 2007, Prog. Surf. Sci. **82**, 55.
Woodside, M. T., and P. L. McEuen, 2002, Science **296**, 1098.
Wulfhekel, W., and J. Kirschner, 1999, Appl. Phys. Lett. **75**, 1944.
Xu, S., and G.-Y. Liu, 1997, Langmuir **13**, 127.
Yang, C., Z. H. Zhong, and C. M. Lieber, 2005, Science **310**, 1304.
Yang, C. H., *et al.*, 2009, Nature Mater. **8**, 485.
Yang, H., *et al.*, 2002, Phys. Rev. Lett. **89**, 226101.
Yayon, Y., *et al.*, 2007, Phys. Rev. Lett. **99**, 067202.
Yunseok, K., A. Marin, and S. Ekhard, 2010, Appl. Phys. Lett. **96**, 032904.
Zhang, T., *et al.*, 2009, Phys. Rev. Lett. **103**, 266803.
Zhang, X., *et al.*, 2007, Physica (Amsterdam) **387B**, 147.
Zhang, Y., *et al.*, 2008, Nature Phys. **4**, 627.
Zhao, M. H., Z. L. Wang, and S. X. Mao, 2004, Nano Lett. **4**, 587.
Zuloaga, J., E. Prodan, and P. Nordlander, 2009, Nano Lett. **9**, 887.
Zurita-Sanchez, J. R., and L. Novotny, 2002, J. Opt. Soc. Am. B **19**, 1355.